THE UNIVERSITY OF CHICAGO

SEARCHING FOR DARK MATTER WITH SUPERCONDUCTING QUBITS

A DISSERTATION SUBMITTED TO
THE FACULTY OF THE DIVISION OF THE PHYSICAL SCIENCES
IN CANDIDACY FOR THE DEGREE OF
DOCTOR OF PHILOSOPHY

DEPARTMENT OF PHYSICS

BY
AKASH V. DIXIT

CHICAGO, ILLINOIS
JUNE 2021

Table of Contents

List of Figures

xv

List of Tables

Acknowledgments

I have been privileged to have undertaken this journey through grad school with so many people alongside me. I have been able to share the joys with so many people and been lucky enough to have their support when things were difficult. I'd like to thank my labmates, Nate, Vatsan, Ravi, Ankur, and everyone else in the Schuster lab who made it so fun to learn and create together. I've been fortunate to have not one, but two advisors: Aaron and Dave. From the first day we met, Aaron's way of thinking has been infectious and I hope I have been able to absorb his ability to systematically work through any challenge at hand. It was Dave's openness to collaboration that made undertaking this thesis work even possible. His innovative approach to the problems we encountered meant that I was never stuck and I left each conversation with new ideas. Most importantly, my advisors gave me the freedom to explore and create, which has made grad school a rewarding and fulfilling experience. I have to thank my friends, Zo, Ryan, Jon, Sam, Aziza, Andrew, who made grad school fun even when we had insurmountable piles of homework and tons of research to work on. Thank you to everyone I played music with, went on a bike ride with, played basketball with. I'm lucky to have the support of my family who always reminded me of what's important in life from music to hiking to good food, Amma, Appa, Chirag, Anshu Mami, Uday Mama. Finally, I want to thank my partner Meeka who is the best friend anyone can ask for. She has encouraged me, supported me, and believed in me during the hardest and best times. She has made my life richer in every way imaginable. My research and work have been fulfilling and exciting, but my proudest achievement has been building a life together with Meeka.

Abstract

Dark matter is an enduring mystery in our quest to understand the fundamental constituents of our universe. Low mass bosons, such the axion or hidden photon, are compelling dark matter candidates. We leverage their potential interactions with electromagnetic fields, whereby the dark matter (of unknown mass) on rare occasion converts into a single photon, to devise a method of detecting these candidates. Current dark matter searches operating at microwave frequencies use a resonant cavity to coherently accumulate the field sourced by the dark matter and a near standard quantum limited (SQL) linear amplifier to read out the cavity signal. To further increase sensitivity to the dark matter signal and enable future searches, sub-SQL detection techniques are required.

In this thesis, I report the development of a novel microwave photon counting technique and a new exclusion limit on hidden photon dark matter. We operate a superconducting qubit to make repeated quantum non-demolition measurements of cavity photons and apply a hidden Markov model analysis to reduce the noise to $15.7\,\mathrm{dB}$ below the quantum limit, with overall detector performance limited by a residual background of real photons. With the present device, we perform a hidden photon search and constrain the kinetic mixing angle to $\epsilon \leq 1.68 \times 10^{-15}$ in a band around $6.011\,\mathrm{GHz}$ ($24.86\,\mathrm{\mu eV}$) with an integration time of $8.33\,\mathrm{s}$. This demonstrated noise reduction technique enables future dark matter searches to be sped up by a factor of 1,300. By coupling a qubit to an arbitrary quantum sensor, more general sub-SQL metrology is possible with the techniques presented in this work.

Chapter 1

Introduction

The beauty of scientific inquiry is that you don't know what you will discover when you set out. Along my path to explore cosmological questions and uncover the nature of dark matter, I have taken as many detours as possible. These experiences have made my work richer and allowed me to be part of an endeavour worthy of the expansive questions we are attempting to answer. The defining detour has been the opportunity to learn from and be part of the burgeoning field of quantum information. The techniques and technologies from this field are the backbone of the work I present here. Although a full scale quantum computer may still be in the distant future, the advances are already yielding results in unexpected places. The gains made in the effort to construct a quantum computer directly lead to the novel dark matter detection method we develop in this work. This type of cross cutting research is the hallmark of scientific progress.

Working on an experiment involving two seemingly disparate fields has presented many challenges and opportunities. Each day can be as different as fabricating superconducting quantum bits to machining high purity aluminum cavities or operating sensors in near absolute zero temperatures to calculating dark matter constraints. I am in the middle of two worlds: the dark matter on a galactic scale and quantum sensors on the nano scale.

1.1 Dark matter

A large part of why I have been drawn to studying physics is the unsolved mysteries and collective effort to unravel them. There are a lot of things we understand about the universe, but the fun is in all the things we do not. Dark matter one of these mysteries; it is a significant component (27%) of the matter-energy content of the universe[10] and yet, we do not know its intrinsic nature.

The process of understanding dark matter is as large scale as the mystery itself. The first hints of the existence of dark matter have come from astronomy. Astrophysics and cosmology provides compelling hypothesis for what the nature of dark matter could be. Experiments in numerous laboratories across the world are trying to generate or detect the dark matter. This work is another in the long line of experiments drawing on the expertise of an emerging field to devise novel methods to sense the dark matter with terrestrial experiments.

1.1.1 How do we know dark matter exists

The evidence of the existence of dark matter is predicated on astronomical observations of its gravitational interactions. Anomalies observed in various different experiments can be explained by a dark matter hypothesis, making it quite compelling.

Galactic rotation curve

One stark example of dark matter's gravitational influence is in the velocity of stars in the periphery of spiral galaxies. From Newtonian mechanics, based on the observed distribution of stars, we expect the velocity of stars further out from the center to decrease. This can be calculated by determining the kinetic energy of a star (mass m, velocity v) required to sustain a circular orbit (at a distance R) in the gravitational potential of the massive central portion of the galaxy (M), $K = -\frac{1}{2}U$.

$$\frac{1}{2}mv^2 = \frac{1}{2}G\frac{Mm}{R} \tag{1.1}$$

As the stars get further out, we expect the velocity to fall off as $v \sim \frac{1}{\sqrt{R}}$. However, observations of the velocity of stars in spiral galaxies indicate that the velocity remains constant[11]. This contradicts the premise that the bulk of a galaxy's mass is in the central bulge of visible stars, but instead indicates that there may be a halo of dark matter that extends beyond the visible components of the galaxy[12,13].
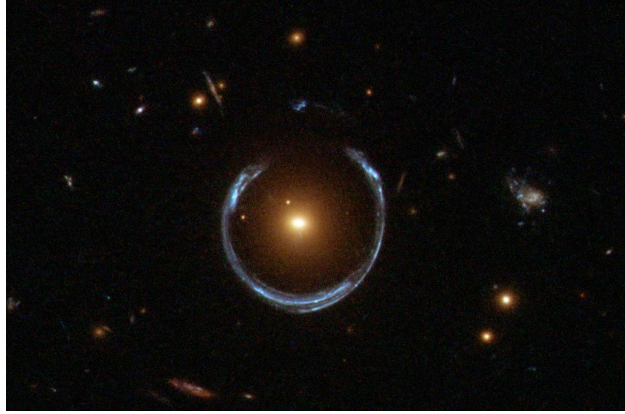
Figure 1.1: **Lensing of light**. Light from a galaxy in the background is warped and distorted as it passes by a massive dark object in the foreground.

The velocity curves also provide insight into the distribution of the dark matter in the halo. The equation describing the balance of kinetic and gravitational potential energy in the presence of a halo of dark matter with density ρ is shown in Equation 1.2.

$$\frac{1}{2}mv^2 = \frac{1}{2}G\frac{4}{3}\frac{\pi R^3 \rho}{R} \tag{1.2}$$

The observation indicate that the velocities are constant with increasing distance. This implies that the right hand side of Equation 1.2 must be independent of R. This gives an estimate of the distribution of the dark matter; the density must scale as $\rho \sim \frac{1}{R^2}$.

Gravitational lensing

The massive scale of the dark matter in galaxies and collections of galaxies can lead to mind bending gravitational effects. Such massive objects have an immense effect on the curvature of the space-time around them, warping it significantly[14]. As light from distant galaxies passes by this warped space-time on its journey towards our eyes, the galaxy appears distorted (see Figure 1.1).

The specific details of the image produced by the light bending around the dark matter give us insight into the mass and distribution of the foreground object. Observations of this
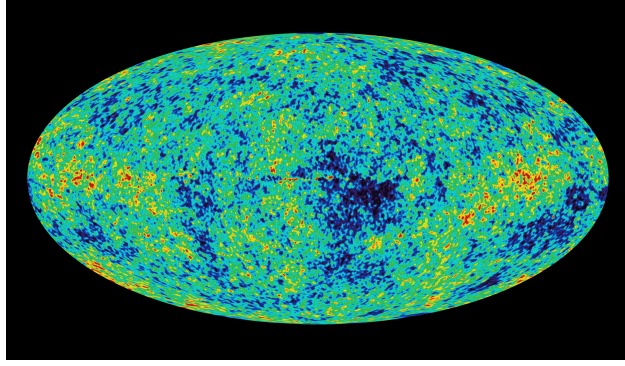
Figure 1.2: **Anisotropy of cosmic microwave background**. Angular power spectrum of anisotropy in the radiation reveals that a significant component of the universe's matter-energy content is comprised of dark matter.

effect are ubiquitous, and are a clear indication that the universe is filled with unseen mass exerting its gravitational influence on everything.

Cosmic microwave background

The remnant radiation from the early part of the universe's evolution can now be observed as a cosmic microwave background[15] and corresponds to a temperature of $2.73\,\mathrm{K}$. Small deviations from the average temperature reveal important features of our universe (see Figure 1.2). A multipole expansion of the anisotropies shows a series of peaks[16,17] corresponding to harmonics of the sound waves induced by the perturbations of the gravitational potential in the early universe. The first reveals that the curvature of the universe is flat and the relative amplitudes of the second and third are consistent with a universe filled with dark matter.

Structure formation

On the largest scales the universe is organized into a cosmic web. These structures house the galaxies, stars, black holes, and much of the 'normal' matter in our universe. The existence of large scales structures and the variety of interesting objects that fill them, including oceans, flowers, whales, rocks, and octopuses, is all due to dark matter. Small fluctuations in the density of the dark matter in the early universe are magnified by the universe's ex-

pansion. Though the radiation in the early universe counteracts the gravitational attraction of 'normal' matter, the dark matter is unaffected and begins to collapse. This seeds a gravitational potential that the rest of the matter can fall into when the universe expands and cools. These seeds produce the vibrant, intricate patterns that we see when we look up at the universe, 13.8 billion years later .

1.2 Circuit quantum electrodynamics

In the endeavour to detect and understand the dark matter, we must continuously adapt and develop new technologies. In this work, we use innovations originating in the field of circuit quantum electrodynamics[18,8,19] as a basis for the detector we construct and the techniques we use.

1.2.1 Artificial atom coupled to a microwave cavity

Superconducting circuitry can be used to build systems analogous to an atom in a cavity. The advantages of building our own artificial atom in a cavity are controllable, enhanced coupling, arbitrary choice of atomic transition frequency, and customizable device geometry.

The key enabling component that makes this all work is a Josephson junction[20–22], which is effectively an nonlinear inductor. Along with a capacitive element that functions as a dipole antenna, the Josephson junction forms a nonlinear oscillator with a periodic potential. This nearly harmonic circuit no longer contains evenly spaced levels and the manifold of the the first two levels can be addressed to form a qubit. The qubit transition frequency is in the microwave region and the qubit can be controlled using conventional GHz electronics (as used for cell phones).

The artificial atom is embedded into a 3D resonating structure and couples to the modes with the dipole antenna. This interaction provides a platform for growing collection of experiments including many body simulations, quantum information processing, and metrology of

quantum systems. In this work we harness the metrological capabilities of superconducting qubits to develop a novel dark matter detection technique.

1.3 Thesis overview

The work presented in this dissertation is an attempt to shed light onto the deep mystery of dark matter. I detail the development of a quantum sensor and its application in dark matter detection. In Chapter 2, I describe how to harness the potential interactions between dark matter and electromagnetism to produce a detectable signal and why it is necessary to rethink the way we perform the detection. Next, I explain how to utilize superconducting qubit technology to construct a photon counting device in Chapter 3. This includes the full process of design, simulation, and fabrication required to construct and operate superconducting quantum circuits. I harness the non-demolition nature of the interaction between superconducting qubits and photons, in Chapter 4, to suppress sensitivity to detector based false positives. The analysis of the resulting signal is shown in Chapter 5. This section focuses on incorporating all possible error channels into the analysis to make an informed decision about the source of a signal. In Chapter 6, I demonstrate the operation of the photon counting device and characterize its properties. I show successful suppression of detector errors and describe the limiting backgrounds. In Chapter 7, I use the detector to conduct a dark matter search for hidden photons and exclude candidates with unprecedented sensitivity. I conclude by describing how photon counting with a superconducting qubit can be employed in future dark matter searches for axions and hidden photons.

Chapter 2

Photon counting for dark matter detection

In this chapter, I outline the detection principles for two low mass dark matter candidates. I describe the operating principle of a haloscope, which looks for dark matter converting to light. Current detection techniques are fundamentally limited by the standard quantum limit (SQL), a manifestation of the uncertainty principle. I show that employing photon counting methods is imperative to subvert the SQL that currently limits dark matter detectors.

2.1 Dark matter candidates

In this work I focus on two low mass candidates: the axion and hidden photons.

Axion physics originates from the mystery of why charge-parity symmetry (CP) is conserved in quantum chromodynamics (QCD). If CP symmetry were broken in the strong force, this would manifest itself as a measurable electric dipole moment (EDM) of the neutron. The angle θ, which characterizes the predicted CP violating term in QCD and sets the scale of the neutron EDM, is expected to be $\mathcal{O}(1)$. However, current experimental constraints of the neutron EDM indicate that $\theta \leq 10^{-10}$. To explain why θ is so small, Peccei and Quinn[23,24] postulated that rather than being a number, θ could be described as a dynamical field. A tilting of the potential that θ lives in would result in the value of the field to tend to zero, consistent with measurements. As a consequence of the global symmetry breaking and a tilting of the potential, a pseudo Nambu-Golstone boson is generated. This particle is dubbed the QCD axion[24,23,25,26]. If produced with the right initial conditions in the early history of the universe, the axion would account for the dark matter abundance observed today[27–29]. There are also compelling models that show how the axion could be involved in the observed asymmetry between matter and anti-matter in the universe[30].

The origin story of hidden photons is slightly different[4,6]. They could be produced during

the inflationary period of the early universe. This is an interesting idea since these particles could account for the dark matter and would also be consistent with other measures of inflation such as the power spectrum of the cosmic microwave background.

Both candidates could have interactions with electromagnetism that we can harness to detect their presence. This interaction is enabled by a magnetic field, in the case of axions, or occurs spontaneously, in the case of hidden photons. In either situation, the result is a current density that can be used to source a detectable electric field.

2.1.1 Axion electrodynamics
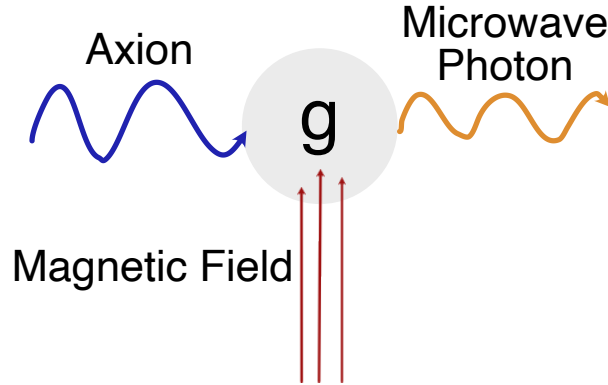
Figure 2.1: **Axion conversion to photon**. In the presence of an externally supplied magnetic field, the axion can convert to a photon.

The interaction between the axion and electromagnetism is described in Equation 2.1. $g_{a\gamma\gamma}$ is the coupling strength, a represents the axion field, F ($\tilde{F}$) is the field strength tensor (and its dual).

$$\mathcal{L} \supset -\frac{1}{4} g_{a\gamma\gamma} a F_{\mu\nu} \tilde{F}^{\mu\nu} \tag{2.1}$$

To understand how this interaction can produce a measurable signal we recast it in terms of electric and magnetic fields in Equation 2.2.

$$\mathcal{L}_{\text{axion}} = g_{a\gamma\gamma} a \mathbf{E} \cdot \mathbf{B} \tag{2.2}$$

To probe this interaction, we can supply an external magnetic field ($\mathbf{B}_0$) to reduce the interaction to a two-body exchange between the axion and a quanta of the electric field (a photon) as shown in Figure 2.1. In the presence of a magnetic field, the axion produces an effective current that couples to electromagnetism. Using the fact that $\mathbf{E} = -\frac{\partial \mathbf{A}}{\partial t}$ and integrating by parts we obtain Equation 2.3 to describe the axion induced current density.

$$\mathcal{L}_{\text{axion}} = \mathbf{J}_{\text{axion}} \cdot \mathbf{E} = \frac{\partial}{\partial t} \left(g_{a\gamma\gamma} a \mathbf{B}_0 \right) \cdot \mathbf{A} \tag{2.3}$$

The velocity dispersion of dark matter, gravitationally bound in our galaxy, is $10^{-3}c$ and the kinetic energy effectively broadens of the dark matter line such that it has a linewidth $10^{-6} m_{\text{DM}}$. The generated AC current will be oscillating with frequency approximately equal to the mass of the axion. Assuming the dark matter is composed solely of axions, we relate the energy contained in the axion field to the density of dark matter in Equation 2.4.

$$\rho_{\text{DM}} = \frac{1}{2} m_a^2 a^2 \tag{2.4}$$

Substituting Equation 2.4 into Equation 2.3 and evaluating the time derivative on the oscillating axion field, yields the generated current density in terms of the dark matter abundance (Equation 2.5). The spatial dependence of the magnetic field is imprinted onto the generated current density.

$$\mathbf{J}_{\text{axion}}(t) = g_{a\gamma\gamma} \sqrt{2\rho_{\text{DM}}} \mathbf{B}_0 e^{i m_a t} \tag{2.5}$$

2.1.2 Hidden photon electrodynamics

The Lagrangian of electromagnetism is modified to include a hidden sector kinetically mixed with the standard model electromagnetism as shown in Equation 2.6

$$\mathcal{L} \supset -\frac{1}{4} \left(F_{\mu\nu} F^{\mu\nu} + F'_{\mu\nu} F'^{\mu\nu} \right) - J_\mu A^\mu + \frac{1}{2} m_{\gamma'}^2 A'_\mu A'^\mu + \epsilon m_{\gamma'}^2 A'_\mu A^\mu \tag{2.6}$$
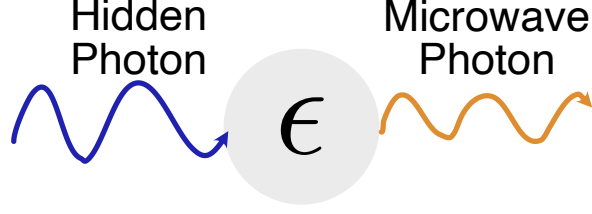
Figure 2.2: **Hidden photon conversion to photon**. The hidden photon can mix with the standard electromagnetism and convert to a photon.

The hidden photon gauge potential and field strength are represented by A'_μ and $F'_{\mu\nu}$. The mass of the hidden photon is given by $m_{\gamma'}$. The last term in this Lagrangian describes the mixing between hidden and standard electromagnetism as shown in Figure 2.2. A background of hidden photons forms an effective current density of the form shown in Equation 2.7

$$\mathbf{J}_{\mathrm{HP}} = \epsilon m_{\gamma'}^2 \mathbf{A}' \tag{2.7}$$

This AC current will be oscillating with frequency equal to the mass of the hidden photon. Assuming the dark matter is composed solely of hidden photons, we relate the magnitude of the hidden photon gauge potential to the density of dark matter in Equation 2.8.

$$\rho_{\mathrm{DM}} = \frac{1}{2} m_{\gamma'}^2 A'^2 \tag{2.8}$$

Substituting Equation 2.8 into Equation 2.7 and accounting for the oscillatory behavior yields the generated current density in terms of the dark matter abundance (Equation 2.9). $\hat{\mathbf{u}}$ represents the spatial dependence of the hidden photon polarization which is imprinted onto the generated current density.

$$\mathbf{J}_{\mathrm{HP}}(t) = \epsilon m_{\gamma'}^2 \mathbf{A}' = \epsilon m_{\gamma'} \sqrt{2\rho_{\mathrm{DM}}} e^{im_{\gamma'}t} \hat{\mathbf{u}} \tag{2.9}$$

2.2 Dark matter detection with a haloscope

There are various techniques to try and detect low mass particles such as the axion or hidden photon, including astrophysical searches for photon absorption near regions of high magnetic fields[31], recoil measurements from detectors such as CDMS and XENON100[32,33], and light shining through walls experiments[34,35].

In order to detect these candidates, we harness their potential interaction with electromagnetism. Both axions and hidden photons potentially source an effective oscillating current density $\mathbf{J}_{DM}$. A microwave cavity can be used to capture the effect of this current source. Via Faraday's law, the dark matter sources the electric field of a microwave cavity: $\nabla \times \mathbf{B} - \frac{\partial \mathbf{E}}{\partial t} = \mathbf{J}_{DM}$. For axions, the effective current density is $\mathbf{J}_{axion} = g_{a\gamma\gamma}\sqrt{2\rho}\mathbf{B}_0 e^{im_a t}$, where $g_{a\gamma\gamma}$ is the predicted coupling of the axion field to electromagnetism, ρ is the local dark matter density, $\mathbf{B}_0$ is a DC magnetic field applied in the laboratory, and m_a is the mass of the axion. For hidden photons, the effective current is $\mathbf{J}_{HP} = \epsilon m_{\gamma'}\sqrt{2\rho}e^{im_{\gamma'}t}\hat{\mathbf{u}}$, where ϵ is a postulated kinetic angle of mixing between standard electromagnetism and hidden sector electromagnetism, $\hat{\mathbf{u}}$ is the polarization of the hidden photon field, and $m_{\gamma'}$ is the hidden photon mass.

2.2.1 Signal accumulation with a microwave cavity

To coherently accumulate the signal, the microwave cavity must be on resonance with the dark matter $m_{DM}c^2 = \hbar\omega$. For an axion search this cavity must be immersed in a high magnetic field. This precludes the use of superconducting materials to minimize losses, and the cavity is typically made from high purity copper. Novel techniques are currently being developed to implement high quality factor cavities in a magnetic field. This includes using thin coatings of superconducting material and dielectric materials to create photonic bandgap crystals. Hidden photon searches do not require a magnetic field, so superconducting materials can be used to construct low loss cavities. We can take advantage of the advances made

in accelerator physics fabrication techniques to build high quality factor microwave cavities.

2.2.2 Probability of dark matter depositing a photon

In order to optimally extract power from the dark matter field, the dark matter mass has to equal the resonant frequency of the cavity. As the search for dark matter extends to higher masses (higher frequencies), the cavity volume must shrink to maintain the resonance condition. The signal power and therefore, expected induced photon population scales poorly at higher frequencies $\bar{n}_{\mathrm{DM}} \sim V \sim \lambda^3 = f^{-3}$.

For Axion Dark Matter eXperiment[36] operating at 650 MHz, the expected signal photon occupation number is $\sim 10^{-2}$. For an axion search with the microwave cavity (6.011 GHz) used in this work and given the experimental parameters in typical axion search experiments[37–40], QCD axion models[41–44] predict a signal with mean photon number of $\bar{n}_{\mathrm{axion}} \sim 10^{-8} - 10^{-5}$ per measurement. For hidden photons, the parameter space is less constrained,[4,45] and the mean photon number per measurement could be $\bar{n}_{\mathrm{HP}} \leq 10^{-1}$.

2.2.3 Measuring the state of the cavity

In order to discern the minute signals expected from the dark matter, it is necessary to employ low noise readout techniques. There has been a concerted effort over the last few decades to use amplifiers with ultra low noise temperatures. Recent axion searches have started using superconducting amplifiers that operate near the standard quantum limit (SQL). One device currently used in axion experiments is a Josephson parametric amplifier (JPA), whose operation requires a flux bias to bring the amplifier nearly on resonance with the cavity and a charge or flux pump to enable the amplification. The nonlinearity of the JPA can result in $> 20\,\mathrm{dB}$ signal gain. Most importantly, the input referred noise can be as one photon equivalent, also known as the standard quantum limit (SQL). Appendix A describes the added noise in the process of linear amplification at the quantum limit.

Even with quantum limited amplification, the dark matter induced signals are over-

whelmed by noise. The probability of a signal photon can be orders of magnitude below the SQL noise $(\bar{n}_{\mathrm{SQL}} \gg \bar{n}_{\mathrm{axion}}, \bar{n}_{\mathrm{HP}})$.

2.3 Subverting the quantum limit
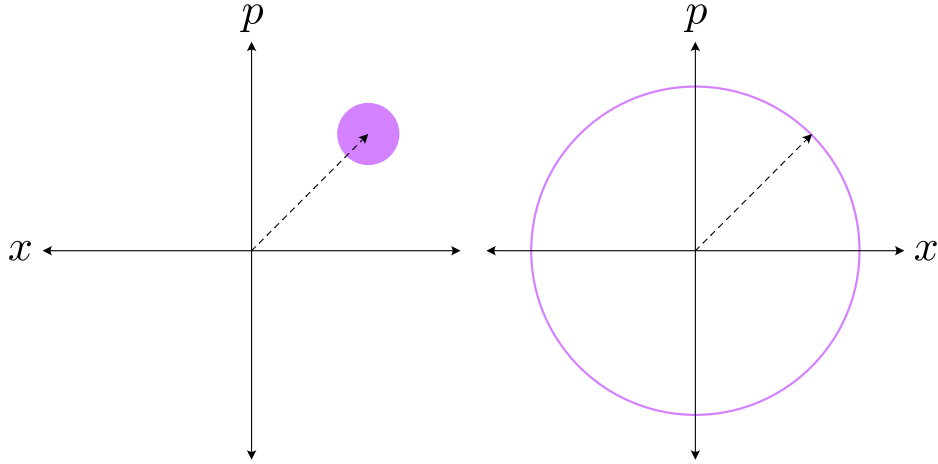
Figure 2.3: **Linear amplification vs photon counting**. (Left) Linear amplification introduces backaction noise equally along both quadratures, represented by the purple circle. This amounts to one photons worth of noise. (Right) Counting photons imparts all the backaction onto the phase information, represented by the purple ring. In principle, this allows for a noiseless measurement of the field amplitude.

The devices currently used for readout in axion searches amplify both the quadratures of the cavity field. This mode of operation is known as phase preserving amplification as shown in Figure 2.3. The two quadratures correspond to the real and imaginary components of the field in the cavity as shown in Equations 2.10 and 2.11.

$$I = \frac{a + a^\dagger}{2} \tag{2.10}$$

$$Q = \frac{a - a^\dagger}{2i} \tag{2.11}$$

For example, to measure a coherent state of the cavity $|\alpha\rangle$ with $\alpha = |\alpha|e^{i\theta}$, we apply the

quadrature operators to the state to obtain the real and imaginary components.

$$I \left| \alpha \right\rangle = \frac{\alpha e^{i\theta} + \alpha^* e^{-i\theta}}{2} \left| \alpha \right\rangle = \left| \alpha \right| \cos \theta \left| \alpha \right\rangle \tag{2.12}$$

$$Q \left| \alpha \right\rangle = \frac{\alpha e^{i\theta} - \alpha^* e^{-i\theta}}{2i} \left| \alpha \right\rangle = \left| \alpha \right| \sin \theta \left| \alpha \right\rangle \tag{2.13}$$

Since the quadrature measurements are composed of the non commuting ladder operators of the harmonic oscillator, $[a, a^\dagger] = 1$, they inherit commutation relations (Equation 2.14) and associated uncertainty relation (Equation 2.15).

$$
\begin{aligned}
[I, Q] &= \frac{1}{4i}[a + a^\dagger, a - a^\dagger] \\
&= \frac{1}{4i} \left([a, a - a^\dagger] + [a^\dagger, a - a^\dagger] \right) \\
&= \frac{1}{4i} \left(-[a, a^\dagger] + [a^\dagger, a] \right) \\
&= \frac{1}{4i} \left(-1 + (-1) \right) \\
&= \frac{1}{2i}
\end{aligned} \tag{2.14}
$$

The non zero commutator of the two measured quantities results in an uncertainty relation between them.

$$
\begin{aligned}
\Delta I \Delta Q &\geq \frac{1}{2} |[I, Q]| \\
&\geq \frac{1}{4}
\end{aligned} \tag{2.15}
$$

This uncertainty manifests as the quantum limit when trying to measure both relevant quadratures of the field inside of the cavity. Alternatively, we could use a device that selectively measures one quadrature resulting in a distortion of the phase space density of the measured state[2].

For the purposes of a dark matter search, information about both quadratures of the signal field is unnecessary. We only need to determine if the dark matter has successfully deposited a photon in the cavity. Therefore, it is sufficient to count the photons in the cavity rather than extract information about both quadratures[46].

This amounts to measuring the quantity $a^\dagger a$ rather than I and Q. The backaction of such a number measurement is a complete randomization of the phase of the field. This is evident by recasting the Heisenberg uncertainty principle in terms of number (n) and phase (ϕ).

$$\Delta n \Delta \phi \geq \frac{1}{2} \tag{2.16}$$

By counting the number of photons in the cavity it is possible to achieve an arbitrarily accurate measurement of the field amplitude while giving up all information about the phase of the field. This is a trade-off worth making since the primary focus of current dark matter searches is to efficiently search vast regions of the mass and coupling parameter space. If and once the dark matter is detected, the phase information becomes useful in understanding the structure of the dark matter distribution in our galaxy. Until then, photon counting is the optimal strategy for low mass dark matter searches.

Chapter 3

Device design, fabrication, and operation

To build a photon counting device, we employ the techniques devised in atomic physics[47,48].
Coupling an artificial atom (superconducting qubit) to the field of a microwave cavity allows
us to count photons. In this chapter I will describe the design and fabrication process
required to construct a useful photon counting device.

3.1 Constructing a qubit with a Josephson junction

A key component of the device used in this work is a Josephson junction. This element
provides the nonlinearity that is needed to transform linear oscillators into quantum bits.
The junction is composed of two superconducting islands separated by a insulating barrier.

3.1.1 Non linear inductance

The relations describing the Josephson junction[20,22] are given in Equations 3.1 and 3.2.

$$V(t) = \frac{\Phi_0}{2\pi} \frac{\partial \varphi(t)}{\partial t} \tag{3.1}$$

$$I(t) = I_c \sin\left(\varphi(t)\right) \tag{3.2}$$

V is the voltage across the junction, Φ_0 is the magnetic flux quanta $h/(2e)$, ϕ is the phase
difference across the junction, I is the current across the junction, I_c is critical current above
which the junction becomes normal and resistive.

Differentiating Equation 3.2 and substituting into Equation 3.1 yields a relation that is
identified as Faraday's Law of induction as shown in Equation 3.3.

$$V(t) = \frac{\Phi_0}{2\pi I_c \cos\left(\varphi(t)\right)} \frac{\partial I(t)}{\partial t} \tag{3.3}$$

The junction behaves a nonlinear inductance shown in Equation 3.4.

$$L = \frac{\Phi_0}{2\pi I_c \cos \varphi(t)} \tag{3.4}$$

3.1.2 Josephson energy

The energy stored in the Josephson junction can be computed using Equations 3.1 and 3.2 shown in Equation 3.5.

$$U = \int IV = E_J(1 - \cos(\varphi)) \tag{3.5}$$

The coefficient is defined as the Josephson energy $E_J = \frac{\Phi_0 I_c}{2\pi}$.

3.1.3 Non linear oscillator

We couple the Josephson junction to a capacitor to enable a dipole coupling to a microwave environment. This contribution a charging energy related to the capacitance $E_C = e^2/(2C)$. The Hamiltonian for the system is shown in Equation 3.6.

$$\mathcal{H} = 4E_C n^2 + E_J(1 - \cos(\varphi)) \tag{3.6}$$

n is the number of Cooper pairs on the capacitor. The number of Cooper pairs and phase fluctuations are conjugate variables. For small phase fluctuations $\varphi \ll pi$, the Josephson energy component can be approximated by expanding the sinusoidal potential fourth order (Equation 3.7).

$$\mathcal{H} = 4E_C n^2 + E_J \left(\frac{\varphi^2}{2!} - \frac{\varphi^4}{4!} \right) \tag{3.7}$$

We quantize the Hamiltonian by writing the number and phase variables as operators.

$$\varphi = \frac{1}{\Phi_0} \sqrt{\frac{\hbar \mathcal{Z}_0}{2}} (a + a^\dagger) \tag{3.8}$$

17

$$n = -i\frac{1}{2e}\sqrt{\frac{\hbar}{2\mathcal{Z}_0}}(a - a^\dagger) \tag{3.9}$$

$a(a^\dagger)$ is the annihilation (creation) operator and $\mathcal{Z}_0 = \sqrt{L/C}$ is the characteristic impedance of the circuit. Recasting the Hamiltonian in terms of the creation and annihilation operators we obtain Equation 3.10.

$$\mathcal{H}/\hbar = \omega_q a^\dagger a + \alpha a^\dagger a(a^\dagger a - 1) \tag{3.10}$$

This Hamiltonian describes a non linear oscillator. The self interaction term at higher order leads to unequally spaced energy levels. The eigenstates of this system are $|g\rangle, |e\rangle, |f\rangle, etc...$ and can be uniquely addressed. The first two levels comprise a qubit which is the central piece of our detector. The qubit is described as a two level system $\mathcal{H} = \frac{1}{2}\omega_q\sigma_z$, with fundamental frequency $\omega_q = \sqrt{8E_JE_C} - E_C$. The anharmonicity of the system, the difference between the first and second transition, is determined by $\alpha = -E_C$.

3.2 Using a qubit to count photons

To count photons, I harness the interaction between a superconducting qubit and a microwave cavity. The Jaynes-Cummings Hamiltonian[49] describes the interactions between a qubit and cavity, and is expressed as $\mathcal{H}/\hbar = \omega_c a^\dagger a + \frac{1}{2}\omega_q\sigma_z + g(\sigma_+ + \sigma_-)(a + a^\dagger)$. ω_c and ω_q are the transition frequencies of the cavity and qubit respectively. g is the dipole coupling between the electric field of the cavity mode and qubit antenna. This coupling can be approximated as $g \sim \mathbf{d} \cdot \mathbf{E}$, where $\mathbf{d}$ is the dipole moment of the qubit and $\mathbf{E}$ is the zero point field of the cavity mode as shown in Figure 3.1.

Note that in practice, the transmon qubit that we construct is not strictly a two-level system, though we only use the sub space of the ground and excited states $|g\rangle, |e\rangle$ with a transition frequency of ω_q. The next transition is between the excited state $|e\rangle$ and the next excited state $|f\rangle$ with a transition frequency of $\omega_q + \alpha$. The difference of these two transitions is characterized by the anharmonicity of the transmon α and allows for unique
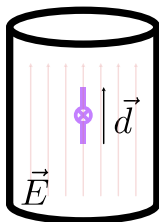
Figure 3.1: **Qubit and cavity coupling**. The interaction between a superconducting quantum bit and the resonant mode of a cavity is well approximated as a dipole coupling. The coupling rate associated with this interaction is $g \sim \mathbf{d} \cdot \mathbf{E}$.

addressability of the first transition without exciting higher order transitions. The anharmonicity is determined by the capacitive energy of the transmon which spacing and size of the transmon pads.

In the dispersive limit where the qubit and cavity detuning ($\Delta = \omega_c - \omega_q$) is much greater than the coupling $\frac{g}{\Delta} \ll 1$, the Jaynes-Cummings Hamiltonian can be analyzed using second order perturbation theory to obtain the approximation shown in Equation 3.11 (see Appendix B).

$$\mathcal{H}/\hbar \approx \omega_c a^\dagger a + \frac{1}{2}\omega_q \sigma_z + 2\chi a^\dagger a \frac{1}{2}\sigma_z \tag{3.11}$$

The interaction term is now dependent only on the number operators $a^\dagger a$ and σ_z and $2\chi = \frac{g^2}{\Delta(\Delta+\alpha)}\alpha$. The Hamiltonian can be recast to elucidate a key feature: a photon number dependent frequency shift (2χ) of the qubit transition shown in Equation 3.12.

$$\mathcal{H}/\hbar = \omega_c a^\dagger a + \frac{1}{2}(\omega_q + 2\chi a^\dagger a)\sigma_z \tag{3.12}$$

The number dependent frequency shift is known as the AC Stark effect and is shown in Figure 3.2. This functions as a mapping of the cavity excitation number to qubit transition frequency. By accurately measuring the qubit frequency, the cavity photon number can be extracted. This is accomplished with a Ramsey type interferometry experiment which is

19
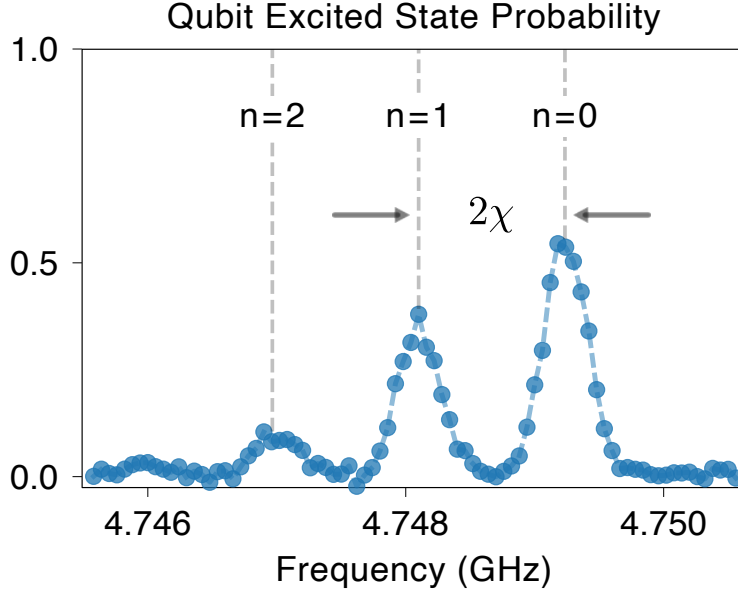
Figure 3.2: **Number splitting**. The cavity population is imprinted on the qubit transition frequency. Here, the coherent state of the cavity results in multiple split peaks in frequency where the qubit has a non zero probability of being excited.

described in Chapter 4.

3.3   Designing a photon counting device

A useful photon counting device consists of a storage cavity to hold the photon while it is counted, a qubit to sense the presence of the photon, and a readout cavity to measure the state of the qubit[50]. Figure 3.3 shows a schematic of the device and Figure 3.4 shows a 3D model.

The interaction rate between the storage cavity and the qubit sets the time required to resolve the cavity photon number. This rate is determined in part by the detuning between the qubit and mode of interest. The interaction rate also determines the Purcell rate, a measure of the loss due to the coupling between two elements. In order to ensure the interaction rate is sufficiently large enough for measuring the photon number, the storage cavity is closest to the qubit in the hierarchy of frequencies. In order to minimize the coupling between the qubit and the higher order modes of both the storage and readout cavities, the
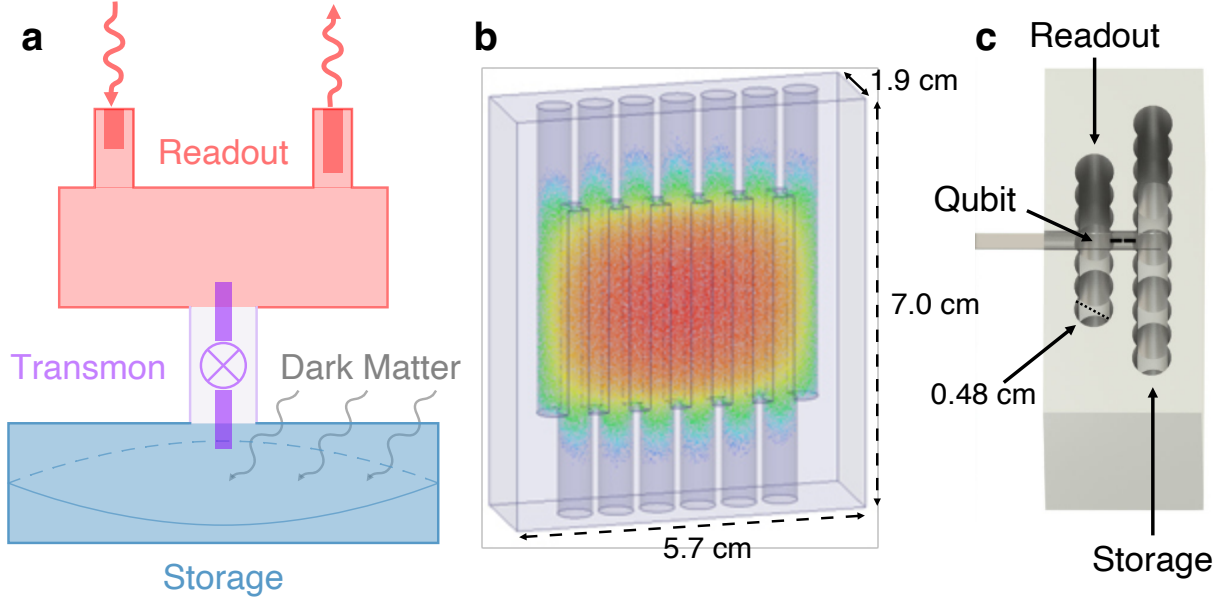
Figure 3.3: **Device schematic, simulation, and rendering**. **a.** A superconducting qubit bridges the storage and readout cavities. The storage is used to hold the dark matter generated photon and the readout is used to measure the state of the qubit. **b.** Electromagnetic simulation of the fundamental mode of the storage cavity. The holes used create the space for the cavity are all sub-wavelength and evanescent, preventing leakage of the field. **c.** 3D rendering of the bottom half of the device shows the storage cavity, the transmon qubit on a sapphire chip, and the readout cavity used to measure the state of the qubit.

qubit frequency is designed to be below the fundamental modes of both cavities. The readout cavity is strongly coupled to the transmission line in order to perform fast measurements of the qubit and is the lossiest element in the system. Therefore, in order to minimize the Purcell induced qubit loss[51], the readout cavity frequency is the highest of all the elements.

3.3.1 Storage cavity

The storage cavity must contain a long lived mode that can contain an excitation for longer than the photon takes to be measured. We employ two strategies for minimizing loss of the cavity excitation. First, the cavity is machined from high purity (99.9999 %) aluminum and operated at cryogenic temperatures such that the metal is superconducting. Second, the design allows for the cavity to be machined from one monolithic field of material, eliminating
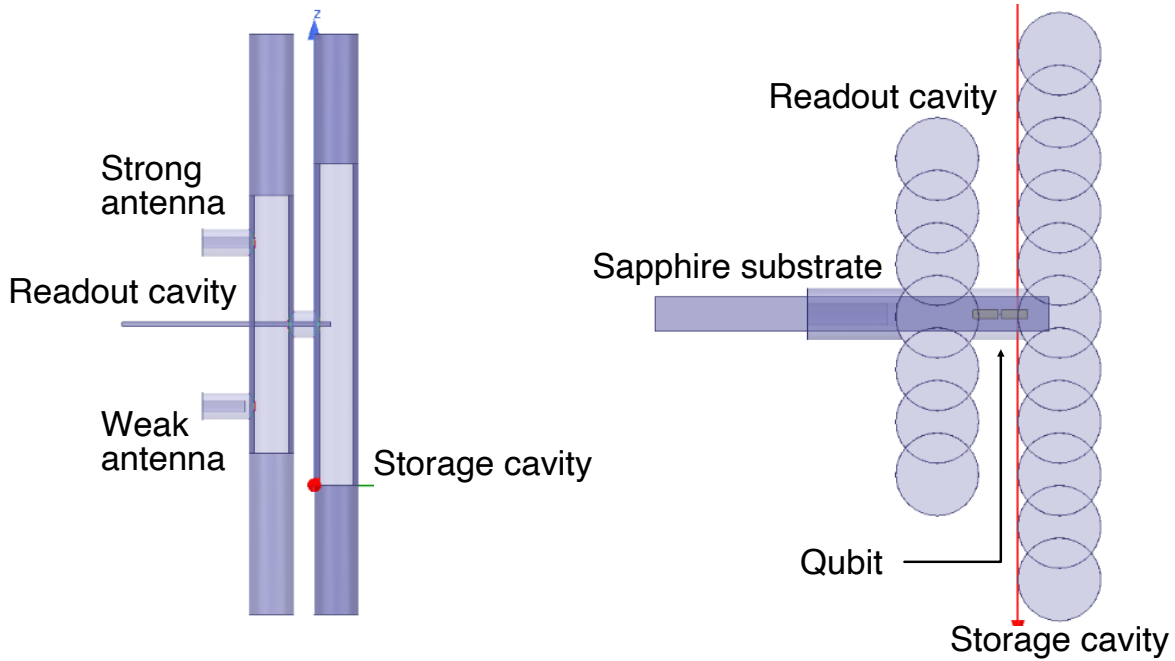
Figure 3.4: **Device design in HFSS**. Side and top view of qubit, storage cavity, and readout cavity simulated in high frequency electromagnetic solver.

the losses typically associated with seams in construction[52].

This is accomplished by drilling offset holes from the top and bottom of the stock material, with an overlapping region in the middle defining the cavity volume. The 0.48 cm (3/16 in) diameter holes are undersized and then brought to size using a ream. To ensure smooth internal surfaces, a series of hones with finer abrasive is used. This technique was developed in the Schuster lab by A. E. Oriani, R. K. Naik, and S. Chakram.

The storage cavity is well approximated as a rectangular box with dimensions $3.48 \times 3.56 \times 0.953 \, \text{cm}^3$, with the holes used in its fabrication as perturbations. The cross section of the box is designed to be as close to a square as possible to maximize the detuning between the lowest order mode and the next lowest mode. The last dimension of the cavity is constrained by the diameter of the drill bit used to produce the holes.

Before final assembly and installation in the fridge, the machined cavity must be processed. It is washed in a soap solution, sonicated in Isopropyl, and rinsed with deionized water. In order to remove the oxidized layer and surface damage caused by the machining

process, the cavity is etched immediately before being assembled. The etch processes consists of soaking the cavity in Transene Aluminum Etch A at $50\,^{\circ}$C with constant agitation for 4 hours with the etchant being replaced at the 2 hour mark.

3.3.2 Readout cavity

In order to efficiently machine the readout cavity and eliminate joints, the readout structure is machined in the same stock material as the storage cavity. A single hole is drilled along the short dimension through the center of both the readout and storage cavities to house the qubit chip.

3.3.3 Transmon qubit

The qubit must couple to the storage cavity to sense the presence of photons and must also couple to the readout cavity to be read out quickly. This is accomplished by designing a qubit that bridges both the storage and readout cavity such that it has an antenna coupling to both systems. Additionally the Josephson energy (E_J) and the capacitive energy (E_C) are chosen to ensure the qubit is in the transmon regime, $\frac{E_J}{E_C} \gg 1$. In this configuration the qubit is insensitive to charge fluctuations[53] which dephase the qubit at a rate shown in Equation 3.13. The rate of qubit dephasing from charge noise is suppressed exponentially in $\frac{E_J}{E_C}$.

$$\Gamma_{\text{charge}} = 2^9 E_C \sqrt{\frac{2}{\pi}} (\frac{E_J}{2E_C})^{5/4} e^{-\sqrt{8E_J/E_C}} \tag{3.13}$$

Qubit design and simulation

The qubit, storage, and readout are simulated with a high-frequency structure simulator (Ansys HFSS). An initial eigenmode simulation is useful in choosing the optimal dimension for the storage and readout cavity to obtain the desired resonances. Observing the simu-
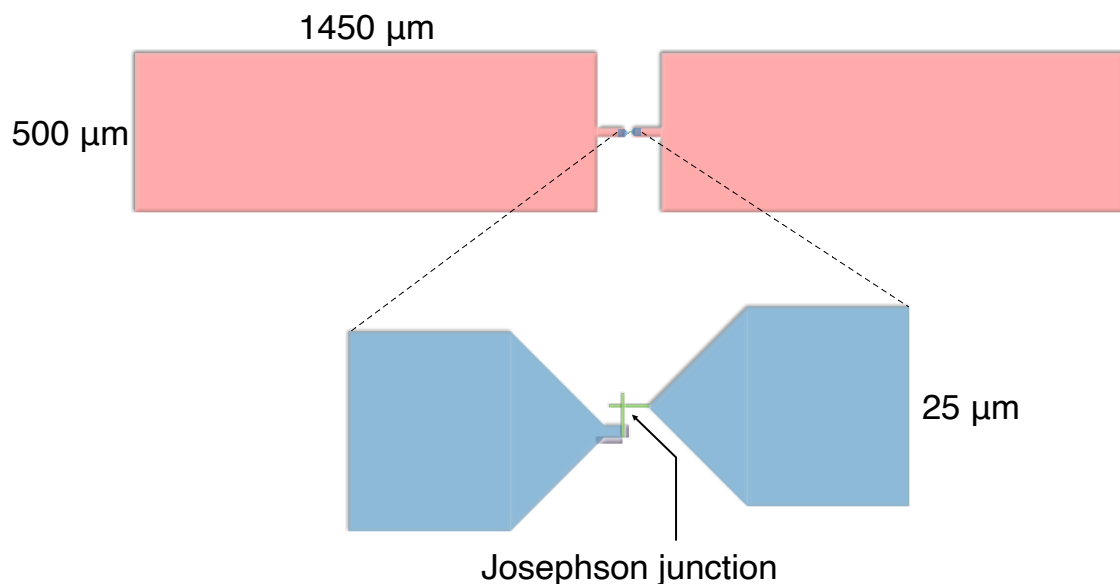
Figure 3.5: **Qubit design**. (Top) Full qubit design including capacitive pads (red) for coupling and Josephson junction (green). (Bottom) Close up on junction region. This component has significantly smaller length scales than the coupling pads, and requires a separate step for fabrication. There is a region of overlap between the first layer of the pads and the second layer (blue) that includes the junction to ensure electrical contact. In addition, the junction in formed by two angled evaporations in directions $90°$ relative to each other. The overlap area is determined by the Josephson energy required for the qubits and is typically in the range of $150 \times 150 \, \text{nm}^2$ to $250 \times 250 \, \text{nm}^2$. To facilitate good contact between the layers and to ensure clean liftoff of the excess metal, there are two undercuts of the resist profile (gray).

lated field provides an indication of where the interaction between mode and qubit will be optimized. The eigenmode simulation also calculates the total quality factor of each mode. This is used to determine if there is significant leakage between the high Q storage cavity and the over coupled readout. In such a situation, the bridge between the two cavities must be extended to minimize coupling the storage cavity mode to the transmission line.

In order to determine the coupling strengths and anharmonicities of the structures, we use the Black-Box formulation[9]. This technique identifies all the resonances of the linear system and then introduces the nonlinearity associated with the Josephson junction as a perturbation. Diagonalizing the perturbed system results in interactions between distinct
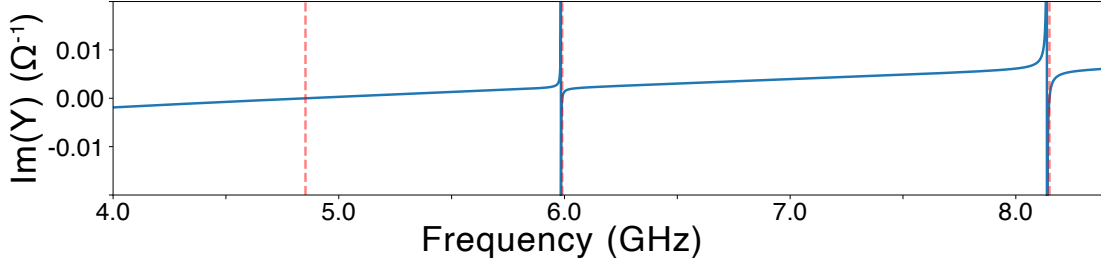
Figure 3.6: **Admittance across Josephson junction**. In order to extract the device parameters, we find the admittance across the Josephson junction. We add the inductive component of the Josephson junction to the response to obtain the admittance shown in blue. The zero crossing determines the resonance frequency of the qubit, storage, and readout shown in dashed red lines. The capacitance C_i of a mode is calculated from the derivative of the admittance evaluated at the resonance frequency. The inductance L_i is determined from the capacitance and the resonance frequency $\omega_i = 1/\sqrt{L_i C_i}$.

modes as well as self interaction. These interactions give rise to the AC Stark shift and anharmonicity of the qubit and cavities.

We include the capacitive structures that form the qubit antenna as well as the sapphire substrate in the HFSS simulation. The qubit design including the Josephson junction is shown in Figure 3.5. We extract the admittance (shown in Figure 3.6) at the location of the Josephson junction to determine the linear components of the circuit. The system is effectively composed of multiple RLC circuits each with a resonance frequency, ω_i, determined form the zero crossing of the imaginary part of the admittance ($\mathrm{Im}[Y]$). We calculate the mode capacitance as $C_i = \frac{1}{2}\mathrm{Im}\left[\frac{dY}{d\omega}\right]\Big|_{\omega_i}$. By introducing higher order terms into the Hamiltonian, we enable nonlinear interactions and calculate the relevant parameters such as anharmonicity and cross Kerr shifts. The simulated and calculated values for the design of the qubit, storage cavity, and readout cavity used in this work are shown in Table 3.1.

The real part of the admittance contains information about the resistive elements of the circuit. We determine the effective resistance using $R_i = \frac{1}{\mathrm{Re}[Y(\omega_i)]}$. The mode quality factors can be calculated as $Q = \omega R C$. This provides the quality factors of the readout and storage resonator as well as the Purcell limit[51] to the qubit lifetime $T_1^{\mathrm{Purcell}} = Q_q/\omega_q$. In order to accurately simulate the real part of the admittance, an additional convergence

25

criteria must be applied to the HFSS simulation to account for the orders of magnitude difference between the real and imaginary parts of the admittance. Our usual strategy is to first perform a simulation across all frequencies to determine all the resonances. Then, we conduct a narrow sweep with high resolution around the qubit frequency to extract the Purcell lifetime.

Device parameter	Simulated value
Qubit frequency	$\omega_q = 2\pi \times 4.683\,\text{GHz}$
Qubit anharmonicity	$\alpha_q = -112\,\text{MHz}$
$\frac{E_J}{E_C}$	196
Storage frequency	$\omega_s = 2\pi \times 5.99\,\text{GHz}$
Storage-Qubit coupling strength	$g_s = 79.9\,\text{MHz}$
Storage-Qubit Stark shift	$2\chi_s = -2\pi \times 1.06\,\text{MHz}$
Readout frequency	$\omega_r = 2\pi \times 8.149\,\text{GHz}$
Readout-Qubit coupling strength	$g_r = 162.1\,\text{MHz}$
Readout-Qubit Stark shift	$2\chi_r = -2\pi \times 0.524\,\text{MHz}$

Table 3.1: **Simulated device parameters**. Simulation of qubit, storage, and readout cavity parameters involves a combination of high frequency finite element modeling and calculation using the Black-Box technique[9].

Fabrication

The transmon qubit shown in Figure 3.7 is fabricated on $430\,\mu\text{m}$ thick C-plane (0001) Sapphire wafers with a diameter of $50.8\,\text{mm}$. Wafers are cleaned with organic solvents (Toluene, Acetone, Methanol, Isopropanol, and DI water) in an ultrasonic bath to remove contamination, then annealed at $1200\,^{\circ}\text{C}$ for 1.5 hours. Prior to film deposition, wafers undergo a second clean with organic solvents (Toluene, Acetone, Methanol, Isopropanol, and DI water) in an ultrasonic bath.

The base layer of the device, which includes the capacitor pads for the transmon, consists of $75\,\text{nm}$ of Nb deposited via electron-beam evaporation at $1\,\text{Å/s}$. The features are defined via optical lithography using AZ MiR 703 photoresist, and exposure with a Heidelberg MLA150
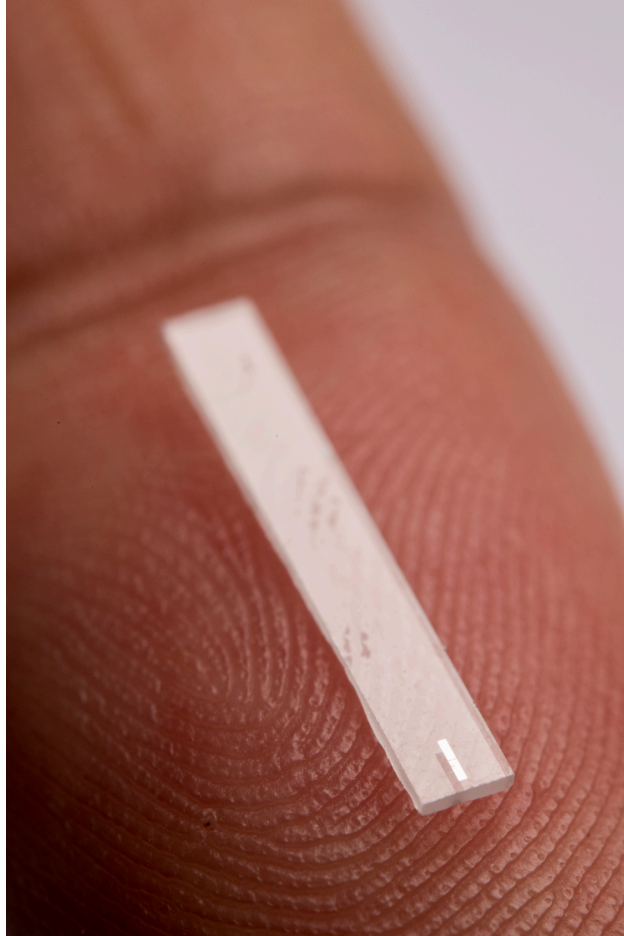
Figure 3.7: **Qubit on sapphire substrate.** The superconducting qubit is embedded in a microscopic antenna that facilitates a coupling between the qubit and microwave cavity. Photograph by Reidar Hahn.

Direct Writer. The resist is developed for 1 minute in AZ MIF 300 1:1 with constant agitation. Since only a small portion of the wafer contains the base metal, the patterns are clearly visible after development.

The features are etched in a Plasma-Therm inductively coupled plasma (ICP) etcher using fluorine based ICP etch chemistry with a plasma consisting of 15 sccm SF_6, 40 sccm CHF_3, and 10 sccm Ar. Since most of the Nb is being etched, the remaining patters will remain while the exposed metal is removed, leaving only the transparent sapphire.

Before proceeding to the Josephson junction patterning, the remaining protective photoresist is removed using N-Methyl-2-pyrrolidone (NMP) at 80 °C. The wafer is cleaned with

Isopropal and DI water. To prevent outgassing during the following steps, the wafer is baked in a vaccuum chamber to remove any excess water. We have found this step is important for the stability of the resist stack used for junction patterning.

The junction mask is defined via electron-beam lithography of a bi-layer resist (MMA-PMMA) in the Manhattan pattern using a Raith EBPG5000 Plus E-Beam Writer, with overlap pads for direct galvanic contact to the optically defined capacitors. The resist stack is developed for 1.5 minutes in a solution of 3 parts IPA and 1 part DI water at 6 °C.

Before junction deposition, the overlap regions on the pre-deposited capacitors are milled *in-situ* with an Argon ion mill to remove the native oxide. The junctions are then deposited with a three step electron-beam evaporation and oxidation process. First, an initial 35 nm layer of aluminium is deposited at 1 nm/s at an angle of 29° relative to the normal of the substrate, parallel azimuthally to one of the fingers in the Manhattan pattern for each of the junctions. Next, the junctions is exposed to 20 mbar of a high-purity mixture of Ar and O_2 (ratio of 80:20) for 12 minutes for the first layer to grow an oxide layer. This is a self terminating process and results in approximately 1 nm of high purity aluminum oxide. Finally, a second 120 nm layer of aluminium is deposited at 1 nm/s, at the same angle relative to the normal of the substrate, but orthogonal azimuthally to the first layer of aluminium. The critical current density of the junction is determined by both the area of the overlap and thickness of the oxide barrier. The dependence is captured in the effective resistance of the junction R and the Josephson energy is $E_J = \frac{\hbar\pi\Delta}{(2e)^2 R}$, where Δ is the superconducting bandgap of aluminum. The junction resistance is inversely proportional to the overlap area and is an exponential function of the oxide thickness.

After evaporation, the remaining resist is removed via liftoff in N-Methyl-2-pyrrolidone (NMP) at 80 °C for 3 hours, leaving only the junctions directly connected to the base layer. After both the evaporation and liftoff, the device is exposed to an ion-producing fan for 15 minutes, to avoid electrostatic discharge of the junctions. The room temperature DC resistance of the Josephson junction of each qubit is measured to select the qubit which

corresponds to the target Josephson energy[54] (E_J).

3.4 Operating a qubit coupled to a cavity

The superconducting cavities and qubit are operated in a cryogenic environment with minimal coupling to the ambient room temperature environment. Here, I describe the hardware used to operate and communicate with the device.

3.4.1 Dilution refrigerator

The device is operated in a cryogenic environment for two main reasons. First, the cavity and qubit materials, niobium and aluminum, only become superconducting at temperatures below $9.3\,\mathrm{K}$ and $1.2\,\mathrm{K}$ respectively. Second, the mitigation of thermal photons is crucial to operating a photon counting experiment with minimal backgrounds. To this end, the device is housed in a Bluefors LD400 dilution refrigerator operating at $8\,\mathrm{mK}$ shown in Figure 3.8. An oxygen-free high thermal conductivity (OFHC) copper mount is directly attached to the body of the device and attached to the base plate of the fridge to ensure thermal coupling. The qubit package is composed of OFHC copper and is coupled to the base plate of the fridge through the same copper mount. The device is also enclosed by a series of nested radiation shields, the first of which is gold plated and heat sunk directly to the base stage of the fridge.

3.4.2 Magnetic and radiation shielding

The qubit and cavity system is housed in two layers of cylindrical μ-metal to shield from stray magnetic fields shown in Figure 3.8. Each layer is thermally coupled to an OFHC copper ring which is screwed into the base plate via copper posts. The top endcap of the shield is removable to insert the device. This screws into the copper mount as well.

In order to prevent high frequency radiation from entering the qubit and cavities, the
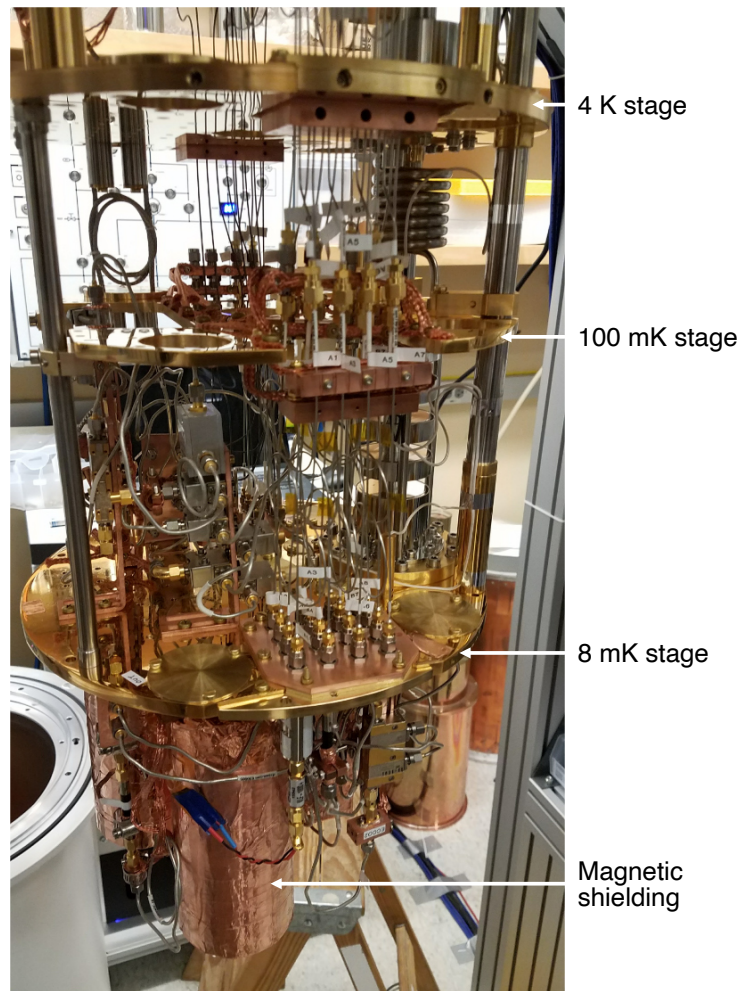
Figure 3.8: **Device in dilution refrigerator.** View of the fridge when open. There are a series of plates each corresponding to a temperature stage. The device is thermalized to the base stage at 8 mK. The attentuators, circulators, filters, and JPA are also coupled to the base state. The HEMT amplifier is at 4 K. A superconducting wire carries the signal from the base stage.

entire device is potted in a block of infrared absorbent material, eccosorb CR-110. A copper sheath supports the eccosorb and provides thermalization.

3.4.3 Microwave control

The wiring and hardware used to control and interrogate the qubit, storage, and readout cavity are shown in Figure 3.9. Performing operations such as qubit initialization or readout

30

requires sending microwave signals, synthesized by an arbitrary waveform generator, to the device. These input lines carrying the signals must be sufficiently attenuated to prevent radiation from higher temperature stages from entering the device at the cold stage. The attenuators are thermalized to suppress stray radiation from each stage. The field probing the readout resonator is injected via the weakly coupled port (shorter dipole stub antenna). Control pulses for qubit, storage cavity, and sideband operation are inserted through the strongly coupled readout port (the longer dipole stub antenna). This line includes a cryogenic microwave attenuator thermalized to the base stage (Courtesy of B. Palmer[1]) and a weak eccosorb (IR filter). Both control lines also contain an inline copper coated XMA attenuator that is threaded to the base state. The signal from the readout resonator is carried along a superconducting NbTi coaxial cable. It reflects off a Josephson parametric amplifier (connected, but not used in this work) before being amplified by a cryogenic HEMT amplifier at the $4\,\mathrm{K}$ stage. There are four isolating devices to route the output signal to the room temperature data acquisition system while preventing stray radiation from higher temperature stages from entering the cavity through the strongly coupled port. The output is filtered, further amplified, and mixed down to DC before being digitized.

31
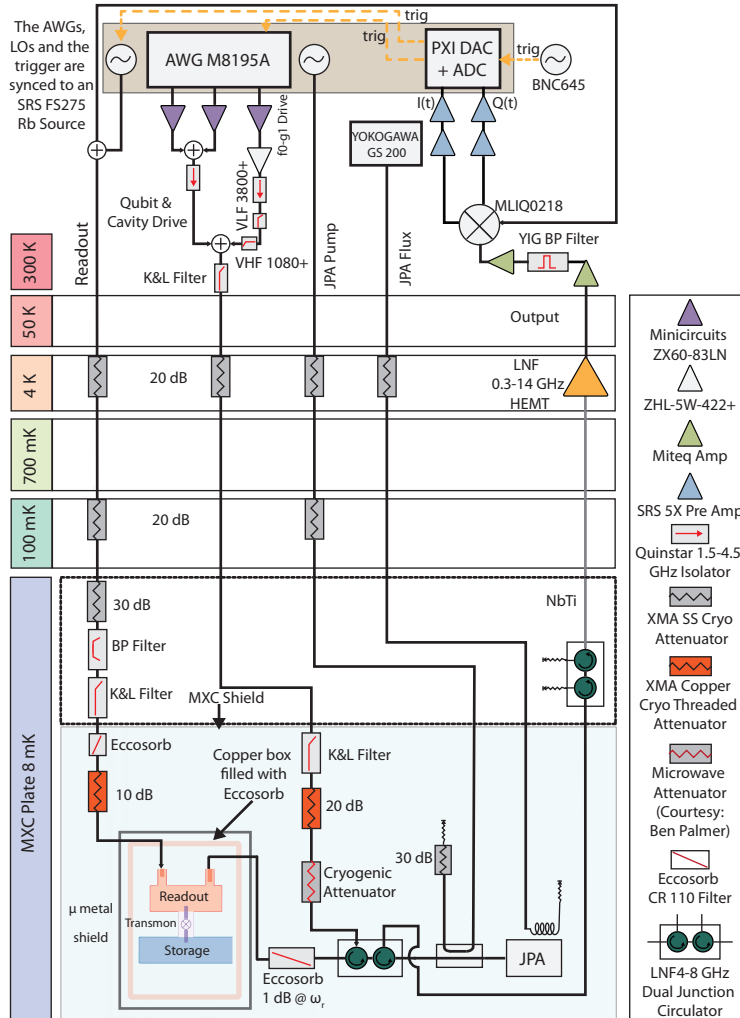
Figure 3.9: **Wiring diagram inside the dilution refrigerator and the room temperature measurement setup.** Qubit readout is performed by injecting a drive into the weakly coupled port. After interacting with the readout cavity, the signal is routed to the amplification chain using non reciprocal circulator and isolator elements. Note, the Josephson parametric amplifier is not in operation for the measurements presented in this work. The signal is then mixed down to DC, further amplified, and finally digitized. Qubit and storage cavity operations are performed via the strongly coupled port. This line is heavily filtered and attenuated[1] to minimize stray radiation from entering the device.

Chapter 4

Measuring the same photon many times

The operating principle of a qubit based sensor for a dark matter experiment is to use the interaction between a superconducting qubit and a photon stored in a high quality factor resonator to make a direct measurement of the resonator state. We take advantage of large coupling strengths that can be engineered between qubit and photon to perform this measurement. Additionally, the nature of the interaction allows us to overcome detector errors inherent to this system.

4.1 Determining photon number parity

In order to determine the number of photons in the cavity, we map the cavity state onto the qubit using Ramsey interferometry[55] as depicted in Figure 4.1. This requires manipulating the state of the qubit. We use the dipole interaction between electric fields and the qubit, which is proportional to σ_x. We apply an external field to rotate the qubit state around the x-axis of the Bloch sphere. Driving for a time such that qubit state, initialized in either $|g\rangle$ or $|e\rangle$, is rotated a quarter turn around the Bloch sphere is called a $\pi_{ge}/2$ pulse ($2\pi/4 = \pi/2$). This leaves the qubit state in a superposition state $\frac{1}{2}(|g\rangle \pm |e\rangle)$. Since the qubit frequency is shifted by 2χ when there is a photon in the cavity, the superposition state precesses at a rate $|2\chi| = 2\pi \times 1.13\,\mathrm{MHz}$ relative to when there are no photons in the cavity. By waiting a time $t_p = \pi/|2\chi|$, the superposition acquires a π phase if there is one photon in the cavity. A $-\pi/2$ pulse projects the qubit back onto the z-axis, completing the cavity state mapping onto the qubit. Using the standard dispersive technique we measure the state of the qubit using the readout resonator. For small cavity displacements ($\bar{n} \ll 1$), this protocol functions as a qubit π pulse conditioned on the presence of a cavity photon. If there are zero photons in the cavity, the qubit is returned to its initial state. If there is one photon in the cavity, the
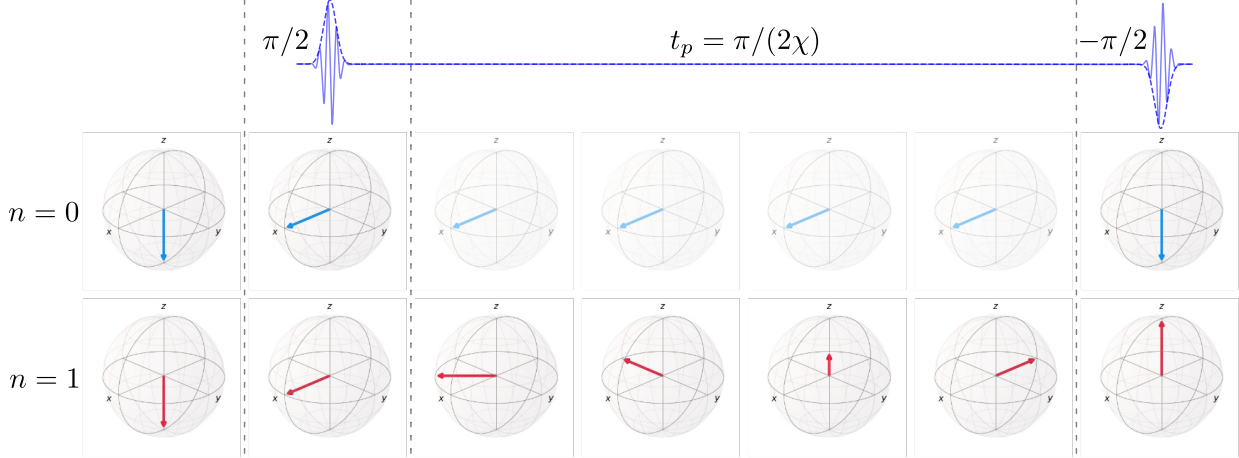
Figure 4.1: **Parity measurement**. The parity measurement maps the cavity number parity onto the state of the qubit. In the case of a weak cavity displacement, zero photons are mapped to the ground state and one photon is mapped to the excited state.

qubit state is flipped ($|g\rangle \leftrightarrow |e\rangle$). More generally, the parity measurement results in a qubit flip for any odd number cavity population. The parity measurement procedure is described in full detail in Appendix C.

4.2 Quantum non-demolition interaction

Though the parity measurement ideally maps the cavity state onto the qubit, there are various possible errors that could result in inefficiencies or worse, false positive detections. These include qubit heating, decay, or dephasing, cavity decay, and readout misassignment. In contemporary transmon qubit systems, these errors occur with probabilities on the order of 0.1-10%. This is much greater than the potential signal probabilities induced by the dark matter. In order to mitigate the effect of these errors on the detector inefficiency and false positive probability, we take advantage of the quantum non-demolition (QND) nature of the cavity-qubit interaction.

The interaction term, $2\chi a^\dagger a \frac{1}{2}\sigma_z$, is composed solely of number operators and commutes with the bare Hamiltonian of the cavity ($\omega_c a^\dagger a$) and the qubit ($\frac{1}{2}\omega_q \sigma_z$). Upon measurement of the cavity state by interaction with the qubit, the cavity state collapses to a Fock state
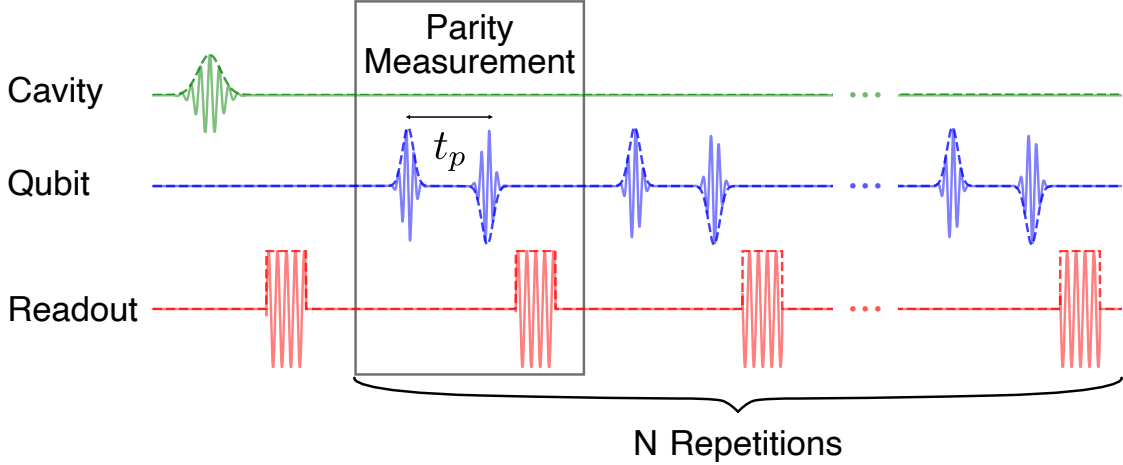
Figure 4.2: **Repeated measurements of cavity state**. The pulse sequence for counting photons includes initializing the cavity followed by a series of parity measurements. Each parity measurement consists of a $\pi/2$ pulse, a wait time of t_p, a $-\pi/2$ pulse, and a qubit state readout.

$|0\rangle$ or $|1\rangle$ (in the $\bar{n} \ll 1$ limit). However, the cavity state is not absorbed or destroyed as a result of the measurement[56–58]. In principle, the resultant Fock state can be measured again.

Repeated measurements of the cavity state via the QND operator enable us to devise a protocol insensitive to errors in any individual measurement[59–61]. Crucially, for the detection of ultra-rare events, we realize an exponential rejection of false positives while incurring only a linear cost in measurement time.

4.3 Measurement protocol

The three components of the measurement protocol shown in Figure 4.2 are cavity initialization, parity measurement, and qubit readout.

4.3.1 Cavity drive

For the purposes of a dark matter search, the cavity initialization is a result of the dark matter induced cavity displacement. This is effectively a translation of the cavity phase

space, resulting in a finite amplitude phasor. The displacement is a result of a classical sinusoidal drive, resulting in a coherent cavity state (quantum mechanical description of a sine wave).

In order to characterize the detector efficiency, I apply a variable displacement to the cavity to simulate a hypothetical signal. The displacement is generated by applying a sinusoidal drive at the storage cavity frequency with a square envelope with a variable length and amplitude to obtain the variable displacement strength. The resulting coherent state can be decomposed into number states with weights given by a Poisson distribution as shown in Equation 4.1.

$$|\alpha\rangle = e^{-\alpha^2/2} \sum_{n=0}^{\infty} \frac{\alpha^n}{\sqrt{n!}} |n\rangle \tag{4.1}$$

To characterize the cavity displacement α, I perform resolved qubit spectroscopy and fit the resulting number peaks with a Poisson distribution to obtain the mean injected cavity population as shown in Figure 4.3. This procedure is an absolute calibration of the mean injected photon number and will be vital to determining the efficiency of photon detection in Chapter 6.

I calibrate the nonlinearities of the signal generator by measuring cavity population as a function of the drive amplitude input to the controller. The mapping shown in Figure 4.4 allows me to inject arbitrary cavity populations.

4.3.2 Qubit pulses

The parity measurement consists of two $\pi/2$ pulses with opposite phases and a $t_p = \pi/|2\chi|$ delay between them. The pulses are generated by driving a microwave tone at the qubit frequency with a Gaussian envelope with $\sigma = 6\,\text{ns}$. We choose the pulse length to be sufficiently small so that the qubit transition is addressable irrespective of the number of photons in the cavity $1/\sigma > 2\chi$. In this case, the pulse bandwidth is $1/\sigma = 167\,\text{MHz}$, much larger than $2\chi/2\pi = 1.13\,\text{MHz}$.
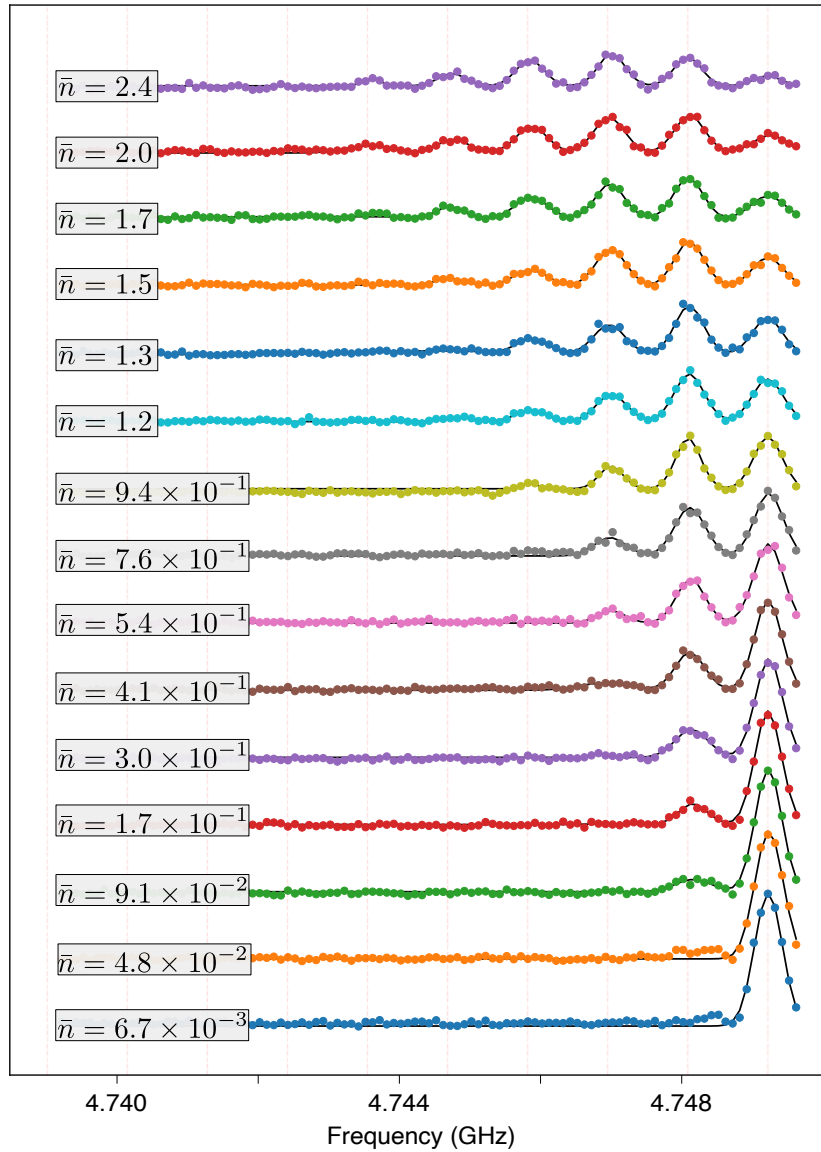
Figure 4.3: **Cavity state via qubit spectroscopy**. The cavity is displaced by applying a variable weak coherent drive. The cavity state is reconstructed by measuring the population in each Fock state by performing qubit spectroscopy (points). The cavity photon number dependent shift of the qubit transition frequency reveals which Fock states are occupied and the peak height corresponds to their weights in the cavity state. By fitting to the spectrum (black) we extract the Poisson weights of the cavity number states in the prepared coherent state and determine the displacement amplitude α and mean cavity population $\bar{n} = \alpha^2$.
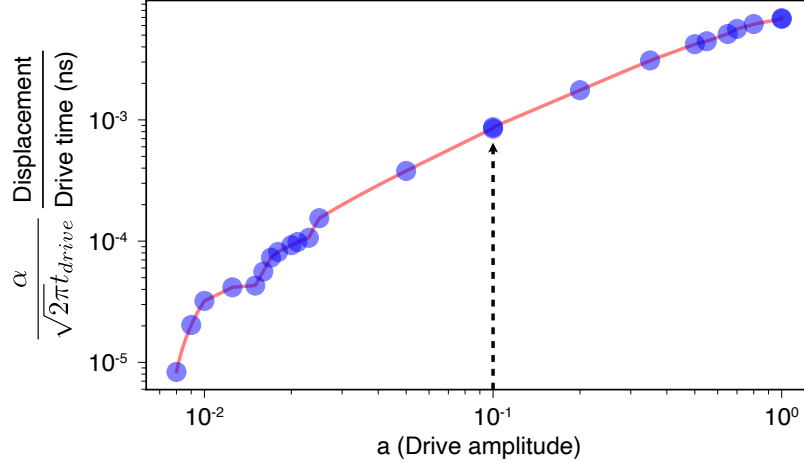
Figure 4.4: **Transfer function describing mapping between drive amplitude in software and cavity displacement.** This transfer function is calibrated such that the cavity is displaced by α when we use a coherent drive of length t_{drive} and amplitude of a (in software) at the cavity frequency. Blue points are obtained by fitting to qubit spectroscopy after applying cavity displacements with variable drive time. For example, a 10ns pulse with a = 0.1 (indicated by the arrow) produces a cavity displacement of $\alpha = 2.1 \times 10^{-1}$. The red curve is a linear interpolation between the data points and can be used to generate displacements that are not directly calibrated. The waveform generator resolution on the amplitudes it can output, is determined by the number of bits in its memory. We use an 8-bit generator, where one bit is used for the sign of the amplitude and the remaining 7 are used to represent the amplitude. As we vary the signal amplitude, the generator exhibits nonlinear behaviors when an additional bit is required to represent the output. The data points are chosen to capture this nonlinear behavior of the waveform generator, at values where an additional bit is necessary to represent the drive amplitude.

4.3.3 Readout

I measure the state of the qubit by probing the readout resonator. By resolving the readout frequency we determine the state of the qubit. To do this, a pulse of $3\,\mu s$ is applied at the readout frequency. After interacting with the cavity, the output is amplified, mixed down, and digitized. I use the resulting I,Q voltages obtained to determine the state of the qubit (see Chapter 5).

4.3.4 Pulse sequence

The experiment begins with a cavity displacement and an initial readout, followed by parity measurement and readout. The parity and readout measurements are repeated a total of $N = 30$ times. After the readout pulse, the resonator must empty before the next parity experiment can be performed. In total, each set of parity and readout measurements takes $10\,\mu s$.

The result of this measurement protocol is a set of $N+1 = 31$ readout signals $(R_0, R_1, ..., R_N)$. Combining the series of readout results with our understanding of the qubit, cavity, and readout I will describe how to reconstruct initial probability of a photon in the storage cavity in Chapter 5.

Chapter 5

Determining the cavity state – hidden Markov model analysis

In order to extract the maximal amount of information from the series of parity measurements, I use a Bayesian analysis[59–61]. A hidden Markov model structure is used to reconstruct the state of the cavity at the outset of the measurement sequence. The analysis tracks all the possible qubit and cavity states and their imperfect measurements that would result in the observed sequence of readouts. With this technique, we realize the exponential suppression of detector false positives achieved by making repeated measurements of the same photon, crucial for detecting the small dark matter signals.

A hidden Markov model (HMM) encapsulates the structure of this experiment as shown in Figure 5.1. A HMM consists of hidden states, their signatures, transitions between hidden states, and emissions of hidden states. In this context, the hidden states are the joint qubit and cavity states and their signatures are the measured readout signals. The transition between hidden states is captured in a transition matrix (T), whose elements are determined by the properties of the device. The emission of the hidden states as a particular signature is characterized by the emission matrix (E), whose elements are related to the fidelity of qubit readout. In this chapter I will discuss how to determine the elements of the transition and emission matrices, how to apply the HMM model to the collected data, and how to reconstruct the initial cavity state efficiently.

5.1   Hidden Markov model structure

The device I use in this work is composed of a storage cavity, qubit, and a readout cavity. The states that are relevant to the photon counting work are $n \in [0, 1]$ for the storage cavity
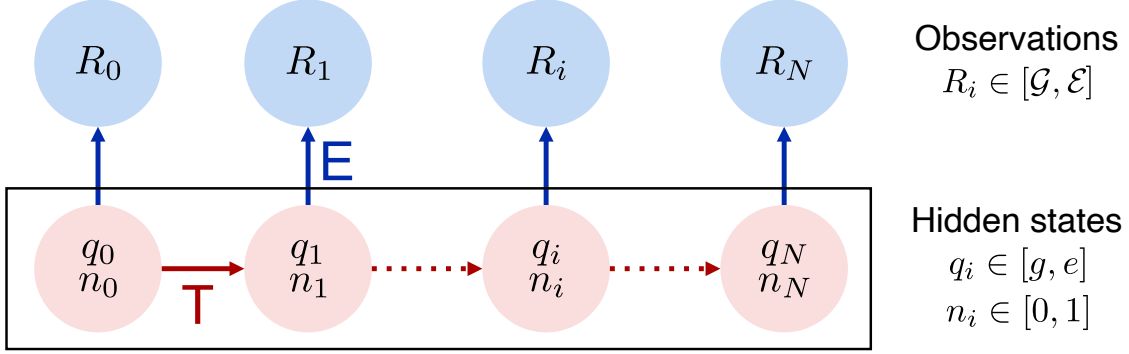
Figure 5.1: **Hidden Markov model structure**. Reconstructing the state of the cavity from the results of the repeated measurements requires a Markov model based analysis. This is comprised of hidden states, cavity (n) and qubit (q) and their observations, readout (R). The relationships between hidden states are encapsulated in the transition matrix, T. The observations from a particular hidden state are encoded in the emission matrix, E.

and $q \in [g, e]$ for the qubit. The joint storage cavity - qubit states are $s \in [0g, 1g, 0e, 1e]$. The readout procedure results in imperfectly determining the state of the qubit as $R \in [\mathcal{G}, \mathcal{E}]$.

5.2   Transition matrix

The transition matrix captures all the possible pathways the joint cavity-qubit state can take between subsequent measurements. The probability of a transition between $s_i \to s_{i+1}$ is given by $\mathrm{T}_{s_i, s_{i+1}}$. $\mathrm{T}_{i,j}$ is the element of the transition matrix in row i and column j.

$$
T = \begin{array}{cccc} |0g\rangle & |0e\rangle & |1g\rangle & |1e\rangle \end{array} \\
\begin{bmatrix} P_{00}P_{gg} & P_{00}P_{ge} & P_{01}P_{ge} & P_{01}P_{gg} \\ P_{00}P_{eg} & P_{00}P_{ee} & P_{01}P_{ee} & P_{01}P_{eg} \\ P_{10}P_{gg} & P_{10}P_{ge} & P_{11}P_{ge} & P_{11}P_{gg} \\ P_{10}P_{eg} & P_{10}P_{ee} & P_{11}P_{ee} & P_{11}P_{eg} \end{bmatrix} \begin{array}{c} |0g\rangle \\ |0e\rangle \\ |1g\rangle \\ |1e\rangle \end{array}
\tag{5.1}
$$

5.2.1 Cavity transitions

There are two processes that can change the state of the cavity between measurements: decay and heating. Over the course of a single $t_m = 10\,\mu s$ measurement the probability of decay from $|1\rangle \to |0\rangle$ is given by $P_{10} = 1 - e^{-t_m/T_1^s}$, where T_1^s is the cavity decay time. The probability of spontaneous cavity heating $|0\rangle \to |1\rangle$ towards the steady state population, $\bar{n}_c$, is given by $P_{01} = \bar{n}_c[1 - e^{-t_m/T_1^s}]$. P_{00} and P_{11} correspond to events where no cavity errors occur, such that probabilities pairwise sum to unity (e.g. $P_{00} + P_{01} = 1$).

Cavity decay

A photon stored in the cavity is lost on a characteristic timescale of T_1^s. These errors are measured by initializing the cavity with $n = 1$ and then probing its state after a variable time. The $|f0\rangle - |g1\rangle$ interaction is used to load the cavity and retrieve the cavity state for measurement[62–65]. The experimental sequence is as follows: qubit π_{ge}, qubit π_{ef}, followed by a $\pi_{|f0\rangle-|g1\rangle}$ to swap the excitation into the cavity, a variable time delay τ, $\pi_{|f0\rangle-|g1\rangle}$ to unload the cavity, and π_{ef} to bring the state back into the measured subspace. A qubit measurement of $\mathcal{G}$ indicates that a photon is no longer in the cavity and a measurement of $\mathcal{E}$ indicates a photon is still present after time τ. The measurement sequence and resulting state during the sequence is shown in Table 5.1 Figure 5.2 shows the photon probability vs τ, which is fit with a decaying exponential with time constant $T_1^s = 546 \pm 23\,\mu s$.

Operation	Qubit-Cavity state $|q, s\rangle$
	$|g, 0\rangle$
π_{ge}	$|e, 0\rangle$
π_{ef}	$|f, 0\rangle$
$\pi_{|f0\rangle-|g1\rangle}$	$|g, 1\rangle$
Wait τ	$|g, 1\rangle$ or $|g, 0\rangle$
$\pi_{|f0\rangle-|g1\rangle}$	$|f, 0\rangle$ or $|g, 0\rangle$
π_{ef}	$|e, 0\rangle$ or $|g, 0\rangle$

Table 5.1: **Cavity decay measurement**. Pulses sequence and joint qubit-cavity states during the measurement of the cavity decay time.

Cavity dephasing

The coherence of the cavity state is not relevant for the HMM analysis since the cavity is only in a number state which has an indeterminate phase due to the number-phase uncertainty relation. However, the dephasing time is important to understanding how the dark matter induced signal coherently or incoherently accumulates in the storage cavity. Measuring this quantity is similar to the decay time procedure, but involves placing the cavity in a superposition $\frac{1}{\sqrt{2}}(|0\rangle + |1\rangle)$. The experiment sequence is qubit $\pi_{ge}/2$, qubit π_{ef}, followed by a $\pi_{|f0\rangle-|g1\rangle}$ to swap the superposition into the cavity, a variable time delay τ, $\pi_{|f0\rangle-|g1\rangle}$ to unload the cavity, π_{ef}, and $\pi_{ge}/2$ to complete the Ramsey interferometry. Figure 5.2 shows the resulting interferomtery fringes, the decay of the sinusoid indicates a dephasing time of $T_2^s = 774 \pm 286\,\mu\text{s}$.

Cavity heating

In this work, only the initial cavity state is important as it determines if the dark matter has successfully deposited a photon in the cavity. Therefore, cavity heating events should be rejected. This can be accomplished by setting $\bar{n}_c = 0$ in the transition matrix. In the reconstruction of the initial cavity state, this penalizes events where a cavity photon appears after the measurement sequence has begun.

5.2.2   Qubit transitions

There are three processes that can result in a qubit error: decay, dephasing, and heating. Over the course of a single $t_m = 10\,\mu\text{s}$ measurement the probability of decay from $|e\rangle \to |g\rangle$ is given by $P_{eg}^{\downarrow} = 1 - e^{-t_m/T_1^q}$, where T_1^q is the qubit decay time. Dephasing errors occur only during parity sequence lasting $t_p = 380\,\text{ns}$ with probability $P^{\phi} = 1 - e^{-t_p/T_2^q}$, where T_2^q is the qubit dephasing time and $t_p \ll T_2^q$. Spontaneous heating $|g\rangle \to |e\rangle$ to the steady state qubit population $\bar{n}_q$ occurs with probability $P_{ge}^{\uparrow} = \bar{n}_q[1 - e^{-t_m/T_1^q}]$. The transition
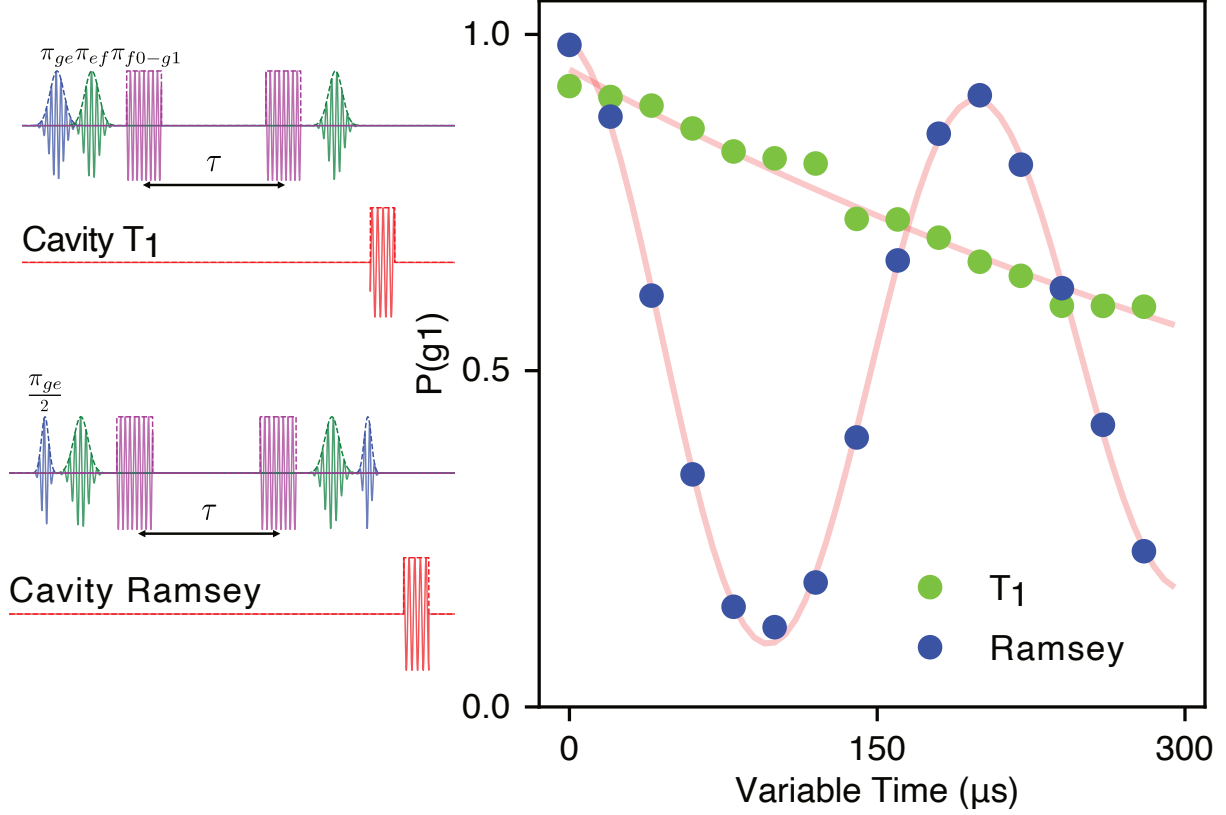
Figure 5.2: **Cavity decay and dephasing**. **Green,** Exponential decay of a cavity photon as a function of measurement delay time with fit in red. Measurement pulse sequence is shown in top left and involves putting one photon in the cavity using the $|f0\rangle - |g1\rangle$ sideband. After a variable delay time, the cavity population is swapped back into the qubit and measured using a readout pulse. The long lived mode of the storage cavity is ideal to hold the photon while it is being repeatedly measured **Blue,** Decaying sinusoid characteristic of an interferometry measurement with fit in red. The measurement pulse sequence is shown in bottom left and involves swapping a qubit superposition state into the cavity. After a variable delay time, the cavity superposition state is swapped back into the qubit and measured using a readout pulse. The long dephasing time of the storage cavity is important for coherent accumulation the dark matter induced signal.

matrix captures all these processes in $P_{ge} = P_{ge}^{\uparrow} + P^{\phi}$ and $P_{eg} = P_{eg}^{\downarrow} + P^{\phi}$. P_{gg} and P_{ee} correspond to events where no qubit errors occur, such that probabilities pairwise sum to unity (e.g. $P_{gg} + P_{ge} = 1$).

44
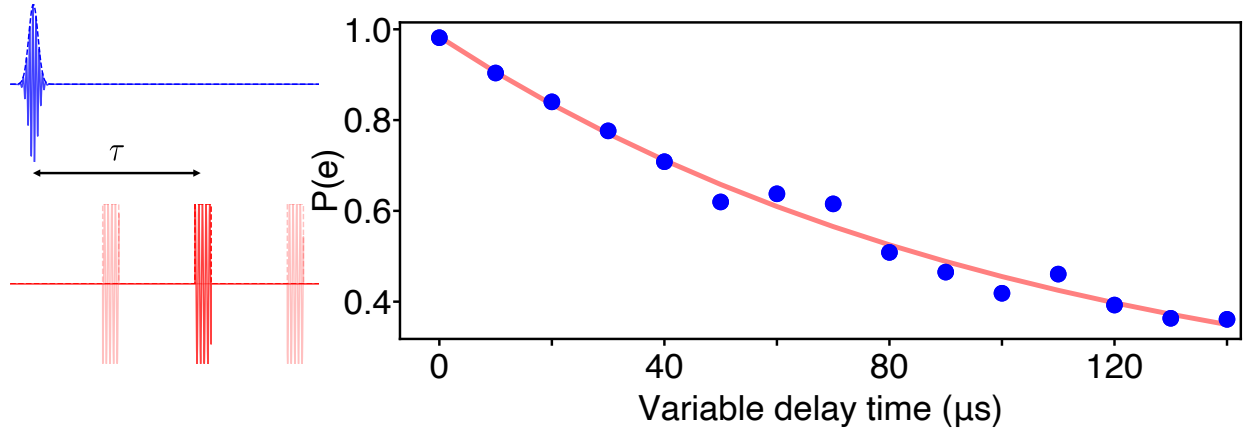
Figure 5.3: **Qubit decay**. **Left.** Pulse sequence for measuring qubit decay time requires first exciting the qubit then measuring the population after a variable time. **Right,** Measurement of qubit decay time in blue dots fit with decaying exponential in red.

Qubit decay

A qubit excitation dissipates on the time scale of T_1^q. This type of error results in a state change of the qubit, exactly the same signature as the presence of a cavity photon. Therefore, qubit decay events constitute false positive signals and it is especially important to account for this error channel. Qubit decay errors are measured by first initializing the qubit in its excited state and then measuring the qubit state after a variable time. The protocol is π_{ge}, variable wait time τ, and a readout of the qubit state. The resulting state probability versus wait time is fit with a decaying exponential to extract $T_1^q = 108 \pm 18\,\mu$s as shown in Figure 5.3.

Qubit dephasing

The qubit superposition used for the photon counting experiment dephases on the time scale of T_2^q. The parity measurement is sensitive to phase accumulated by the qubit which makes it useful in determining the cavity photon number. However, dephasing from other sources can result in qubit errors that are indistinguishable from the photon induced phase accumulation, thus resulting in a false positive detection. A Ramsey interferometry experiment is conducted
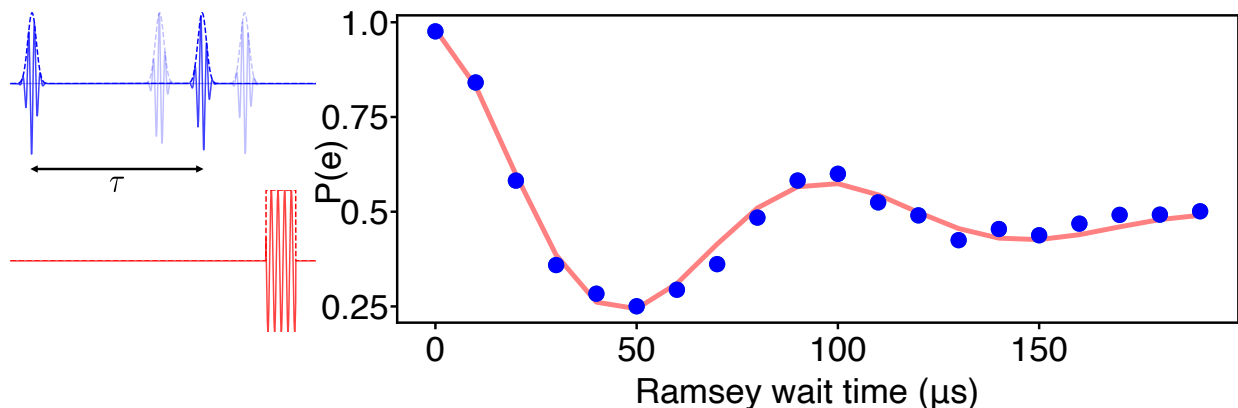
Figure 5.4: **Qubit dephasing**. **Left.** Pulse sequence for measuring qubit dephasing time requires first putting the qubit in its clock state, then waiting a variable time, before finally rotating the qubit back onto the z-axis. **Right,** Measurement of qubit dephasing time in blue dots fit with decaying sinusoid in red.

to determine the dephasing time. The experimental protocol is $\pi_{ge}/2$, variable wait τ, and a final $\pi_{ge}/2$ with its phase advanced by $\omega_r\tau$ where ω_r is the Ramsey frequency. During the variable wait period, slow perturbations of the qubit frequency will dephase the qubit. We are only interested in capturing qubit dephasing on a time scale at least as short as the experiment time. To reduce sensitivity to low frequency sources of dephasing we can apply the spin echo technique used in NMR[66]. A series of π pulses are applied during the wait time of the Ramsey measurement to refocus the qubit. In NMR, faster spins will be leading and slower spins will be trailing, but after the *pi* pulse the situation reverses and the fast spins are able to catch up to the slow spins ahead. One difference between NMR experiment and a qubit is that the ensemble of experiments for qubits exists in time rather than a spatially variant set of spins. The resulting Ramsey fringe is fit with a decaying sinusoid to obtain $T_2^q = 61 \pm 4\,\mu s$ as shown in Figure 5.4.

Qubit heating

The qubit is coupled to various extraneous heat baths that result in a non zero steady state population. The result of qubit heating is identical to a state change due to the
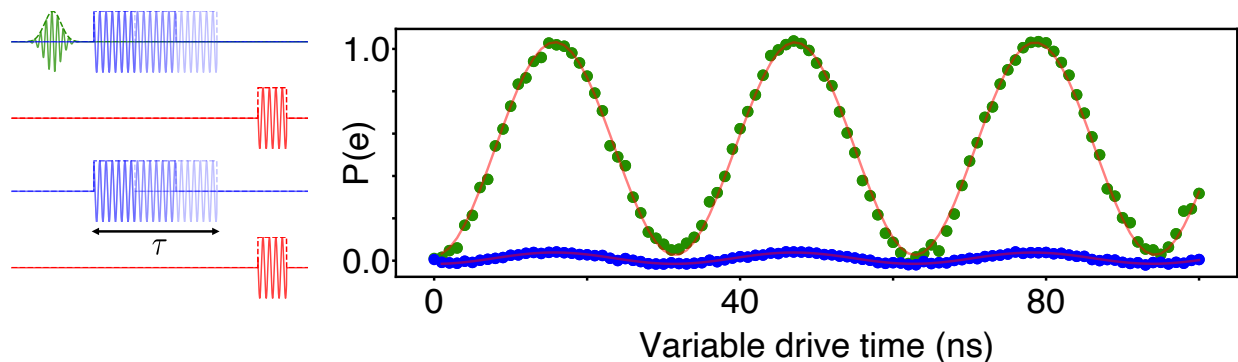
Figure 5.5: **Qubit residual state population**. **Left.** Pulse sequence for measuring qubit excited state population requires applying a π_{ge} pulse and performing a $|e\rangle - |f\rangle$ Rabi oscillation, and the same measurement without the initial π_{ge} pulse. **Right,** Rabi oscillations with π_{ge} are green dots and without π_{ge} are blue dots. Fits are in red.

presence of a photon. Therefore, accounting for heating errors is vital to accurately model the measurement sequence. This is accomplished by performing two experiments to measure the relative population of the qubit ground $|g\rangle$ and excited $|e\rangle$ states[67].

Measuring the qubit spurious population requires using a Rabi measurement where the qubit is driven for a variable amount of time so that it can undergo a coherent oscillation between two states. In this experiment I use two higher order levels of the qubit and the drive frequency is chosen to match the transition between them. First, I perform Rabi oscillations between the second and third levels of the transmon ($|e\rangle \leftrightarrow |f\rangle$) by driving at $\omega_{ef} = \omega_{ge} + \alpha$. In the second experiment, I invert the population of $|g\rangle$ and $|e\rangle$ with a π_{ge} pulse before performing the $|e\rangle \leftrightarrow |f\rangle$ Rabi oscillation. Both sequences and resulting Rabi oscillations are shown in Figure 5.5. The relative amplitudes of the resulting oscillations gives the ratio of the $|e\rangle$ and $|g\rangle$ populations, r. Assuming the qubit temperature is low enough that only the first two levels of the transmon are occupied, gives two equations: $r = \frac{P(|e\rangle)}{P(|g\rangle)}$ and $P(|g\rangle) + P(|e\rangle) = 1$. This yields the excited state population

$$\bar{n}_q = P(|e\rangle) = \frac{r}{r+1}. \tag{5.2}$$

47

The effective qubit temperature is obtained from the Boltzmann factor

$$\frac{P(e)}{P(g)} = r = e^{-\hbar\omega_q/k_B T_q}$$

$$k_B T_q = -\frac{\hbar\omega_q}{ln(r)}.$$

(5.3)

I measure $\bar{n}_q = 5.1 \pm 0.3 \times 10^{-2}$ and $T_q = 78.0 \pm 1.7\,\mathrm{mK}$.

5.2.3   Evaluating transition matrix

This series of independent experiments allows for calibration of all the possible state transitions and their probabilities. Evaluating these probabilities, the transition matrix is

$$T = \begin{array}{cccc} |0g\rangle & |0e\rangle & |1g\rangle & |1e\rangle \end{array}$$

$$T = \begin{bmatrix} 0.989 & 0.011 & 0 & 0 \\ 0.094 & 0.906 & 0 & 0 \\ 0.018 & 1.94 \times 10^{-4} & 0.011 & 0.971 \\ 1.71 \times 10^{-3} & 0.0164 & 0.889 & 0.093 \end{bmatrix} \begin{array}{c} |0g\rangle \\ |0e\rangle \\ |1g\rangle \\ |1e\rangle \end{array}$$

(5.4)

5.3   Emission matrix

The emission matrix captures the possible readout signals that can occur for a given cavity-qubit state. The probability of observing a readout R given the cavity-qubit state is s, is determined by $E_{s,R}$. $E_{i,j}$ is the element of the emission matrix in row i and column j.

$$E = \frac{1}{2} \begin{array}{cc} \mathcal{G} & \mathcal{E} \end{array}$$

$$E = \frac{1}{2} \begin{bmatrix} F_{g\mathcal{G}} & F_{g\mathcal{E}} \\ F_{e\mathcal{G}} & F_{e\mathcal{E}} \\ F_{g\mathcal{G}} & F_{g\mathcal{E}} \\ F_{e\mathcal{G}} & F_{e\mathcal{E}} \end{bmatrix} \begin{array}{c} |0g\rangle \\ |0e\rangle \\ |1g\rangle \\ |1e\rangle \end{array}$$

(5.5)

5.3.1 Readout shift
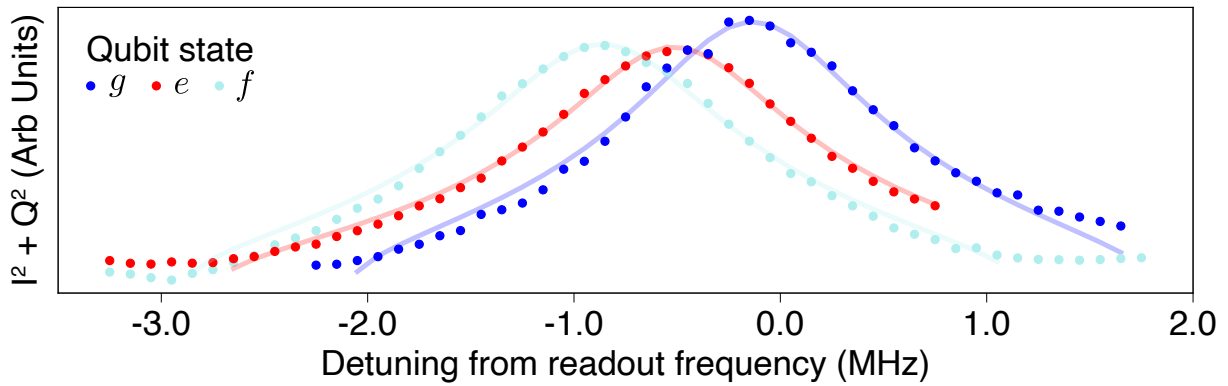
Figure 5.6: **Readout shift** Readout cavity frequency shifts in response to the qubit state. Spectroscopy of the readout while the qubit is in $|g\rangle$, $|e\rangle$, or $|f\rangle$, reveals the shifting transition frequency. The quadrature signals (I,Q) are digitized and combined to obtain the transmission magnitude squared $I^2 + Q^2$. The data is fit with Lorentzian lineshape, shown as solid lines.

The readout cavity frequency shifts in response to different qubit states. Probing the readout resonator in transmission and measuring the response allows us to distinguish the different qubit states. The readout shift is obtained by performing spectroscopy of the readout cavity transition with the qubit in the $|g\rangle$, $|e\rangle$, or $|f\rangle$ and comparing the central frequencies of the line. I determine that relative to the $|g\rangle$ response, the shift due to $|e\rangle$ is $2\chi_r^e = -2\pi \times 0.38\,\mathrm{MHz}$ and due to $|f\rangle$ is $2\chi_r^f = -2\pi \times 0.73\,\mathrm{MHz}$ as shown in Figure 5.6

5.3.2 Readout fidelities

The probability of obtaining the correct readout is given by the readout fidelity, $F_{g\mathcal{G}}, F_{e\mathcal{E}}$. Readout errors occur due to infidelity of the measurement, $F_{g\mathcal{E}}, F_{e\mathcal{G}}$, and are indistinguishable from state change errors.

In order to determine the readout fidelities, the transmon is prepared in its three possible states ($|g\rangle$, $|e\rangle$, $|f\rangle$), 3000 times for each state. By linearly amplifying the signal we measure the I,Q observables as described in Chapter 2. The resulting readout I,Q voltages are used
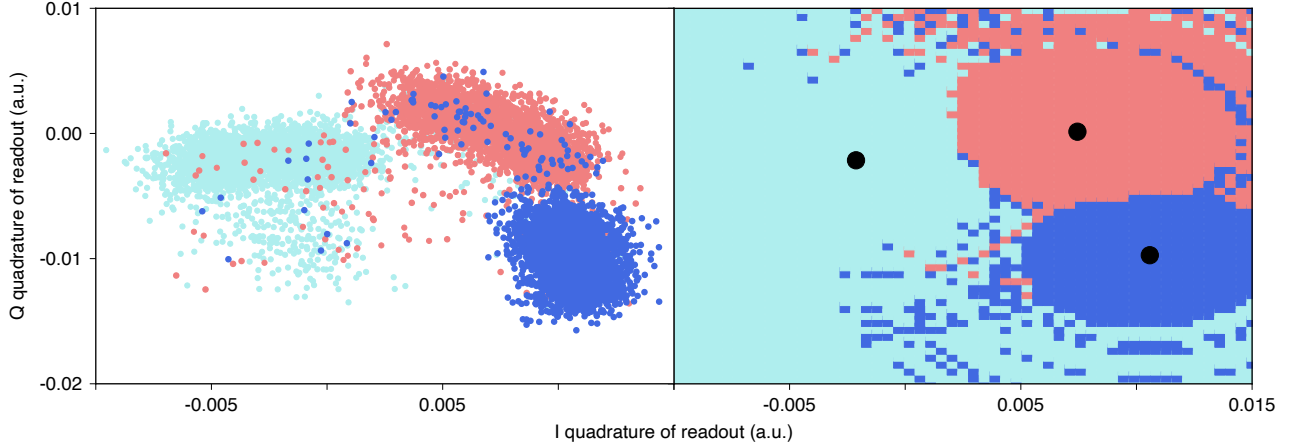
Figure 5.7: **Mapping of readout measurements to transmon states.** (Left) Transmon is prepared in one of its possible states ($\lvert g \rangle$, $\lvert e \rangle$, $\lvert f \rangle$ in blue, red, cyan) 3000 times each and the corresponding readout signals are recorded. (Right) Map that takes a measurement (point in I,Q space) and returns a readout signal, $\mathcal{G}$, $\mathcal{E}$, or $\mathcal{F}$. All measurements that fall outside of the subspace of $\lvert g \rangle$ and $\lvert e \rangle$ are assigned to $\lvert f \rangle$ since the parity measurement only makes use of the first two levels of the transmon.

as a map to calculate the probability of any measured signal being from $\lvert g \rangle$, $\lvert e \rangle$, $\lvert f \rangle$. Based on the probabilities determined from the mapping, an arbitrary measured signal is assigned to either $\mathcal{G}$, $\mathcal{E}$, or $\mathcal{F}$. The measured readout distribution and associated mapping is shown in Figure 5.7. Events where the transmon is prepared in $\lvert g \rangle$ ($\lvert e \rangle$), but are mapped to $\mathcal{E}$ ($\mathcal{G}$) contribute to the readout infidelity.

Readout errors occur due to either voltage excursions from amplifier noise or spurious qubit transitions. The emission matrix should only contain readout errors that occur due to voltage fluctuations since errors due to qubit state transitions during the readout window are accounted for in the transition matrix. To disentangle the two contributions, the readout infidelity is computed by subtracting the qubit error probabilities during the $3\,\mu\mathrm{s}$ readout window due to qubit decay $(1 - e^{-3\,\mu\mathrm{s}/T_1^q})$ or heating $(\bar{n}_q[1 - e^{-3\,\mu\mathrm{s}/T_1^q}])$ from the total measured error during readout, leaving only readout errors due to voltage noise from amplifiers. This is the readout infidelity used to determine the elements of the emission matrix in the analysis. I obtain $F_{g\mathcal{G}} = 95.8 \pm 0.4\,\%$ and $F_{e\mathcal{E}} = 95.3 \pm 0.5\,\%$.

The factor of 1/2

The emission matrix contains the readout fidelities and infidelities, but also a factor of $1/2$ in front. The elements of the emission matrix represent only a marginal distribution since there is no dependence of the readout on the state of the cavity. For example, $F_{g\mathcal{G}} = P(G|g) = P(G|g0)+P(G|g1)$. Since the readout is independent of the cavity state, $P(G|g0) = P(G|g1)$, such that $P(G|g) = 2P(G|g0)$. This implies that the $E_{|g0\rangle,\mathcal{G}} = \frac{1}{2}F_{g\mathcal{G}}$.

5.3.3 Evaluating the emission matrix

I obtain the elements of the emission matrix by measuring the readout fidelities with the generated map and subsequent correction to account for qubit errors.

$$
E = \begin{matrix} & \mathcal{G} & \mathcal{E} & \\ & \begin{bmatrix} 0.479 & 0.021 \\ 0.023 & 0.477 \\ 0.479 & 0.021 \\ 0.023 & 0.477 \end{bmatrix} & \begin{matrix} |0g\rangle \\ |0e\rangle \\ |1g\rangle \\ |1e\rangle \end{matrix} \end{matrix}
\tag{5.6}
$$

5.4   Summary of device properties

In order to accurately fill out the transition and emission matrices integral to the hidden Markov model, it is necessary to keep track of the qubit, storage cavity, and readout cavity properties. In Table 5.2, I summarize the relevant parameters and their independently measured values used in this work.

5.5   Reconstructing the cavity state

The hidden Markov model structure provides a method to obtain the cavity state probabilities at the outset of the measurements sequence. This calculation involves following all

Device Parameter	Measured Value	Designed Value
Qubit frequency	$\omega_q = 2\pi \times 4.749\,\text{GHz}$	$2\pi \times 4.683\,\text{GHz}$
Qubit anharmonicity	$\alpha_q = -139.5\,\text{MHz}$	$-112\,\text{MHz}$
Qubit decay time	$T_1^q = 108 \pm 18\,\text{μs}$	
Qubit dephasing time	$T_2^q = 61 \pm 4\,\text{μs}$	
Qubit residual occupation	$\bar{n}_q = 5.1 \pm 0.3 \times 10^{-2}$	
Storage frequency	$\omega_s = 2\pi \times 6.011\,\text{GHz}$	$2\pi \times 5.99\,\text{GHz}$
Storage decay time	$T_1^s = 546 \pm 23\,\text{μs}$	
Storage dephasing time	$T_2^s = 774 \pm 286\,\text{μs}$	
Storage-Qubit Stark shift	$2\chi = -2\pi \times 1.13\,\text{MHz}$	$-2\pi \times 1.06\,\text{MHz}$
Storage residual occupation	$\bar{n}_q = 7.3 \pm 2.9 \times 10^{-4}$	
Readout frequency	$\omega_r = 2\pi \times 8.052\,\text{GHz}$	$2\pi \times 8.149\,\text{GHz}$
Readout $|e\rangle$ shift	$2\chi_r^e = -2\pi \times 0.38\,\text{MHz}$	$-2\pi \times 0.524\,\text{MHz}$
Readout $|f\rangle$ shift	$2\chi_r^f = -2\pi \times 0.73\,\text{MHz}$	
Readout fidelity (g)	$F_{g\mathcal{G}} = 95.8 \pm 0.4\,\%$	
Readout fidelity (e)	$F_{e\mathcal{E}} = 95.3 \pm 0.5\,\%$	

Table 5.2: **Device parameters**. Measured qubit, storage, and readout cavity parameters. These independently measured values are necessary to determine for the transition and emission matrices. This enables the hidden Markov model to capture the behavior of the system during the measurement sequence.

the possible paths that the qubit and cavity states could such that their imperfect measurements would result in the observed readout sequence $(R_0, R_1, ..., R_N)$. This is represented in Equation 5.7 and is efficiently computed using the backward algorithm as described in Appendix D.

$$P(n_0) = \sum_{s_0 \in [|n_0,g\rangle, |n_0,e\rangle]} \sum_{s_1} ... \sum_{s_N} E_{s_0,R_0} T_{s_0,s_1} E_{s_1,R_1} ... T_{s_{N-1},s_N} E_{s_N,R_N} \qquad (5.7)$$

The inner set of N sums of the qubit-cavity states s_i account for the various possible state changes as well as the emissions during each observation. Since the goal of this reconstruction is to determine the initial cavity state, there is an additional sum over the two possible qubit states.

Take for example the situation where an initial observation of $\mathcal{G}$ is followed by $\mathcal{E}$. We can
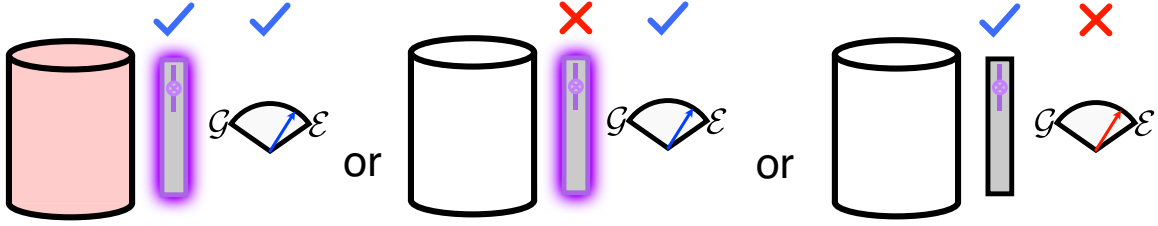
Figure 5.8: **Terms in state reconstruction**. The reconstruction of the cavity state using the hidden Markov model accounts for all possible processes that would result in the measured observation sequence. Here, I depict the three possible processes that could lead to the observation sequence $[\mathcal{G}, \mathcal{E}]$

enumerate the various processes that would have resulted in this particular measurement sequence (shown in Figure 5.8) and associated probabilities that would go into the reconstruction. This measurement sequence could be due to the correct detection of a photon in the cavity (with probability $P_{11}P_{gg}F_{e\mathcal{E}}/2$), a qubit heating event ($P_{00}P_{ge}F_{e\mathcal{E}}/2$) or a readout error ($P_{00}P_{gg}F_{g\mathcal{E}}/2$).

5.5.1   Likelihood test

To determine the initial cavity state I compare the reconstructed state probabilities using a likelihood ratio test.

$$\lambda = \frac{P(n_0 = 1)}{P(n_0 = 0)} \tag{5.8}$$

If the likelihood ratio is below a threshold, $\lambda < \lambda_{\text{thresh}}$, the cavity is determined to contain no photons. If the likelihood ratio is above a threshold, $\lambda > \lambda_{\text{thresh}}$, the cavity is determined to contain a photon. For example, a likelihood ratio of $\lambda = 1$ indicates that the cavity is equally likely to have zero or one photons.

The threshold for determining the presence of a photon sets the false positive probability due to detector errors. The detector induced false positive probability (δ_{det}) can be decreased by increasing the threshold for detection.

$$\delta_{\text{det}} = \frac{1}{\lambda_{\text{thresh}} + 1} \tag{5.9}$$

When the threshold is set high, there is a cost to detection efficiency since it requires more successful measurements. However, this cost is acceptable since the the false positives probabilities are exponentially suppressed with more measurements.

5.5.2 Two examples of the HMM in action

We can observe the effectiveness of the hidden Markov model analysis by looking at two example measurement sequences. The effectiveness of this measurement protocol and associated Bayesian analysis is evident in the reconstructed probabilities.

No cavity photon

In the sequence shown in Figure 5.9, the readout is recorded as $\mathcal{G}$ consistently over the 30 repeated parity measurements. There are no qubit state changes observed, indicating the absence of a cavity photon. This is reflected in the reconstructed probabilities as the probability of an initial cavity photon is $P(n_0 = 1) < 0.1$ after 30 measurements.

A cavity photon

The sequence in Figure 5.10 shows the qubit state changing with almost every measurement between $\mathcal{G}$ and $\mathcal{E}$. This is a clear signature of the presence of a cavity photon. Although there is error in the 9th measurement, I am able to successfully reconstruct the cavity state with high likelihood since there are many more successful measurements. The state reconstruction shows that there is a high probability that there was a photon in the cavity during the initial measurement. More importantly, the probability of zero cavity photons exponentially decreases with more measurements. The probability of a series of detector errors conspiring to produce the observed 30 measurement sequence is $P(n_0 = 0) < 10^{-14}$.
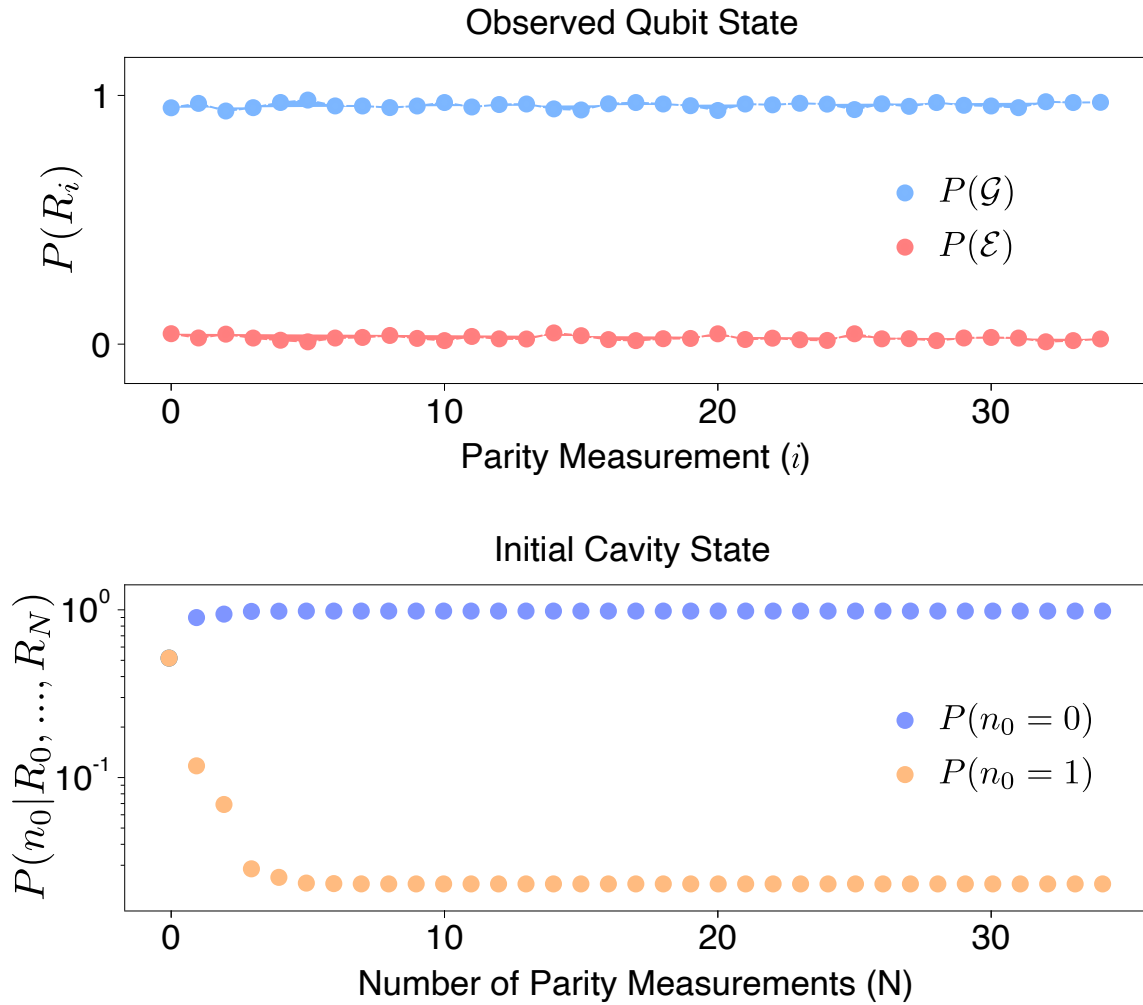
Figure 5.9: **No cavity photon**. Readout sequence and reconstructed initial cavity state. In this example, we see that the probability of an initial cavity photon is small.
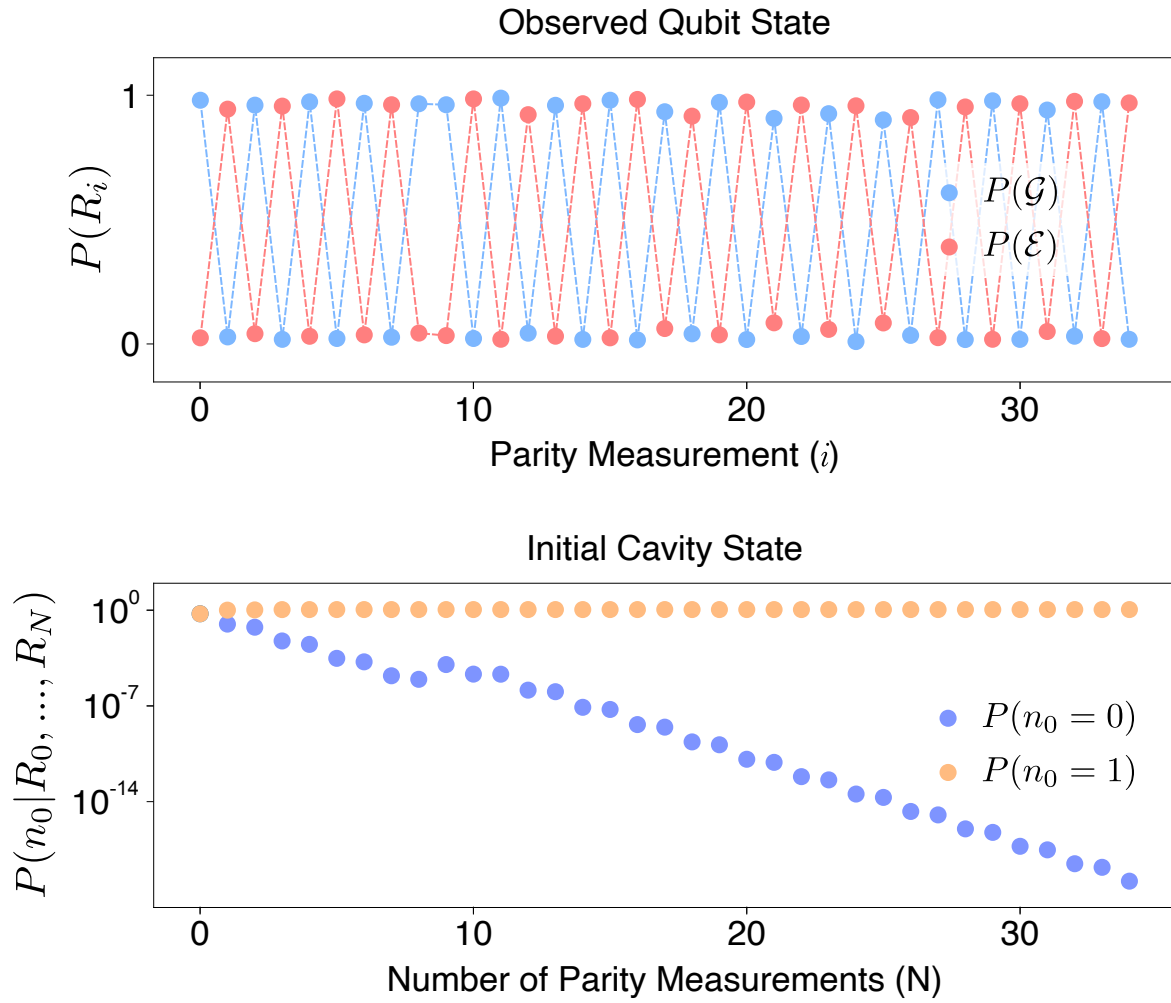
Figure 5.10: **One cavity photon**. Readout sequence and reconstructed initial cavity state. In this example, we see that the likelihood of an initial cavity photon is high.

Chapter 6

Characterizing the qubit based photon counter

6.1 Performance of photon counting protocol

The detector performance is evaluated by injecting a calibrated photon population into the cavity and counting cavity photons using the procedure described in Chapters 4 and 5.

For a calibrated variable injected mean cavity population ($\bar{n}_{\text{inj}}$), a series of 30 repeated parity measurements are performed. The initial cavity state probabilities are reconstructed using the hidden Markov model analysis. A likelihood ratio is computed from these probabilities and compared against a variable threshold to determine if the measured sequence was the result of a photon in the cavity. The measured photon probability $\bar{n}_{\text{meas}}$ at a given $\bar{n}_{\text{inj}}$ is determined by the ratio of the number of photons counted and the measurements performed.

At any fixed threshold the detector efficiency and false positive probability are obtained by fitting the relationship between the injected and measured photon probabilities. The form of the fitting function is given in Equation 6.1.

$$\bar{n}_{\text{meas}} = \eta \times \bar{n}_{\text{inj}} + \delta \tag{6.1}$$

In Figure 6.1 I show this relationship and fit for a threshold of $\lambda_{\text{thresh}} = 10^5$.

6.1.1 Detector efficiency

The prefactor in front of $\bar{n}_{\text{inj}}$ characterizes the efficiency of detection. For a given threshold, a photon is detected with probability η. In Figure 6.2 we see that as the threshold increases, the efficiency is reduced. This is expected since a successful measurement of a photon will require fewer and fewer errors in order to pass the strict criteria set by an increasing threshold.
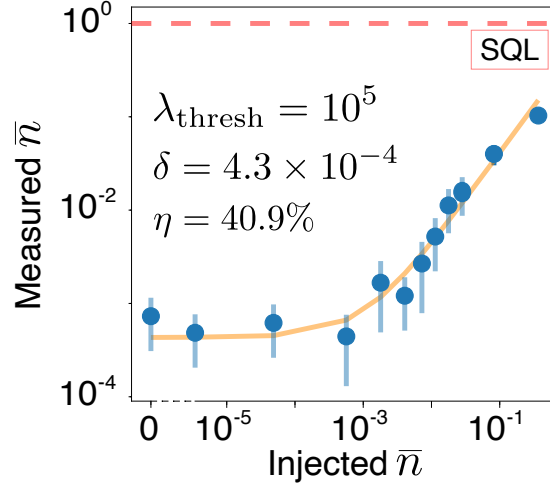
Figure 6.1: **Counting photons with a qubit**. After a variable initial cavity displacement, 30 repeated parity measurements of cavity photon state are performed. The resulting readout sequence is analyzed with the hidden Markov model and a threshold λ_{thresh} is applied to determine the cavity population. The detector efficiency (η) and false positive probability (δ) are determined from the fit in orange using the fitting function shown in Equation 6.1. The dashed red line corresponds to the standard quantum limit (SQL), which results in the noise-equivalent of one photon occupation[2] ($\frac{1}{2}$ from uncertainty of measuring non commuting observables and $\frac{1}{2}$ from amplifier added noise, see Appendix A). We have the ability to detect a single mode photon populations with sub-SQL sensitivity.
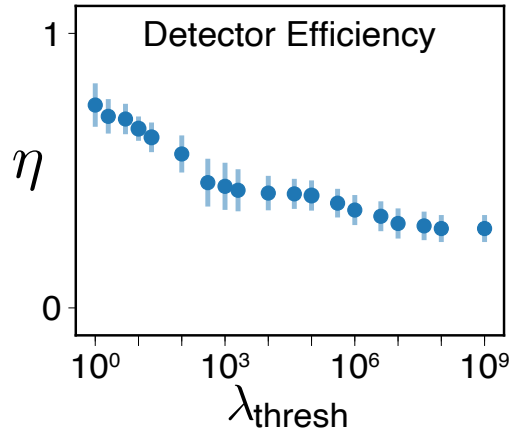
Figure 6.2: **Detector efficiency**. As the threshold for detection increases, the tolerance for qubit based errors is reduced and the quantum efficiency decreases.

58
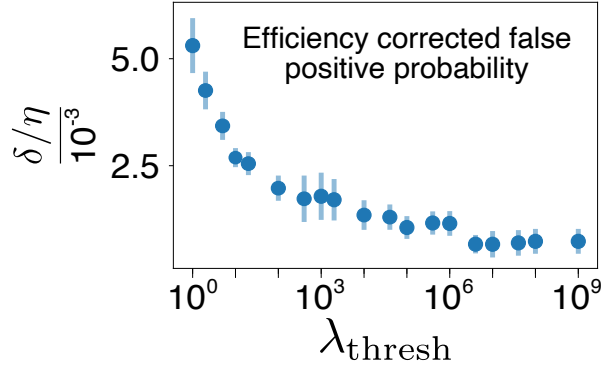
Figure 6.3: **Efficiency corrected false positive probability**. At low thresholds, the false positive probability decreases with increasing threshold. This indicates successful suppression of detector errors being identified as true photon counts. At high thresholds, the efficiency corrected false positive probability (δ/η) versus threshold (λ_{thresh}) curve asymptotes, indicating detector errors are now a subdominant contribution to the total detector false positive probability.

6.1.2 Detector false positive probability

The additive factor in the fit function represents possible false positive counts. These events are either due to a false detection of a photon due to detector errors or the correct detection of an unexpected background photon. The first of these types of errors can be reduced by increasing the threshold for detection. To determine what threshold is required to operate in the regime of background dominated false positives, I plot the efficiency corrected false positive probability (δ/η) as a function of the variable threshold applied, as shown in Figure 6.3. As the threshold is initially increased, δ/η decreases, indicating a suppression of detector errors contributing to false positives. Eventually, δ/η asymptotically reaches a steady value of $\bar{n}_s = 7.3 \pm 2.9 \times 10^{-4}$ even as the threshold is increased. This indicates that the events being measured are not a series of detector errors, but rather a background of real photons. Therefore, operating the detector with a threshold $\lambda_{\text{thresh}} = 10^5$ is sufficient to suppress the detector based errors below the measured backgrounds.

I generate a histogram of the likelihood ratios of events for two different $\bar{n}_{\text{inj}}$ as shown in Figure 6.4 and clearly see that the measured false positives are a result of real background
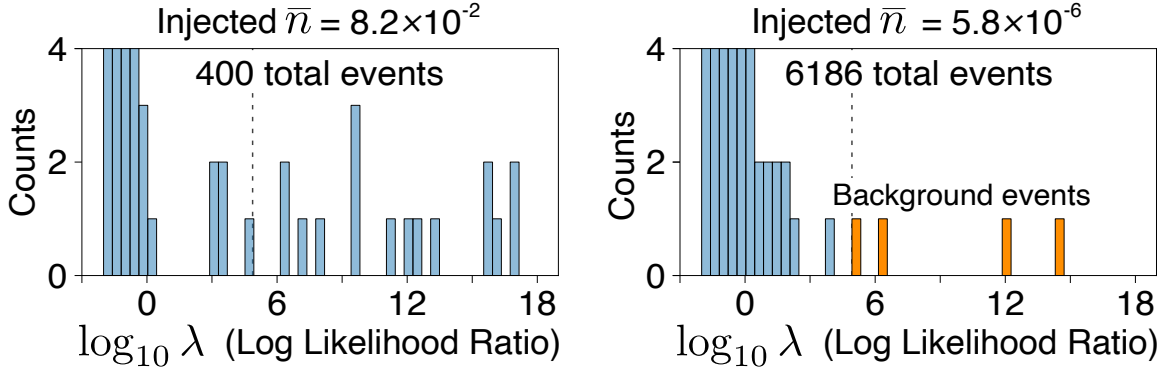
Figure 6.4: **Histograms of events**. I plot a histogram of the log likelihood ratios of all events for two different injected mean photon numbers. The histogram y-axis is cut off at 4 counts to view the rare events at high log likelihood ratios. The dashed grey line corresponds to $\lambda_{\text{thresh}} = 10^5$ used in the experiment and shown in Figure 6.1. The detection of photon events with high likelihood, when very small photon numbers are injected, is from a photon background occupying the storage cavity rather than detector error based false positives.

photons. The likelihood ratios for events where $\bar{n}_{\text{inj}}$ is low are comparable to events when a significant population is injected. This implies the events are highly unlikely to be a result of detector errors and are correctly detected cavity photons.

6.2 Metrological advantage

Counting photons with a superconducting qubit allows us to achieve unprecedented sensitivity to dark matter signals. The technique demonstrated in this work results in single photon detection with background shot noise reduced to $-10 \log_{10} \sqrt{\bar{n}_s} = 15.7 \pm 0.9 \, \text{dB}$ below the standard quantum limit. In Figure 6.5 I compare the metrological gain from counting photons with a qubit to measurements made in trapped ions, Bose-Einstein condensates, and cold atom systems[3]. This shows that qubit based sensing is a viable strategy for quantum sensing generally, particularly for dark matter searches as discussed in Chapter 7.
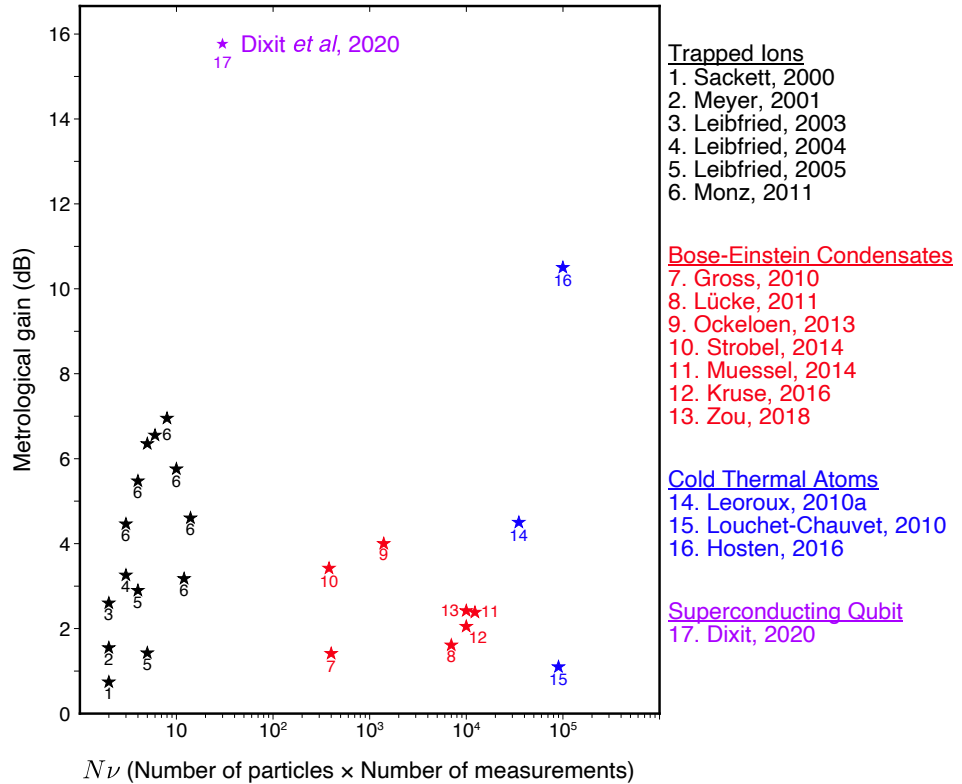
Figure 6.5: **Metrological gain with superconducting qubit**. In this work we show 15.7 dB of metrological gain. Photon counting with a superconducitng qubit is a viable technique for sensing with sub-SQL sensitivity. Figure adapted from Pezz et. al.[3]

6.3 Backgrounds sources and mitigation

With the photon counting technique presented in this work, I am able to decouple detector errors from false positives. This leaves only background photons as the sole source of detector false positives. Further increasing the sensitivity of the photon counter will require identifying and mitigating the background sources.

Though the operating base temperature of the device is 8 mK, the measured background of $\bar{n}_s = 7.3 \pm 2.9 \times 10^{-4}$ corresponds to a photon temperature of 39.9 ± 2.2 mK. This indicates that the device is coupled to extraneous baths.

There are many possible sources of cavity photons that form the measured background. Direct absorption of photons from the environment or indirect excitation due to coupling to

hot subsystems are two avenues for background that I will focus on here.

6.3.1 Direct photon absorption

The photon temperature of the cavity is significantly greater than the operating temperature of the dilution fridge. This points to potential sources of radiation that are able to couple to the cavity mode. These could include the poorly thermalized electronic components, blackbody radiation from higher temperature states, amplifier noise, or insufficiently attenuated microwave lines[1,68].

6.3.2 Quasiparticle induced photons

Due to the coupling between the cavity mode and the qubit, there is a hybridization of the states of the two systems. The dressed eigenstates of the qubit $|\tilde{e}\rangle$ and cavity $|\tilde{1}\rangle$ can be represented as combinations of the uncoupled state $|e\rangle, |1\rangle$ since the interaction is in the dispersive limit.

$$|\tilde{e}\rangle = \sin\theta \, |g, 1\rangle + \cos\theta \, |e, 0\rangle$$
$$|\tilde{1}\rangle = \cos\theta \, |g, 1\rangle - \sin\theta \, |e, 0\rangle$$

(6.2)

If the qubit were purely a two level system, the mixing angle between the qubit and cavity and is determined by their coupling strength g and the detuning Δ as $\sin 2\theta = -\frac{2g}{\sqrt{\Delta^2 + (2g)^2}}$ and $\cos 2\theta = \frac{\Delta}{\sqrt{\Delta^2 + (2g)^2}}$. Combining these two relations yields

$$\frac{\sin 2\theta}{\cos 2\theta} = \frac{2g}{\Delta}$$
$$\tan 2\theta = \frac{2g}{\Delta}$$
$$\theta = \frac{1}{2} \arctan \frac{2g}{\Delta}$$

(6.3)

However, we must account for the fact that the transmon qubits are in fact multilevel systems. This is accomplished numerically and we directly calculate the overlap $|\langle \tilde{1}|e, 0\rangle|^2 = \sin^2\theta = 3.5 \times 10^{-3}$.

Quasiparticle induced excitations of the superconducting qubit are independent of the mixing between the two systems and therefore, excite the qubit in its bare basis. This excitation is described by $|e, 0\rangle = \cos\theta \, |\tilde{e}\rangle - \sin\theta \, |\tilde{1}\rangle$. In this situation there is a nonzero probability that the spurious qubit heating event will manifest as a cavity photon. Therefore, the probability of a cavity photon due to heating is given by the probability of a qubit heating event and the probability that the qubit excitation is projected into a cavity photon, $\bar{n}_s^q = \bar{n}_q \times \sin^2\theta = 1.8 \pm 0.1 \times 10^{-4}$.

Quasiparticle generation

Recent work has shown that quasiparticles are generated in superconducting qubits due to terrestrial and cosmogenic radiation[69–73]. These experiments indicate that radiation produces phonons in the substrate on which the qubits are fabricated. The phonons then couple to the superconducting islands that make up the qubit and produce quasiparticles. The quasiparticles can then tunnel through the insulating barrier. Though the transmon is exponentially insensitive to charge noise, the small amount of remaining dispersion can cause frequency errors as the quasiparticles tunnel. The result is a scrambling of the qubit state which can result in a spurious qubit excitation.

6.3.3   Reducing qubit and cavity populations

Over the course of multiple cooldowns we attempt to reduce the qubit temperature and the residual cavity populations. These efforts include adding filters (reflective and absorptive), potting the entire device in infrared absorbing material, and moving the setup to a fridge with a mixing chamber shield and $8\,\mathrm{mK}$ base temperature. Figure 6.6 describes all the changes made during each cooldown and tracks the qubit temperature and coherences which are a useful proxy for cavity residual population.

I have previously described the measurement protocol to determine the qubit population and temperature in Chapter 5. Here, I infer the readout cavity population by measuring
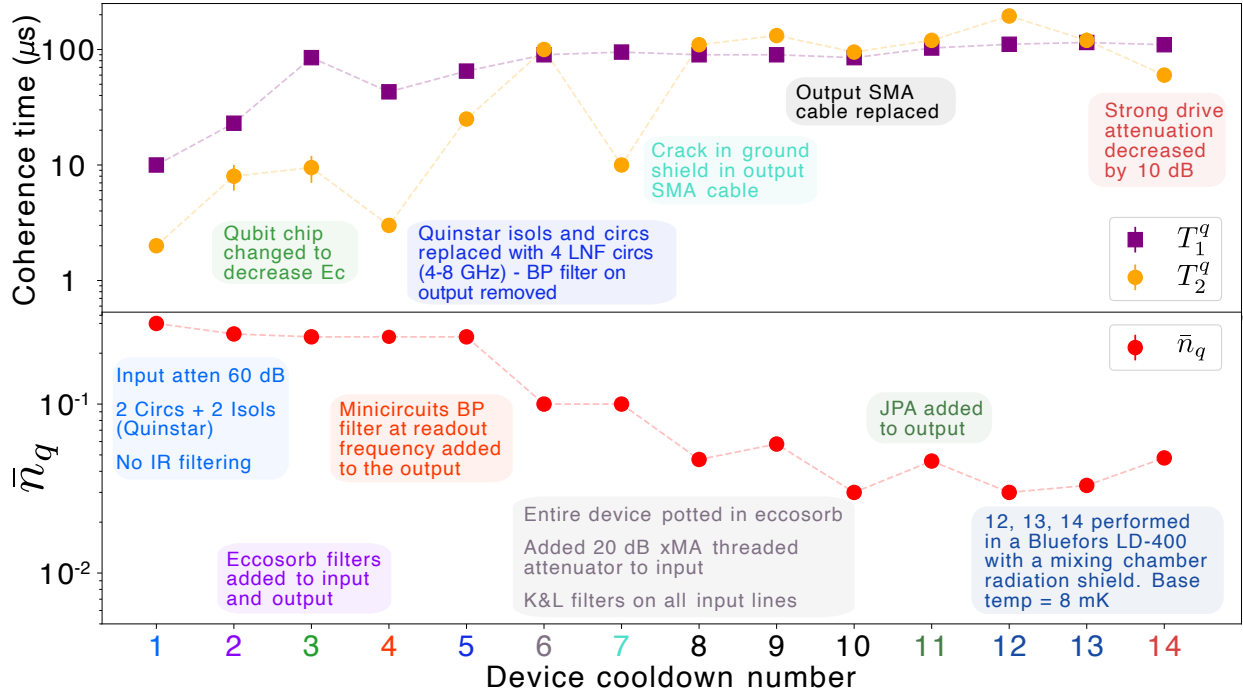
Figure 6.6: **Qubit coherence and temperature**. An enumeration of the efforts over numerous cooldowns and iterations of the device to increase qubit coherences and reduce qubit temperature. The interventions are described and color coded according to the cooldown number. An increased qubit coherence time T_2^q indicates a reduction of the readout cavity thermal population. Filtering, attenuation, and shielding in combination with potting the entire device in eccosorb results in a reduction of the residual qubit occupation.

the qubit dephasing. Since this is a fixed frequency qubit with minimal flux sensitivity, the dominant source of dephasing will be shot noise in the residual readout population. Since the readout lifetime is much shorter than the qubit lifetime, as the readout population fluctuates, the qubit undergoes a series of discrete Stark shifts resulting in dephasing. Though the readout is severely coupled to the environment via the transmission lines, this is a gross overestimate of the population of the storage cavity since we have neglected any other contributions to qubit dephasing. This is intended only for diagnostic purposes and the full photon counting protocol is needed to accurately determine the storage cavity residual population. Residual readout cavity population produces qubit dephasing, leading to increased errors during the photon counting measurement. This is all the more reason to work hard to reduce the residual population of all constituent parts of the device.

64

The qubit dephasing rate can be calculated from the decay and coherence times using Equation 6.4.

$$\Gamma_\phi^q = \frac{1}{T_2^q} - \frac{1}{2T_1^q} \tag{6.4}$$

The measured dephasing rate along with the readout photon number dependent qubit shift $2\chi_r$ and the readout linewidth κ can be used to determine the residual readout population[74], $\bar{n}_r$, using Equation 6.5.

$$\Gamma_\phi^q = \frac{\kappa}{2}\text{Re}\left[\sqrt{\left(1 + i\frac{2\chi_r}{\kappa}\right)^2 + 4i\frac{2\chi_r}{\kappa}\bar{n}_r} - 1\right] \tag{6.5}$$

Figure 6.6 shows that the various strategies employed were successful in reducing qubit and readout excess population. We see an order of magnitude improvement in the qubit population and nearly a two order of magnitude increase in the qubit coherence times over the course of the experiment lifetime. There is, however, no one silver bullet that we are able to find. The suppression of spurious population is the culmination of an intensive, collective, systematic effort.

In addition to further shielding, attenuation, and filtering, an active reset of the qubit and cavity states can be employed to return both systems to the ground state before the dark matter signal is integrated and the photon is counted. The $|f0\rangle - |g1\rangle$ interaction described in Chapter 5 can be used to swap a qubit excitation into the readout cavity where it can be quickly removed from the system through the coupled transmission line. A similar interaction between the storage and readout cavity can be engineered by driving with two tones whose frequencies satisfy the condition $\omega_1 - \omega_2 = \omega_r - \omega_s$. This would allow for a reset of the long lived storage cavity. In Figure 6.7, an excitation in one mode is transferred to another in $\sim 10\,\mu\text{s}$, much quicker than the storage cavity lifetime $T_1^q = 546\,\mu\text{s}$. A reset is enabled when this interaction is applied using the drive frequencies corresponding to the storage and readout cavity. The excitation rapidly exits the over coupled readout cavity into the transmission line $T_1^r = 300\,\text{ns}$.
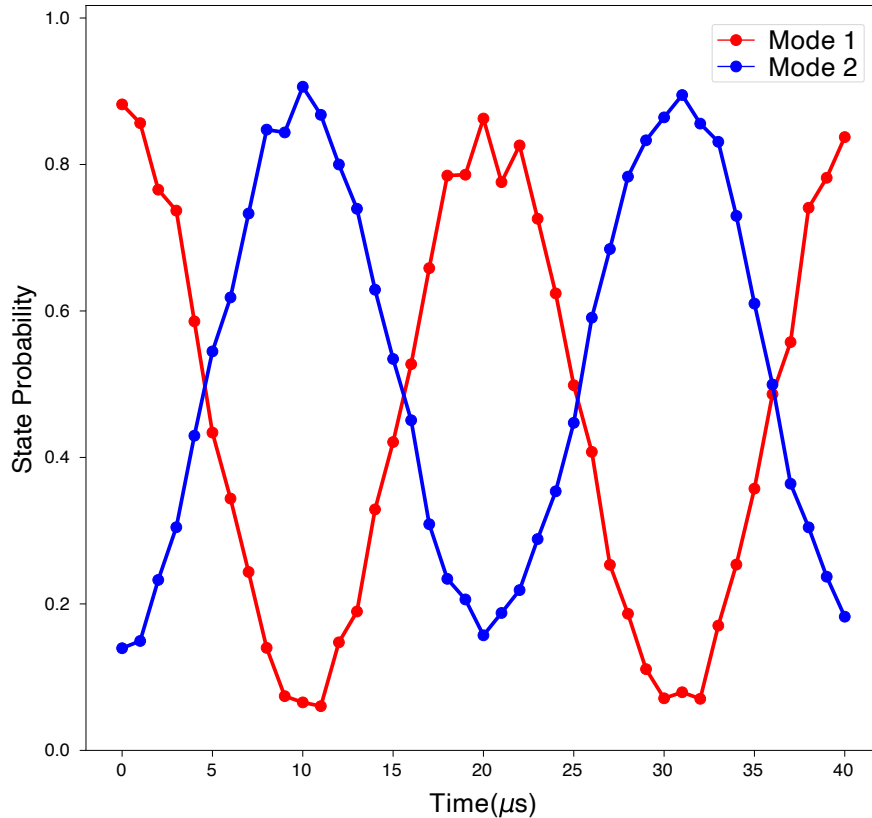
Figure 6.7: **Cavity excitation swap**. A photon from one mode is swapped to another mode of the same cavity. This is achieved by harnessing the interactions of both modes with the non-linear qubit. This procedure can be applied to the storage and readout, both of which are coupled to the same qubit, to facilitate a fast reset of the storage cavity. This would dramatically reduce the cavity background population during the integration of the dark matter signal. Data courtesy of Kevin He.

Further reduction of spurious populations

Further optimizations to the microwave setup of the experiment will yield further suppression of the direct occupation of the storage cavity. These include improved thermalization of the microwave components such as circulators, filters, and μ-metal shielding. Additional layers of shielding from blackbody radiation can be added. A design effort to ensure the cavities and the qubit mount are light tight will be crucial. With these improvements and modifications, I believe we can operate in the regime where direct occupation of the cavity is subdominant to the indirect channel through qubit-cavity coupling.

Unfortunately, it is not possible to turn the qubit-cavity coupling off since this is the

same interaction that is central to the photon counting protocol. There are however many improvements to be made to further reduce the qubit occupation, which lead to a reduced cavity population. Future iterations of these detectors should be equipped with radiation shielding which might include lead shielding around the device as well as a lead castle around the fridge. To further suppress the effect of radiation, the experiment can be performed underground at a facility dedicated to low background physics. Eventually, the experimental equipment can be constructed with radiation free materials dredged from old sunken ships.

On the device side, it is possible to engineer the qubit to be insensitive to quasiparticles generated. This can be accomplished by interspersing normal metal quasiparticle traps in the superconducting material. The traps will absorb a significant fraction of generated quasiparticles and reduce the number that tunnel across the junction. A more speculative idea is to construct the junction from two disparate superconductors, aluminum and niobium for example[54]. In this case quasiparticles will tunnel only in one direction, from the niobium island to the aluminum, but not tunnel back since the superconducting energy difference is asymmetric. This would reduce the probability of qubit heating events.

Finally, active reset of the qubit can temporarily empty the qubit and the entropy can be dumped into the readout cavity. As an example of this in action, we enable the $|f0\rangle - |g1\rangle$ interaction between qubit and readout for $15\,\mu s$ and track the qubit population in Figure 6.8. Even $4\,\mu s$ after the reset, the qubit population is lower by over an order of magnitude than its equilibrium value and reaches $\bar{n}_q^{\text{reset}} = 3.6 \times 10^{-3}$. With this level of suppression, the induced cavity population can be as low as $\bar{n}_q^{\text{reset}} \times (\frac{\sin\theta}{\cos\theta})^2 = 1.3 \times 10^{-5}$. This would result in a metrological advantage of $24\,\text{dB}$ over the SQL.

6.4 Improvements to the protocol

The readout of the qubit state presents an opportunity to further optimize the photon counting protocol. The reconstruction of the cavity state can be achieved with higher likelihood in fewer measurements. and the time per measurement can be significantly reduced with
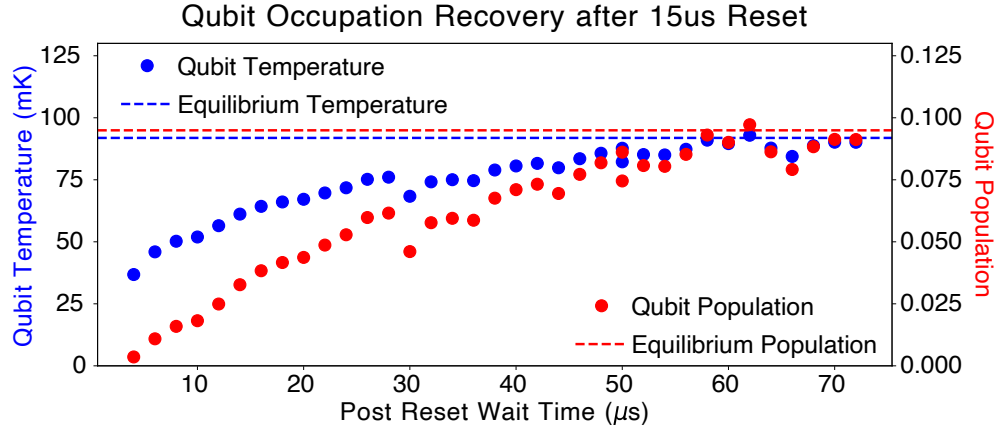
Figure 6.8: **Qubit population reset**. The qubit excitation is swapped into the readout cavity and exits through the transmission line. Here, we track the population and temperature of the qubit a variable time after the reset. The population and temperature equilibrate to their steady state values at long times. These measurements were taken during cooldown 6 as shown in Figure 6.6.

hardware and software improvements.

In the current iteration of the experiment, qubit state readout is performed by applying a square pulse with a 3 µs duration. After interacting with the readout cavity, the signal is amplified with a cryogenic HEMT amplifier with a noise temperature of $\sim 4\,\mathrm{mK}$.

6.4.1   Parametric amplification of readout

In order to overcome the noise imparted by amplification with a cryogenic HEMT, a large pulse containing many photons, integrated over a period much longer than the cavity lifetime is required. With an amplifier adding the minimum noise allowed by the uncertainty principle, both the pulse amplitude and duration can be reduced. This can be achieved by using a quantum limited amplifier.

The experimental setup used in this work already contains a charge pumped Josephson parametric amplifier in line with the readout. Operating the JPA[75] will significantly reduce the effective noise temperature of the output chain. Therefore, the resolution of the readout is greatly improved and the qubit state can be determined with fidelity $> 99\%$. At the readout

frequency of $2\pi \times 8.052\,\mathrm{GHz}$, the noise temperature of a HEMT amplifier corresponds to an equivalent background of $\bar{n}_{\mathrm{HEMT}} \sim 7$. On the timescale of the readout lifetime, we acquire both signal and noise, however over many lifetimes the noise is incoherent and averages out. In order to achieve a required signal to noise ratio of σ_{SNR} requires measuring over many readout lifetimes.

$$\frac{\bar{n}_{\mathrm{meas}}(t/T_1^r)^2}{\sqrt{\bar{n}_{\mathrm{HEMT}}(t/T_1^r)^2}} \geq \sigma_{\mathrm{SNR}}$$

$$t/T_1^r \geq \frac{\sqrt{\bar{n}_{\mathrm{HEMT}}}}{\bar{n}_{\mathrm{meas}}}\sigma_{\mathrm{SNR}}$$

(6.6)

With a measurement probe with $\bar{n}_{\mathrm{meas}} \sim 1$, to achieve $\sigma_{\mathrm{SNR}} \approx 3$, requires a measurement time $t = 10T_1^r$. With a quantum limited amplifier, the effective background is $\bar{n}_{\mathrm{SQL}} = 1$, so the readout will take a factor of $\sqrt{\frac{\bar{n}_{\mathrm{HEMT}}}{\bar{n}_{\mathrm{SQL}}}} \sim 2.5$ less time. By both increasing the drive photon number to 3, and using a quantum limited amplifier we can resolve the readout signal in one cavity lifetime, $T_1^r = 300\,\mathrm{ns}$.

6.4.2 Designing the optimal readout pulse

Currently, the repetition rate of the parity measurements is set by the decay of the photons in the readout cavity. If the parity measurement is performed while the photons from the previous readout are still present, the qubit will dephase and the measurement could result in a false positive. In order to increase the rate of measurements it is necessary to rapidly reset the state of the readout cavity after the measurement is made.

This can be accomplished by shaping the readout pulse optimally to quickly populate and empty the cavity and the timescale of the readout lifetime T_1^r. CLEAR pulses that overshoot the steady state amplitude for injection and undershoot for photon removal have been demonstrated to quickly make high fidelity measurements of the qubit while also minimizing residual photon population at the end of the measurement[76].

Another possible technique to quickly minimize the readout cavity population is to design the pulse with the cavity response in mind[77]. The desired behavior of the readout population
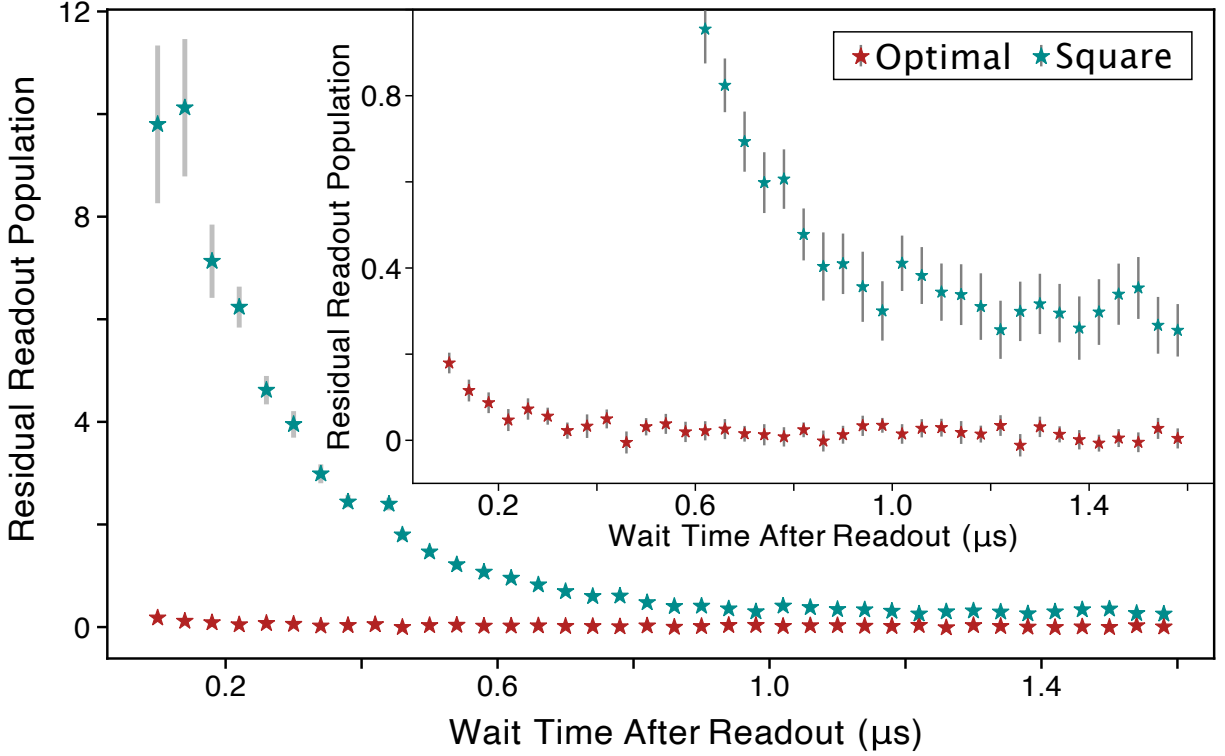
Figure 6.9: **Readout pulse shaping**. We compare the residual readout population for a standard square pulse and the optimized pulse. The readout pulse is used to populate the readout and resolve the state of the qubit. The experiment cadence is set by waiting for this population to empty so as not to produce qubit dephasing in future measurements. By designing an optimal pulse, we can populate and empty the readout cavity, drastically increasing the experiment rate.

is to quickly ring up, persist during measurement, and quickly reset for the next operation. The Fourier transform of this behavior is represented as $O(\omega)$. A pulse input into the cavity, $I(\omega)$ is subject to the Lorentzian response $L(\omega)$ of the resonator, such that the resulting population will have a frequency response $I(\omega)L(\omega)$. To obtain the desired output, $I(\omega)L(\omega) = O(\omega)$, the input pulse can be carefully chosen to cancel the response of the cavity, $I(\omega) = L^{-1}(\omega)O(\omega)$. The only limitation to this technique of designing an optimal readout pulse is the bandwidth of the generator used to make the pulse.

This effort is being led by Morgan Lynn and we have already seen promising results. We have designed an optimized pulse and compared its performance against the standard

square pulse. Both pulses measure the state of the qubit with the same fidelity, but the optimized pulse leaves 100 times fewer photons in the readout cavity after the measurement as seen in Figure 6.9. We can see that it is possible to perform readout on a timescale of $\frac{1}{|2\chi_r|}$ and wait time only set by readout lifetime, which would result in a significant speed up of the experiment. In the original experiment each measurement had a $3\,\mu s$ readout followed by a long wait time to allow the cavity to empty, such that the total time per experiment is $10\,\mu s$. With the optimized pulse we can measure the readout and empty it in a time $\frac{1}{|2\chi_r|} + T_1^r = 2.6\,\mu s + 0.3\,\mu s$. Each parity measurement could be completed in less than $3\,\mu s$.

Chapter 7

Searching for dark matter

The photon detector described in Chapter 6, is ideally suited to perform searches for dark matter. Here, I use the photon counter to conduct a search for hidden photon dark matter. This search excludes a previously unexplored region of the hidden photon parameter space and demonstrates the advantage of quantum sensing with a superconducting qubit. In this chapter I will describe the search protocol, calculate the limits set on hidden photon dark matter, and provide an outline for future dark matter searches with this new technology.

7.1 Search protocol

Unlike the traditional dark matter haloscope searches, a photon counting based experiment cannot perform a continuous search. The process of measuring the cavity state repeatedly with a qubit Zeno suppresses further evolution of the cavity state[78]. This means that while the photon is being counted, the dark matter signal does not accumulate.

As seen in Figure 7.1, the experimental sequence must contain a period of uninterrupted time to integrate the signal and a period to measure the cavity state. The signal integration occurs over one cavity lifetime, $T_1^s = 546\,\mu s$. The photon counting consists of $N = 30$ repeated parity measurements each taking $t_m = 10\,\mu s$, for a total of $300\,\mu s$. This corresponds to a duty cycle of $\frac{T_1^s}{T_1^s + N t_m} = 65\%$. In this work, I perform 15,141 measurements for a total search time of $12.81\,s$ of which $8.33\,s$ is signal integration.

7.2 Expected signal rate

For a dark matter candidate on resonance with the cavity frequency ($m_{\mathrm{DM}}c^2 = \hbar\omega_c$), the rate of photons deposited in the cavity by the coherent build up of electric field in one cavity
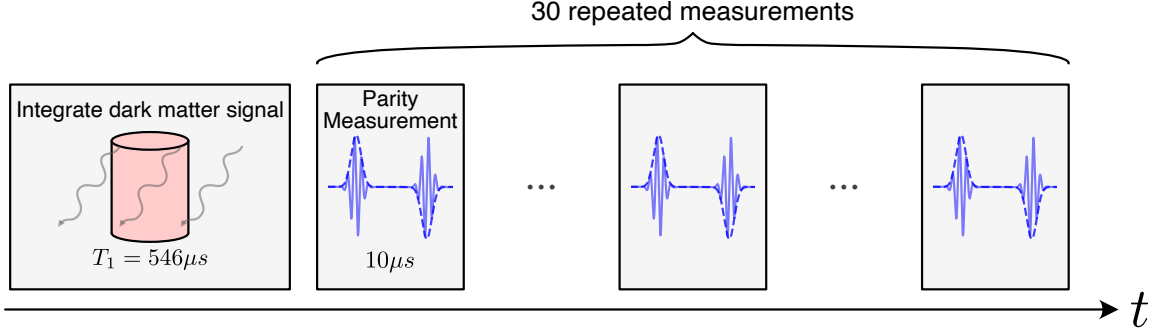
Figure 7.1: **Dark matter search protocol**. Repeated measurements of the cavity state with the qubit Zeno suppress the build up of dark matter induced signal. The experiment protocol, must therefore, be broken up into periods of signal integration and measurement.

coherence time is given by Equation 7.1, where U is the steady state stored energy.

$$\frac{dN_{\text{HP}}}{dt} = \frac{U/\omega_s}{T_1^s} = \frac{1}{2}\frac{E^2 V}{\omega_s}\frac{\omega_s}{Q_s} \tag{7.1}$$

The dark matter sources a current density which induces a electric field response in the cavity oscillating with a frequency equal to the dark matter mass.

$$\begin{aligned}
-\frac{\partial E(t)}{\partial t} &= J_{\text{DM}} \\
-\frac{\partial E e^{imt}}{\partial t} &= J_{\text{DM}} \\
-mE(t) &= J_{\text{DM}} \\
E &= -\frac{J_{\text{DM}}}{m}
\end{aligned} \tag{7.2}$$

The resonant cavity coherently accumulates dark matter induced electric field value over the number of cycles that the dark matter is coherent Q_{DM} times the initial response, $E = -\frac{J_{\text{DM}}}{m}Q_{\text{DM}}$. The expected photon rate is also set by the relative quality factor of the cavity and dark matter $(\frac{Q_s}{Q_{\text{DM}}})$ and the geometric overlap factor between the cavity mode

73

and the dark matter G. Both contributions are discussed below.

$$\frac{dN_{\mathrm{HP}}}{dt} = \frac{1}{2}\frac{E^2 V}{\omega_s}\frac{\omega_s}{Q_s} = \frac{1}{2}\frac{J_{\mathrm{DM}}^2 Q_{\mathrm{DM}}^2}{m^2}\frac{Q_s}{Q_{\mathrm{DM}}}GV\frac{1}{Q_s} \tag{7.3}$$

The storage cavity quality factor is $Q_s = \omega_s T_1^s$ and Q_{DM} is the effective quality factor of the dark matter signal. The volume of the cavity is $0.953 \times 3.48 \times 3.56\,\mathrm{cm}^3 = 11.8\,\mathrm{cm}^3$. G is a dimensionless parameter that represents the geometric overlap between the dark matter signal and the electric field of the cavity.

For hidden photons, dark matter induced current, J_{DM} is determined by the mixing parameter, ϵ, field amplitude, A' and mass, $m_{\gamma'}$. Assuming the hidden photons comprise all of the dark matter in the universe, these are in turn, related to the observed dark matter density, ρ_{DM} as shown in Equation 7.4. The dark matter density is observed to be $\rho_{\mathrm{DM}} = 0.4\,\mathrm{GeV/cm}^3 = 2\pi \times 9.67 \times 10^{13}\,\mathrm{GHz/cm}^3$.

$$J_{\mathrm{HP}}^2 = \epsilon^2 m_{\gamma'}^4 A'^2 = 2\epsilon^2 m_{\gamma'}^2 \rho_{\mathrm{DM}} \tag{7.4}$$

7.2.1   Geometric factor

The overlap factor between the dark matter and the cavity mode is determined using the integral in Equation 7.5.

$$G = \frac{1}{3}\frac{\left|\int dV\, E_z\right|^2}{V \int dV\, |E_z|^2} \tag{7.5}$$

The electric field of the lowest order mode of the rectangular storage cavity coupled to the qubit is given by $\mathbf{E} = \sin(\frac{\pi x}{l})\sin(\frac{\pi y}{w})\mathbf{z}$. The polarization of the hidden photon dark matter $\hat{\mathbf{u}}$ is randomly oriented every dark matter coherence time and results in alignment with the electric field of the cavity only 1/3 of the time. The geometric factor is computed to be $G = \frac{1}{3}\frac{2^6}{\pi^4}$.

7.2.2 Random walk enhancement

In this work, the storage cavity decay (T_1^s) and dephasing (T_2^s) times are much longer than the coherence time of the dark matter with $Q_{\text{DM}} = 10^6$. While the dark matter phase is randomized every coherence time, the storage cavity continues to accumulate. This leads to $\frac{Q_s}{Q_{\text{DM}}}$ incoherent displacements within a single cavity lifetime. This random walk of cavity displacements is on average $\sqrt{\frac{Q_s}{Q_{\text{DM}}}}$ times larger than a single dark matter induced displacement. In Equation 7.3, the field amplitude is squared leading to an photon number enhancements of $\frac{Q_s}{Q_{\text{DM}}}$ in the final photon rate deposited in the storage cavity.

7.2.3 Expected number of signal photons

For a given mixing angle ϵ, to determine the number of expected photons deposited in the storage cavity during the integration time, we first substitute Equation 7.4 into Equation 7.3 and obtain Equation 7.6.

$$\frac{dN_{\text{HP}}}{dt} = \epsilon^2 \rho_{\text{DM}} Q_{\text{DM}} GV \tag{7.6}$$

The photon rate over an integration time of $T_1^s \times N_{\text{meas}} = 8.33\,\text{s}$ yields the expected number of deposited photons (Equation 7.7), with $N_{\text{meas}} = 15{,}141$.

$$N_{\text{HP}} = \frac{dN_{\text{HP}}}{dt} \times T_1^s \times N_{\text{meas}} = \frac{\epsilon^2 \rho_{\text{DM}} Q_{\text{DM}} Q_s GV}{\omega_s} N_{\text{meas}} \tag{7.7}$$

7.3 Excluded hidden photon candidates

With the photon detector developed in this work I make $N_{\text{meas}} = 15{,}141$ measurements of the storage cavity. Each measurement consists of integrating the signal in the storage cavity for its lifetime T_1^s and performing 30 repeated parity measurements with the qubit. The detection threshold is chosen such that detector based errors are well below the measured photon background $\frac{1}{\lambda_{\text{thresh}}+1} < \bar{n}_s$. As shown in Chapter 6, this criteria can be achieved by choosing $\lambda_{\text{thresh}} = 10^5$. At this threshold, I count $N = 9$ photons.

7.3.1 90% confidence limit

I conservatively assume that all the counted photons are from background source rather than the result of dark matter detection. I am forced to compare the hypothetical dark matter signal directly to the background rather than the fluctuations of the background since I do not have the ability to perform background subtraction. Later in this chapter I describe two strategies to measure and subtract the contribution of the background. I can rule out, at the 90% confidence level, the hidden photon dark matter candidates that produce less than the measured $N = 9$ photons with less than 10% probability. This requires accounting for both the statistical and systematic uncertainties inherent to the experiment.

Systematic uncertainties

The probability that a given hidden photon candidate with mixing angle ϵ would produce the observed signal is dependent on the uncertainty in the experimental parameters as enumerated in Table 7.1. The uncertainty in the quantum efficiency is determined from fitting the relation between the measured and injected photon population at a detection threshold of $\lambda_{\text{thresh}} = 10^5$. The storage cavity frequency uncertainty is obtained by Ramsey interferometry. The quality factor of the cavity is given by $Q_s = \omega_s T_1^s$ so the uncertainty is calculated as $\sigma_{Q_s}^2 = (\omega_s \sigma_{T_1^s})^2 + (T_1^s \sigma_{\omega_s})^2$. The volume uncertainty is estimated by assuming machining tolerances of 0.005 inches in each dimension. The form factor uncertainty is estimated from assuming 1% error in the simulated structure. Of the experimental quantities, the efficiency has largest fractional uncertainty (13%), though the statistical fluctuations of the observed counts still dominate (33%).

Marginalizing over nuisance parameters

In each measurement a photon is counted or not so the signal is described by a binomial distribution with probability set by the expected number of deposited photons as calculated

Expt. Parameter	Θ	σ_Θ
Quantum efficiency	$\eta = 0.409$	$\sigma_\eta = 0.055$
Storage cavity frequency	$\omega_s = 6.011\,\text{GHz}$	$\sigma_{\omega_s} = 205\,\text{Hz}$
Storage quality factor	$Q_s = 2.06 \times 10^7$	$\sigma_{Q_s} = 8.69 \times 10^5$
Storage cavity volume	$V = 11.8\,\text{cm}^3$	$\sigma_V = 0.2\,\text{cm}^3$
Storage form factor	$G = 0.22$	$\sigma_G = 0.003$

Table 7.1: **Experimental parameters**. Systematic uncertainties of physical parameters in the experiment must be incorporated in determining the excluded hidden photon mixing angle ϵ.

in Equation 7.7. The systematic uncertainties of the various experimentally determined quantities in Equation 7.7 are treated as nuisance parameters[79] with an assumed Gaussian distribution of mean Θ and standard deviation σ_Θ as shown in Table 7.1. I marginalize over the nuisance parameters[80] and compute the cumulative probability of the hidden photon candidate producing the observed signal, shown in Equation 7.8.

$$
\begin{aligned}
P(\leq N) = \int_0^\infty \prod_i d\Theta_i' \frac{e^{-(\Theta_i - \Theta_i')^2/2\sigma_{\Theta_i}^2}}{\sqrt{2\pi}\sigma_{\Theta_i}} \sum_{k=0}^N \frac{N_{\text{meas}}!}{k!(N_{\text{meas}} - k)!} \\
\times \left(\frac{\eta'\epsilon^2 \rho_{\text{DM}} Q_{\text{DM}} Q_s' G' V'}{\omega_s'} \right)^k \left(1 - \frac{\eta'\epsilon^2 \rho_{\text{DM}} Q_{\text{DM}} Q_s' G' V'}{\omega_s'} \right)^{N_{\text{meas}} - k}
\end{aligned}
\tag{7.8}
$$

For a given hidden photon candidate, a cumulative probability of < 0.1 implies that candidate has less than 10% chance of producing the observed signal, thereby excluding such a candidate with 90% confidence. This leads us to exclude, with 90% confidence, hidden photon candidates with $\epsilon^{90\%} > 1.68 \times 10^{-15}$ as seen in Figure 7.2

This analysis is over constraining since it neglects the limitations of the detector in observing arbitrarily large signals. I describe the reach of the photon counting technique developed to detect, for example, large amplitude or off resonant signals.
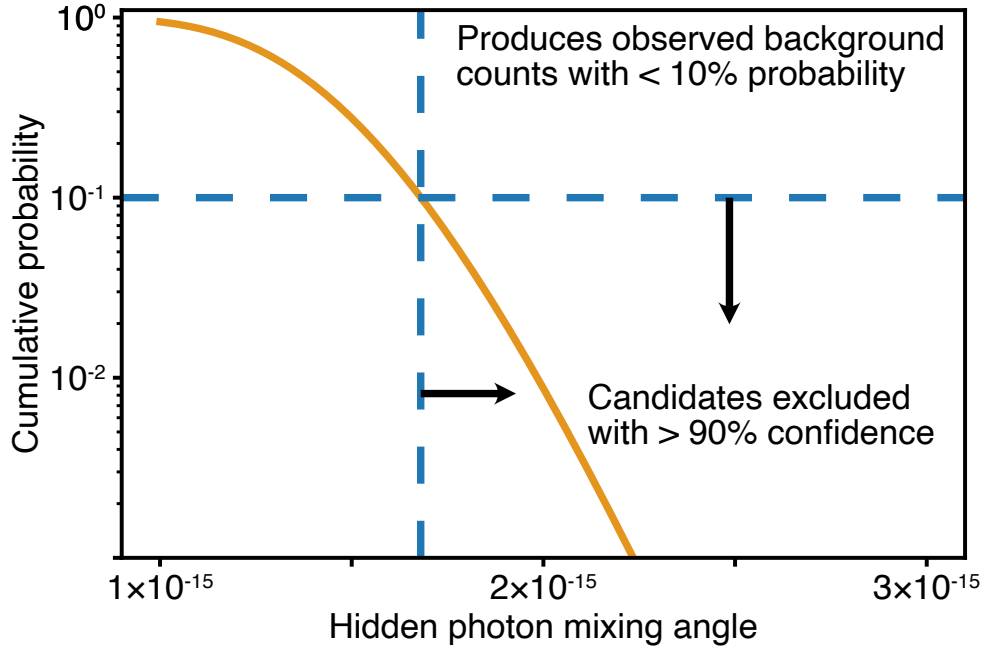
Figure 7.2: **Cumulative probability of hidden photon candidate producing observed signal.** Regions where the cumulative probability falls below 0.1 are ruled out as potential hidden photon candidates with 90% confidence. The minimum mixing angle that can be excluded with 90% confidence is 1.68×10^{-15}.

7.3.2 Resonant signal

The previously calculated exclusions assumed a dark matter signal on resonance with the storage cavity where the detector is most sensitive. A resonant dark matter signal will result in maximal transfer of power into the cavity. Additionally, all the qubit based protocols will function as intended. This allows for the strictest possible exclusion of the hidden photon mixing angle as compared to a signal at any other frequency.

7.3.3 Off resonant signal

In Gambetta et. al.[8], the photon dependent qubit frequency shift is calculated to be $2\chi + \omega_c - \omega_{\gamma'}$ where $\hbar\omega_{\gamma'} = m_{\gamma'}c^2$. When the signal driving the cavity is off resonant, it also

78

dresses the qubit resulting in a modification of the per photon shift. The parity measurement used to determine the photon number relies on precise timing between the two $\pi/2$ pulses set by the nominal 2χ. A photon number dependent shift incommensurate with the nominal shift results in a reduction of the parity measurement efficiency η_{parity} as shown in Equation 7.9.

$$\eta_{\text{parity}} = |\frac{1}{2}(e^{i\pi(2\chi+\omega_c-\omega_{\gamma'})/2\chi} - 1)|^2 = \sin^2\left(\frac{\pi}{2}\frac{2\chi+\omega_c-\omega_{\gamma'}}{2\chi}\right) \tag{7.9}$$

The effect of this inefficiency in each parity measurement is determined by introducing an additional source of error in the hidden Markov model analysis. The data set is then reanalyzed and the detection efficiency is extracted in the presence of this additional error. Figure 7.3 shows both the efficiency of an individual parity measurement and the collective efficiency of 30 repeated measurements of the same photon.

For a very large detuning of the hidden photon signal from the storage cavity, the induced photon number dependent shift is out of the bandwidth of the $\pi/2$ pulses used in the parity measurements. Without the ability to address the qubit, we lose sensitivity to any potential signals that are far off resonance. The pulse shapes are Gaussian with $\sigma = 6\,\text{ns}$. The detector is therefore only sensitive to candidates whose mass obeys the criteria $|2\chi + \omega_c - \omega_{\gamma'}| < \frac{1}{\sigma}$.

7.3.4 Large amplitude signal

In addition to being able to detect single photons in the storage cavity, the photon counting technique employed is also sensitive to any cavity population with an odd number of photons. This is a result of using a parity measurement rather than using a number resolving pulse that specifically targets the one photon state. This provides the benefit of giving the qubit based detection sensitivity to large amplitude signals.

For a given dark matter signal with a certain mass, if the probability of odd photon number population P_{odd} is greater than the excluded $\bar{n}_{\text{HP}}^{90\%}$, the candidate could be detected. The photon population excluded at the 90% confidence level is computed using the excluded
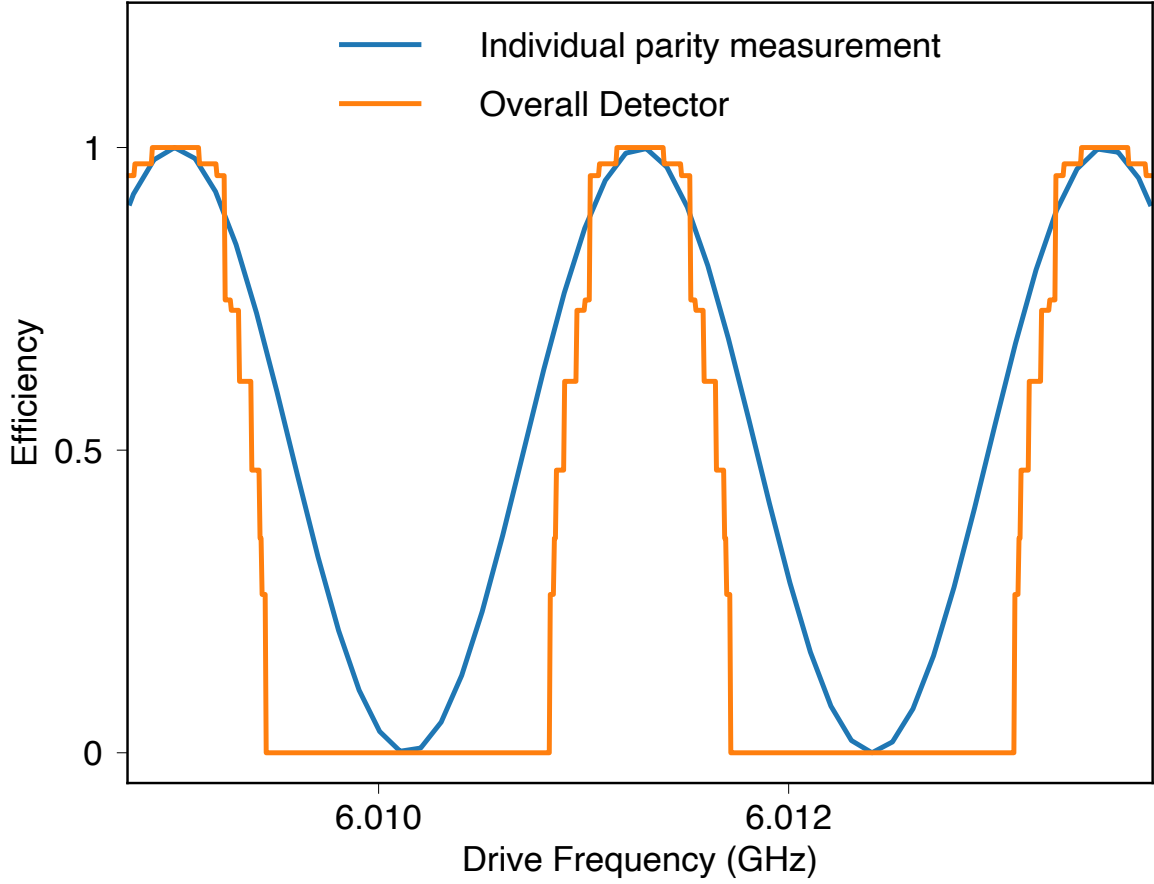
Figure 7.3: **Parity measurement and detector efficiency.** The efficiency of an individual parity measurement (blue) is sinusoidal in the frequency of the hidden photon induced drive $\omega_{\gamma'}$ as calculated in Equation 7.9. The photon counting technique requires a series of 30 repeated parity measurements which collectively operates with an efficiency shown in orange.

mixing angle $\epsilon^{90\%}$ and Eqn. 7.7 as $\bar{n}_{\mathrm{HP}}^{90\%} = \frac{N_{\mathrm{HP}}^{90\%}}{N_{\mathrm{meas}}} = 2.42 \times 10^{-3}$. To determine P_{odd} we follow Gambetta et. al.[8] and obtain Equation 7.10.

$$P_{\mathrm{odd}} = \frac{1}{\pi} \sum_{k=0}^{\infty} \mathrm{Re} \left(\frac{\frac{1}{(2k+1)!}(-A)^{2k+1}e^A}{2(2\pi/T_2^q + \Gamma_m) + (2k+1)2\pi/T_1^s} \right) \tag{7.10}$$

$$A = D \frac{\pi/T_1^s - i\chi - i(\omega_c - \omega_{\gamma'})}{\pi/T_1^s + i\chi + i(\omega_c - \omega_{\gamma'})} \tag{7.11}$$

$$\Gamma_m = D \frac{\pi}{T_1^s} \tag{7.12}$$

The distinguishability is shown in Equation 7.13.

$$D = \frac{2(n_- + n_+)\chi^2}{(\pi/T_1^s)^2 + \chi^2 + (\omega_c - \omega_{\gamma'})^2} \tag{7.13}$$

n_- and n_+ are related to the drive strength (n_{HP}) in units of photons as shown in Equation 7.14.

$$n_\pm = \frac{n_{\mathrm{HP}}(\pi/T_1^s)^2}{(\pi/T_1^s)^2 + (\omega_c - \omega_{\gamma'} \pm \chi)^2} \tag{7.14}$$

For very large amplitude signals, the cumulative photon number shift of the qubit frequency will be outside the addressable band of the parity measurement. The pulses are Gaussian with $\sigma = 6\,\mathrm{ns}$. This sets the criteria for sensitivity to large amplitude signals: $\bar{n}_{\mathrm{HP}} < \frac{1}{|2\chi + \omega_c - \omega_{\gamma'}|\sigma}$.

7.3.5 Dark matter lineshape

The previous analysis assumes that the dark matter signal is infinitely narrow band. However, we know that there is a broadening of the dark matter line due to its velocity dispersion. This leads to a signal with quality factor of $Q_{\mathrm{DM}} \sim 10^6$. To include the dark matter lineshape information into the region of detectable signal, we convolve the signal shape with excluded region which assumed a narrow line[81]. This procedure accounts for dark matter candidates that may be slightly off resonance from the regions of detectable signals, but have frequency content from broadening within the detection region.

Including all of the constraints imposed by the detector and technique, Figure 7.4 shows all the possible hidden photon candidate induced mean photon populations that are excluded by the photon counting experiment.
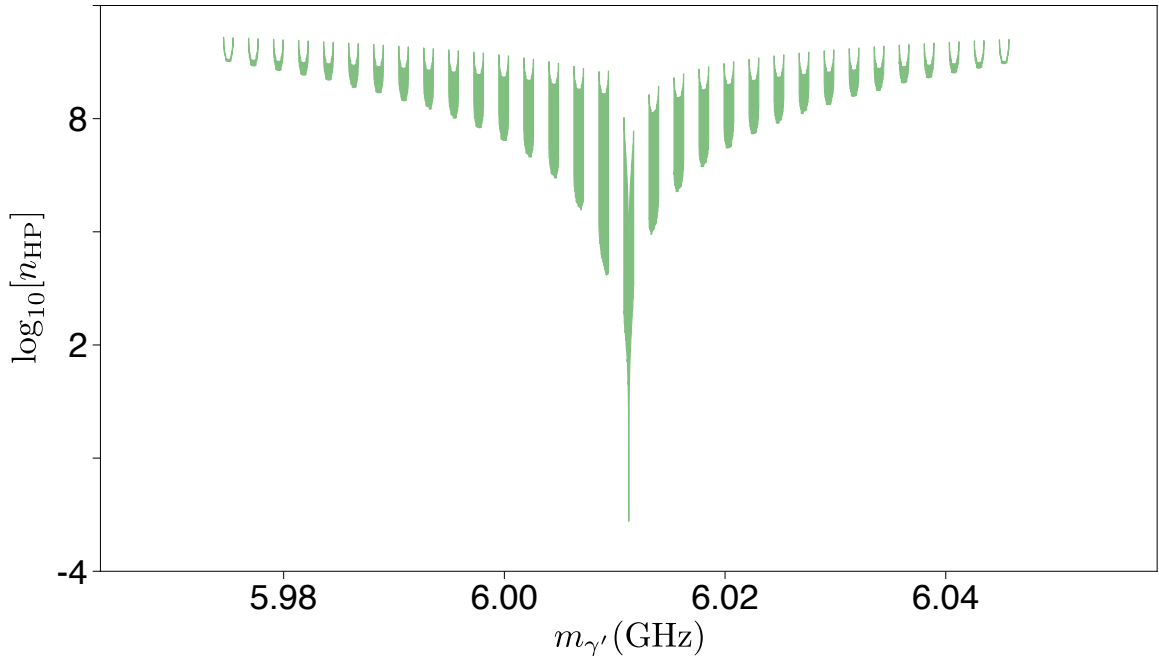
Figure 7.4: **Excluded n_{HP} as a function of $\omega_{\gamma'}$.** The shaded regions indicates n_{HP} that would result in $P_{\text{odd}} \geq \bar{n}_{\text{HP}}^{90\%}$ and are detectable with the photon counting technique. Since these candidates are inconsistent with the observation, they are excluded.

7.4 Excluded kinetic mixing angle

To determine the limits on the mixing angle, I incorporate all the detector constraints shown in Figure 7.4. Using Equation 7.7 I obtain the constraints across mass and amplitude on the mixing angle set by the photon counting experiment as shown in Figure 7.5

We exclude a previously unexplored region of hidden photon parameter space with unprecedented sensitivity. The photon counting strategy developed in this work provides a path to searching for previously inaccessible axion and hidden photon candidates.

7.5 Future dark matter searches

The sub-SQL metrology demonstrated in this work can significantly increase the reach of future dark matter experiments. For both axion and hidden photon searches the photon
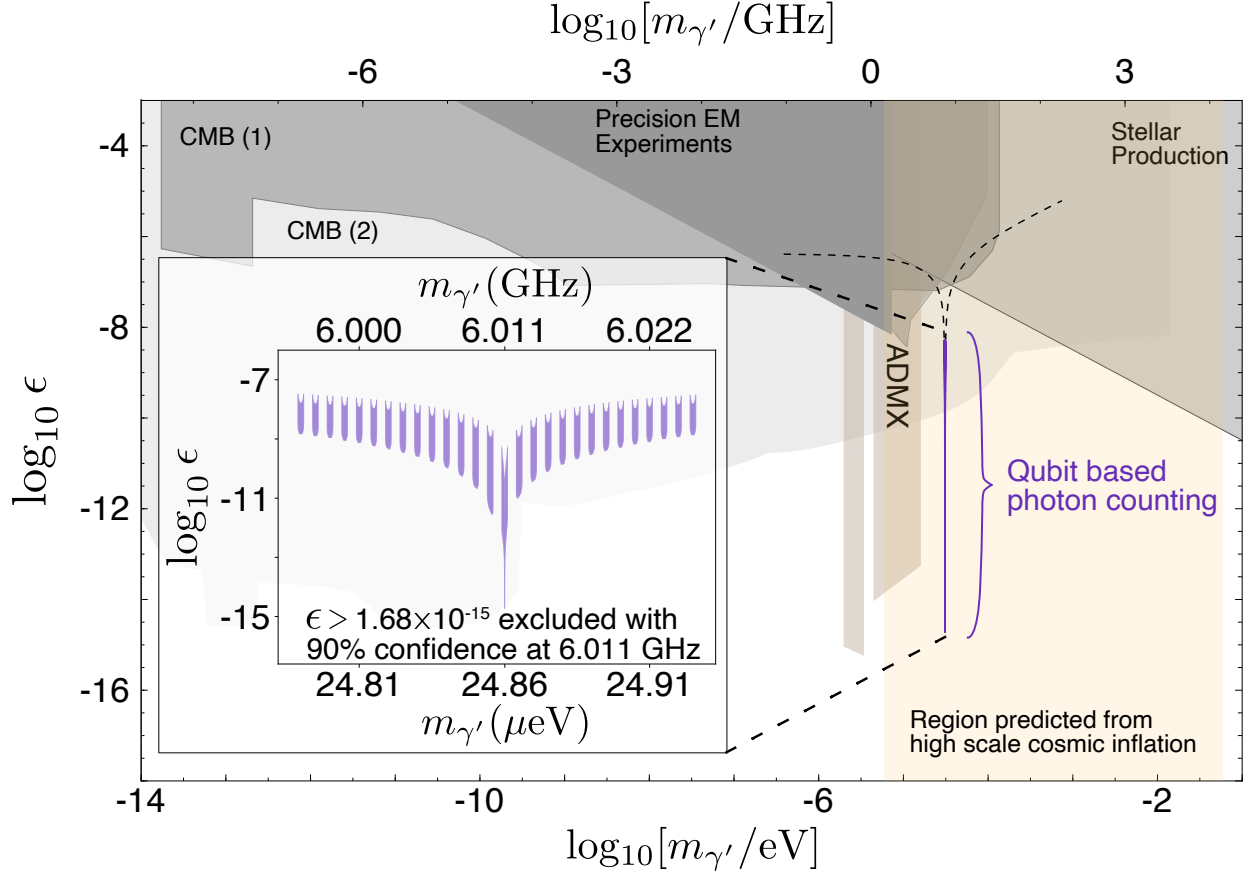
Figure 7.5: **Hidden photon dark matter parameter space**. Shaded regions in the hidden photon parameter space[4,5] of coupling (ϵ) and mass (m_γ) are excluded. In the orange band, hidden photon dark matter is naturally produced in models of high scale cosmic inflation[6]. The exclusion set with the qubit based photon counting search presented in this work[7], is shown in purple (dashed black line to guide the eye). On resonance with the storage cavity ($m_{\gamma'}c^2 = \hbar\omega_s$), the hidden photon kinetic mixing angle is constrained to $\epsilon \leq 1.68 \times 10^{-15}$ with 90% confidence. The Ramsey measurement procedure is also sensitive to signals that produce cavity states with odd photon number populations greater than the measured background. Sensitivity to off resonant candidates gives rise to bands of exclusion (see inset) centered around regions where the photon number dependent qubit frequency shift[8] is an odd multiple of 2χ. Sensitivity to large amplitude and highly detuned signals is limited by the bandwidth of the $\pi/2$ pulses used in the parity measurements.

counting technique must be compatible with a tuning element so that a range of dark matter masses can be probed. For an axion search, the device also needs to be compatible with the high magnetic field required to facilitate the conversion of axions to photons.

7.5.1 Search speed up

With the significantly reduced noise floor, future dark matter searches can search for small signals in much less time. The required signal integration time t_{int} is determined by the signal rate, $R_s = \bar{n}_{\text{DM}}/T_1^s$, and the background rate, $R_b = \bar{n}_b/T_1^s$ in the limit that detector errors are sufficiently suppressed. Equation 7.15 describes the criteria for a successful detection of a signal at a level, σ above the shot noise of the background.

$$R_s t_{\text{int}} > \sigma \sqrt{R_b t_{\text{int}}} \tag{7.15}$$

The integration time needed for a given signal and the background is given in Equation 7.16. A reduction of the cavity background population linearly reduces the integration time needed to have sensitivity to a given signal.

$$t > \sigma T_1^s \frac{\bar{n}_b}{\bar{n}_{\text{DM}}^2} \tag{7.16}$$

As compared to the effective background of a quantum limited amplifier, $\bar{n}_{\text{SQL}} = 1$, the background population achieved in this work, $\bar{n}_b = 7.3 \times 10^{-4}$ would result in a speed up of the search by a factor of $\bar{n}_{\text{SQL}}/\bar{n}_b = 1370$. This three order of magnitude reduction in the integration time would drastically increase the coverage of the dark matter parameter space as the search at each mass would require significantly less time. A scanning search projected to take two years with a linear quantum limited amplifier, would be completed in 12 hours.

The speed up of the search is even more drastic when compared to actual backgrounds achieved with linear amplification. In previous axion searches[37,39], the effective background has ranged from $\bar{n}_b = 2 - 10 \times \bar{n}_{\text{SQL}}$. The background attenuation demonstrated in this work constitutes a speed up of between a factor of 2,500 to 13,000 relative to currently operating dark matter searches.

7.5.2 Future axion search

Recall that for an axion search a microwave cavity must be bathed in a magnetic field in order to enable the axion to photon conversion. The signal power scales with square of the magnetic field and so it is beneficial to operate with extremely large magnetic fields. This, however, is incompatible with the superconducting cavities and qubit that compose the photon counter. There are many ongoing efforts build cavities that can be operated in magnetic fields and we can borrow quantum information techniques to couple the photon counting device with the cavity in the field.
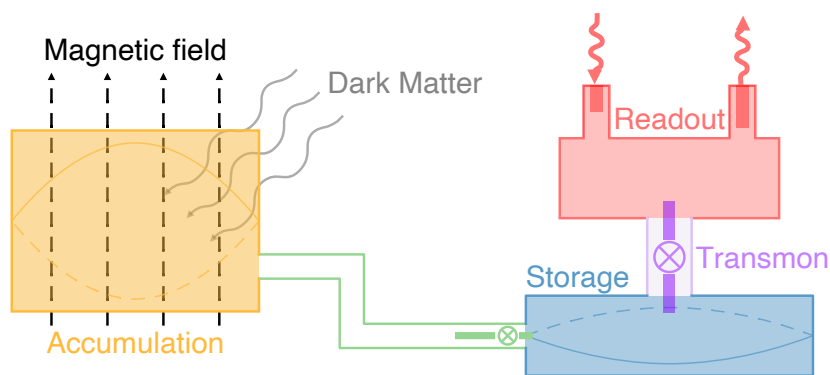
Figure 7.6: **Future axion search**. A high Q cavity (orange) in a magnetic field (black) accumulates the dark matter (gray) induced photon. This signal is then transferred to the storage cavity (blue) using a non linear element (green) such as a Josephson parametric converter. This allows all superconducting elements to be housed in magnetic shielding far from the high field region surrounding the accumulation cavity. The transfer is enabled by driving the non linear elements at the difference frequency between the two target cavity modes. The photon is then counted using the transmon qubit (purple) which is read out with an additional cavity (red).

High Q accumulation cavity

The structure of a future axion search will involve an accumulation cavity, shown in Figure 7.6, whose purpose is to capture the converted photon by occupying the magnetic field region. A superconducting cavity will not fare well in the high magnetic fields required. It is, therefore, important to construct high Q cavities that are not made of superconducting

material but perform better than a standard copper cavity.

The most promising ideas involve constructing a photonic crystal out of low loss dielectric material[82]. This crystal structure results in a band gap that disallows photons of certain wavelengths from penetrating or leaving. By generating a defect of the right size, we can induce a single mode inside the band gap. Once populated, the photon in the mode is confined by the crystal structure, with losses limited by the dielectric material. Our efforts to construct band gap cavities, led by Ankur Agrawal, have already shown better quality factors than copper cavities. With further optimizations and using ultra low sapphire as the dielectric, a quality factor of $Q \sim 10 \times 10^6$ can be achieved.

Transferring population

The photon counting device, consisting of the storage cavity, qubit, and readout cavity, will be placed in a field free region. This can be accomplished by physically separating it from the magnet, surrounding with a counter wound bucking coil to cancel residual field, and enclosing it in multiple layers of magnetic shielding.

The challenge then becomes how to transfer the accumulated signal to the storage cavity to be counted. This mechanism must also work for all frequencies in the tuning range of the accumulation cavity. This sort of state swap interaction can be performed by introducing a non-linear element, shown in Figure 7.6. A Josephson parametric converter can be used to couple the accumulation and storage cavity, enabling a 4-wave mixing process[83–85]. The accumulation and storage cavities account for two of those fields, and we must supply the other two by pumping the device. By applying a drive at frequency $(\omega_a - \omega_s)/2$ we supply two photons whose energies matches the difference energy between the two cavities. The strength of the drive, the coupling between cavities and converter, and non-linearity of the converter all determine the transfer rate.

In the case of a passive transfer by connecting accumulation and storage with only a transmission line and no non-linear element, the two cavities must be tuned to be on reso-

nance with each other. With a non-linear transfer induced by the parametric converter, the storage cavity can remain fixed in frequency while the accumulation cavity is tuned to search for different axion masses. Now, only the frequency of the pump will need to be tuned to ensure the transfer is on resonance by satisfying the condition $\omega_p = (\omega_a - \omega_s)/2$. This greatly reduces the complexity of the entire system. Only one cavity needs to be mechanically tuned and the cavities do not need to be locked together using feedback.

7.5.3 Future hidden photon search

No magnetic field is required to search for the hidden photon. This simplifies the experiment significantly. The accumulation and storage mode can be the same cavity as is the case for the device used in this work. To search across a range of masses, the accumulation/storage cavity must be tuned. Though its frequency is changing, the fundamental quantum non-demolition interaction with the qubit remains. The experimental protocol remains the same at each tuning provided the dispersive shift is sufficiently large enough to resolve individual photons and the qubit is far detuned.

There is no constraint on the material of the cavity. We are free to use very high quality superconducting cavities which can have $Q > 10^{10}$. Though the cavity quality factor is higher than the dark matter broadening of $Q = 10^6$, we only need to sample the dark matter once or twice per linewidth. This means that with only 10^6 tunings, an entire octave in frequency can be covered.

Cavity tuning with a Josephson junction

One viable path for tuning the cavity is the standard technique of moving a metal or dielectric rod within the volume of the cavity. We are currently exploring a Josephson junction based mechanism that can tune the cavity by $\mathcal{O}(100\,\mathrm{MHz})$. This relies on the ability to tune the inductance of the circuit by threading a magnetic flux through a junction loop. We can tune this structure into resonance with the cavity to achieve a large splitting.

The potential drawbacks to this approach are a reduction in the geometric overlap of the mode of interest and the dark matter field. This is due to the complete hybridization of the tuner and cavity when they are on resonance. Half of the resulting mode is now contained in the tuner which has no coupling to the dark matter. However, a factor of 2 reduction in the form factor is acceptable in return for the tuning capability.

The extent of the tuning range depends on the bare coupling g between the tuner and cavity. When on resonance the two resulting modes (the symmetric and anti-symmetric combinations of the bare modes) are split in frequency by $2g$, or equivalently repelling the mode of interest by g. In preliminary studies, we have found that by varying the tuner inductance, we can achieve an avoided crossing between the storage and tuner modes with a splitting of almost $2g \sim 500\,\text{MHz}$. A more realistic experiment might have a tuning range closer to $100\,\text{MHz}$ and a collection of similar structures slightly detuned from each other could be simultaneously operated to cover a large mass range.

Background calibration

Unlike the axion search, the hidden photon signal cannot be tuned off by varying the applied magnetic field. This makes it challenging to discriminate between signal and background. The typical strategy is to measure the background in the cavity when tuned to frequencies separated by more than one dark matter linewidth from the frequency of interest. This estimates the background and allows us to subtract the residual population from the measured signal.

Another possibility is to use a second calibration cavity alongside the search cavity. Both cavities are operated in identical cryogenic and microwave environments as well as being coupled to a qubit for photon counting. We can design the qubit to couple to a mode of the calibration cavity that has a negligible overlap with the dark matter field (Equation 7.5) and is at the same frequency as the search cavity. The geometry of this auxiliary cavity can be arranged to preclude the possibility of the dark matter induced photon, ensuring that the

measured population is solely due to backgrounds. One possible example of a pair of modes could be to use the fundamental transverse magnetic mode of the right cylindrical cavity (TM_{010}) as the search mode and the first longitudinal harmonic (TM_{011}) in a second cavity as the calibration mode. The harmonic has an electric field profile with one node along the longitudinal direction resulting in no overlap with the dark matter field $(G = 0)$.

7.5.4 Stimulated emission

In addition to using the non linearity of the qubit to count photons we can use it to enhance the probability of the dark matter depositing a photon in the cavity. By initializing the cavity in a highly non classical state we can stimulate the emission of a photon by the dark matter[86]. Take for example preparing the cavity in Fock state $|n\rangle$. The dark matter is effectively a very weak displacement of the cavity $\mathcal{D}(\alpha) = e^{\alpha a^\dagger - a^* a}$. In the limit of a small dark matter induced displacement $(\alpha \ll 1)$, the probability of finding the cavity is state $|n+1\rangle$ is shown in Equation 7.17.

$$
\begin{aligned}
P(n+1) &= |\langle n+1| \, \mathcal{D}(\alpha) \, |n\rangle \, |^2 \\
&= |\langle n+1| \, e^{\alpha a^\dagger - \alpha^* a} \, |n\rangle \, |^2 \\
&\approx |\langle n+1| \, \alpha a^\dagger - \alpha^* a \, |n\rangle \, |^2 \\
&= |\langle n+1| \, \alpha a^\dagger \, |n\rangle \, |^2 \\
&= |\alpha \, \langle n+1| \, \sqrt{n+1} \, |n+1\rangle \, |^2 \\
&= (n+1)\alpha^2
\end{aligned}
\tag{7.17}
$$

Relative to starting with the cavity in the ground state, the initialized cavity has n-fold larger probability of containing an extra photon. The limit to how large a Fock state can be prepared in the cavity is set by the relative quality factors of the cavity and the dark matter as shown in Equation 7.18

$$
n < \frac{Q_c}{Q_{\mathrm{DM}}}
\tag{7.18}
$$

89

There has been some initial progress on this technique, led by Ankur Agrawal. The technology borrowed from quantum information science has already allowed us to significantly reduce the noise associated with our measurement and can potentially also enhance the signal. Superconducting qubits provide the path to an improvement in both components of the signal to noise ratio of searches for low mass dark matter.

7.5.5 Combing through the dark matter parameter space

Though I use only a single mode of a cavity to perform a dark matter search, the 3D structure contains an infinite set of discrete modes. The qubit can couple to all of these modes as long as there is appreciable electric field pointing in the same direction as the qubit dipole. For any mode where the photon induced qubit transition frequency shift is resolvable $(2\chi >> 1/T_2^q)$, a photon counting procedure can used to measure the state of the mode. As long as the mode of interest has a non zero overlap factor, this will result in a comb of simultaneous searches for dark matter candidates. A future dark matter search could harness this ability by using a cavity with engineered mode spacing and optimized mode-qubit couplings[87]. Multimodal cavities, when coupled to a qubit, inherently provide the possibility of realizing simultaneous dark matter searches over a wide range of parameter space.

7.5.6 Low field axion search

There is some evidence that superconducting materials are operable in parallel magnetic fields below $1\,T$. This may present an opportunity to conduct an axion search by placing a qubit and cavity in the magnetic field. This would eliminate the need to transfer the population out of the high field region and the protocols would remain identical to those presented in this work. Here I calculate the integration time needed at each tuning for such a search with reasonable parameters.

Signal rate

Assuming we can operate qubits and superconducting cavities in a $1\,\mathrm{T}$ field, I calculate the integration time required to detect a DFSZ axion. I assume we will be able to initialize the cavity in a Fock state with $N = 10$ photons to stimulate emission of the dark matter signal. This will require an accumulation cavity with $Q_a > 10 \times 10^6$, which can easily be achieved by constructing the cavity out of niobium. We will employ the photon counting technique with backgrounds set by the accumulation cavity residual population, which I estimate to be $\bar{n}_a = 10^{-4}$.

We will use a superconducting cavity with quality factor at $\omega_a = 2\pi \times 6\,\mathrm{GHz}$. The expected signal rate for a DFSZ axion is shown in Equation 7.19.

$$R_s = 0.24\,\mathrm{Hz} \times \left(\frac{V}{11.8\,\mathrm{cm}^3}\right) \left(\frac{B}{1\,\mathrm{T}}\right)^2 \left(\frac{C}{0.66}\right) \left(\frac{g_\gamma}{0.97}\right)^2 \left(\frac{\rho_{\mathrm{DM}}}{0.4\,\mathrm{GeV/cm}^3}\right) \left(\frac{Q_{\mathrm{DM}}}{10^6}\right) \left(\frac{N}{10}\right)$$

(7.19)

The enhancement factor is $N = \frac{Q_a}{Q_{\mathrm{DM}}}$ and the form factor is calculated to be $C = 0.66$ assuming a rectangular cavity.

Background rate

The residual cavity population sets the background rate as calculated in Equation 7.20. Note, the stimulated emission process that enhances the signal rate also enhances the background rate.

$$R_b = N\bar{n}_a \frac{\omega_a}{Q_{\mathrm{DM}}} = 37.7\,\mathrm{Hz} \tag{7.20}$$

Integration time

To detect a signal, we need the signal to noise ratio to be greater than 1. The noise is set by the variance of the background. The integration time required to achieve an SNR of 1 is calculated in Equation 7.22

$$\frac{R_s t}{\sqrt{R_b t}} > 1 \tag{7.21}$$

$$t > \frac{R_b}{R_s^2} = 10.6 \, \text{min} \tag{7.22}$$

7.5.7 High field search

Here I calculate the integration time required per tuning for a search with disjoint accumulation and storage cavity. The population will be swapped before being counted using the technique developed in this work. In this scenario, I assume the accumulation cavity will be implemented as a defect inside a photonic bandgap crystal with $Q_a = 10^6$. I assume we use a frequency converting element to swap the accumulated signal to the storage cavity for interrogation. This process will be imperfect and I assume the efficiency of the transfer to be $\eta_{\text{swap}} = 0.1$. Here the applied magnetic field can be extremely large since the superconducting elements are protected in a remote field free region.

Signal rate

We will use a bandgap cavity at $\omega_a = 2\pi \times 6 \, \text{GHz}$. The magnetic field will be $15 \, \text{T}$. The expected signal rate for a DFSZ axion is shown in Equation 7.23.

$$R_s = 5.46 \, \text{Hz} \times \left(\frac{V}{11.8 \, \text{cm}^3} \right) \left(\frac{B}{15 \, \text{T}} \right)^2 \left(\frac{C}{0.66} \right) \left(\frac{g_\gamma}{0.97} \right)^2 \left(\frac{\rho_{\text{DM}}}{0.4 \, \text{GeV/cm}^3} \right) \left(\frac{Q_{\text{DM}}}{10^6} \right) \tag{7.23}$$

With form factor $C = 0.66$ calculated assuming a rectangular cavity.

Background rate

The residual cavity population sets the background rate as calculated in Equation 7.24.

$$R_b = \bar{n}_a \frac{\omega_a}{Q_{\text{DM}}} = 3.77 \, \text{Hz} \tag{7.24}$$

Integration time

To detect a signal, we need the signal to noise ratio to be greater than 1. The noise is set by the variance of the background. The integration time required to achieve an SNR of 1 is calculated in Equation 7.26. I include the efficiency of the population transfer.

$$\eta_{\text{swap}} \frac{R_s t}{\sqrt{R_b t}} > 1 \tag{7.25}$$

$$t > \frac{R_b}{(\eta_{\text{swap}} R_s)^2} = 12.7 \, \text{s} \tag{7.26}$$

It may seem straightforward to operate an axion search with reduced magnetic field in order to operate a qubit directly inside the accumulation cavity, but there are still many challenges to overcome. The background population is too high and the cavity quality factor is too low to compensate for the diminishing signal from the reduced magnetic field. To tune through an octave in axion mass with the parameters described above, it would require over 20 years of integration.

Though operating a remote counting device requires additional effort to engineering a population transfer, this enables us to operate at significantly higher magnetic fields. I have chosen a pessimistic transfer efficiency for the above calculation. A search over an octave of axion mass would require ~ 150 days. Optimistically, with a low loss cable connecting the nonlinear device to the accumulation cavity, the swap efficiency could be as high at 0.9. The search would then reach DFSZ sensitivity with $\sim 100 \, \text{ms}$ integration time per tuning. A search over an octave of axion mass would require only 2 days of integration. This is the optimal path forward and every effort should be made to enable high efficiency photon transport.

Chapter 8

Conclusion

This work is an example of an instance when two nominally unrelated fields converge, resulting in advances in both fields. At first glance quantum information science and particle astrophysics are seemingly unrelated. It is exactly these unexpected connections that lead to progress and advancement.

The fields of quantum information and quantum metrology are burgeoning, with the sensors and techniques developed here playing an important role. As cryogenic microwave systems become ubiquitous, it is paramount to understand the ambient temperature and characterize backgrounds that manifest as errors in quantum circuits. For example, a qubit can be used as a primary thermometer to assess the population of a series of microwave modes being used as a quantum random access memory[87,88]. Recent developments have demonstrated the compatibility of superconducting qubits with quantum acoustical systems and there is progress in interfacing qubits with Rydberg atoms. The error mitigation capabilities we have demonstrated will enable such hybrid experiments with superconducting qubits serving as a central hub for information processes and characterization. The advances demonstrated in this work have applications in performing metrology in a wide range of fields. The unprecedented control over design, properties, and operation of superconducting qubit technology make it a versatile tool that could be deployed in novel scenarios.

The advent of superconducting amplifiers has brought us close to the quantum limit, but for dark matter searches in the GHz range, even the quantum limit overwhelms the anticipated signal. Development and deployment of photon counting sensors is imperative to search for such dark matter candidates. This technique allows us to bend the quantum limit, extract all the information we need to, and in principle, conduct a background free search. Qubit based counting experiments are the next step in the search for dark matter. We demonstrate a counting protocol that is over 1,000 times more sensitive to dark matter

than the conventional strategies.

The future of searches for low mass bosonic dark matter candidates is intricately tied with the techniques and technologies of quantum computing. In the GHz range, superconducting qubits can be used to count signal photons and also enhance the dark matter induced signal. These advancements all rely on the nature of the interaction between a qubit and photon. The quantum non-demolition aspect enables the repeated measurements needed to successfully mitigate errors. The non-linearites of the qubit enable signal enhancement by stimulated emission. These strategies, though implemented with superconducting qubits, can be translated to other technologies such as atoms, spins, or mechanics. This will further push our ability to devise experiments sensitive enough to search for a wide range of dark matter candidates.

Though the nature of dark matter remains a mystery, we have added one element to the vast array of tools used by scientists to understand it. It is exhilarating to be part of this effort to collectively tackle such universal challenges. A bonus of these lofty undertakings is a treasure trove of new ideas and technologies that may play vital roles in yet undiscovered challenges. I am proud of all that we have accomplished and I am privileged to be one small part of the collective scientific endeavor. I hope this work can provide some inspiration and I am excited for all of your new ideas and discoveries.

Appendix A

Quantum limit for linear amplification

In Chapter 2, I show that the potential dark matter induced signal is significantly smaller than the noise added by a linear amplifier operating at the quantum limit. The solution is to devise a readout scheme that selectively measures only one quadrature of the field, while discarding the information in the other. In this Appendix I derive the result that the noise added by a linear amplifier operating at the quantum limit is the equivalent of one quanta[2,46].

The input field has quadrature amplitudes x_i, p_i and the output field is denoted by x_o, p_o. The amplifier acts on both quadrature equally and the gain is given by G. Both the input and output fields obey the commutation relation $[x_i, p_i] = [x_o, p_o] = \frac{i\hbar}{2}$. The uncertainty relation for the input and output fields is given by:

$$\sigma_{x_i}\sigma_{p_i} = \sigma_{x_o}\sigma_{p_o} = \frac{1}{2i}|[x_o, p_o]| = \frac{\hbar}{4} \tag{A.1}$$

The output field uncertainties are related to those of the input field:

$$\sigma_{x_o}\sigma_{p_o} = G\sigma_{x_o}G\sigma_{p_o} + A\frac{\hbar}{4} \tag{A.2}$$

where A is the noise added by the amplification process. Substituting and simplifying yields:

$$\frac{\hbar}{4} = G^2\frac{\hbar}{4} + A\frac{\hbar}{4} \tag{A.3}$$

$$1 = G^2 + A \tag{A.4}$$

The input referred noise, therefore is:

$$\frac{|A|}{G^2} = 1 - \frac{1}{G^2} \tag{A.5}$$

In the limit that the amplifier gain is large, $G \gg 1$, the input referred noise added by a linear amplifier operation at the quantum limit, in units of quanta, is:

$$\frac{|A|}{G^2} = 1 \tag{A.6}$$

At best, a linear amplifier would add one quanta worth of noise to the measurement of a signal ($\bar{n}_{\mathrm{SQL}} = 1$). Though this noise level is a huge improvement relative to field effect transistor amplifiers at $4\,\mathrm{K}$ ($\bar{n}_{4\mathrm{K}} = 13$) and room temperature amplifiers ($\bar{n}_{300\mathrm{K}} = 1000$), it is still too large for detecting the small signals expected from the dark matter. The photon counting technique developed in this work allows us to achieve the equivalent noise of $\bar{n} = 7.3 \times 10^{-4}$, and in principle, can be made arbitrarily low.

Appendix B

Jaynes-Cummings Hamiltonian

In Chapter 3 I use the approximation to the Jaynes-Cummings Hamiltonian in the dispersive limit. In this Appendix I show how to apply second order perturbation theory to a harmonic system coupled to a qubit to obtain an interaction that is the product of number operators.

The Jaynes-Cummmings Hamiltonian describes an exchange interaction between the cavity and the qubit. In the limit that the cavity (ω_c) and qubit (ω_q) detuning ($\Delta = \omega_c - \omega_q$) is much greater than their coupling g, we can expand the interaction to second order in the small parameter $\frac{g}{\Delta}$.

$$\mathcal{H} = \omega_c a^\dagger a + \frac{1}{2}\omega_q \sigma_z + g(a^\dagger \sigma^- + a\sigma^+) \tag{B.1}$$

The eigenvalues of the unperturbed Hamiltonian are:

$$\mathcal{H}^{(0)} |n, s\rangle = E^{(0)} |n, s\rangle = (n\omega_c + s\omega_q) |n, s\rangle \tag{B.2}$$

$s = \pm 1$ represent the ground and excited states of the qubit. The second order correction to the energy is:

$$E_{n,s}^{(2)} = \sum_{m \neq n} \sum_{r \neq s} \frac{\left| \langle m, r| g(a^\dagger \sigma^- + a\sigma^+) |n, s\rangle \right|^2}{E_{n,s}^{(0)} - E_{m,r}^{(0)}} \tag{B.3}$$

The matrix element:

$$\langle m, r| g(a^\dagger \sigma^- + a\sigma^+) |n, s\rangle = g\left[\sqrt{n}\delta_{m,n+1}\delta_{r,s-1} + \sqrt{n}\delta_{m,n-1}\delta_{r,s+1} \right]$$

For a given value of s, only one of the terms survives since there are only two possible qubit states. Enumerating these possibilities we find:

$$E_{n,+1}^{(2)} = \frac{g^2}{\Delta}n$$

$$E_{n,-1}^{(2)} = -\frac{g^2}{\Delta} n$$

For an arbitrary value of s:

$$E_{n,s}^{(2)} = \frac{g^2}{\Delta} sn \tag{B.4}$$

Recasting this in terms of the relevant operators:

$$\mathcal{H}^{(2)} = 2\frac{g^2}{\Delta} a^\dagger a \frac{1}{2}\sigma_z \tag{B.5}$$

$2\chi = 2\frac{g^2}{\Delta}$ is the photon number dependent shift of the qubit frequency (or visa versa). The full Hamiltonian, expanded to second order is given by:

$$\mathcal{H} = \omega_c a^\dagger a + \frac{1}{2}\omega_q \sigma_z + 2\chi a^\dagger a \frac{1}{2}\sigma_z \tag{B.6}$$

This interaction allows us to operate the qubit as a transducer between cavity population and qubit frequency.

Appendix C

Parity measurement

In Chapter 4, I show that the qubit can be used to infer the state of the cavity. This is accomplished by performing a parity measurement, effectively a Ramsey interferometry measurement, on the qubit. This resolves the shift in the qubit frequency due to a potential photon in the cavity. Here I describe the parity measurement sequence and calculate the time required for the qubit to precess to map the cavity state on to the qubit.

We assume the qubit begins in the ground state $|g\rangle$, this calculation proceeds analogously if the qubit begins in the excited state $|e\rangle$. We first place the qubit in its clock state, a super position of ground and excited, using a $\pi/2$ pulse:

$$|\psi(t = 0)\rangle = \frac{1}{\sqrt{2}}\left(|g\rangle + |e\rangle\right) \tag{C.1}$$

The time evolution of the superposition state is determined by the interaction Hamiltonian $\mathcal{H}/\hbar = 2\chi a^\dagger a \frac{1}{2}\sigma_z$.

$$|\psi(t)\rangle = e^{i\mathcal{H}t/\hbar}|\psi(t = 0)\rangle \tag{C.2}$$

$$|\psi(t)\rangle = e^{i2\chi a^\dagger a \frac{1}{2}\sigma_z t}\frac{1}{\sqrt{2}}\left(|g\rangle + |e\rangle\right) \tag{C.3}$$

$$|\psi(t)\rangle = \frac{1}{\sqrt{2}}\left(e^{in\chi t}|g\rangle + e^{-in\chi t}|e\rangle\right) \tag{C.4}$$

where n is the number of photons in the cavity. After a wait time, we apply a $-\pi/2$ pulse which takes the qubit state to

$$|\psi(t)\rangle = \frac{1}{2}\left[e^{in\chi t}(|g\rangle - |e\rangle) + e^{-in\chi t}(|g\rangle + |e\rangle)\right] \tag{C.5}$$

which simplifies to

$$|\psi(t)\rangle = \cos(n\chi t)\,|g\rangle + i\sin(n\chi t)\,|e\rangle \tag{C.6}$$

We chose the wait time t_p such that if there are n (for $n > 0$) photons in the cavity, the qubit state will be $|e\rangle$. This condition is satisfied by setting the square of the overlap of the final qubit state with the eigenstate $|e\rangle$ equal to 1.

$$|\langle e|\psi(t_p)\rangle|^2 = \sin^2(n\chi t_p) = 1 \tag{C.7}$$

$$|n\chi t_p| = \frac{\pi}{2} \tag{C.8}$$

$$t_p = \frac{\pi}{|n2\chi|} \tag{C.9}$$

In the case of searching for small populations deposited by the dark matter, we are mainly interested in searching for $n = 1$ photons. The parity wait time is $t_p = \pi/|2\chi|$.

An important note is that this procedure is not only sensitive to zero or one photons, but can distinguish and even or odd photon number state. This can be seen by setting the parity wait time to $t_p = \pi/|2\chi|$ in Equation C.7

$$|\langle e|\psi(t_p)\rangle|^2 = \sin^2\left(n\chi\frac{\pi}{2\chi}\right) \tag{C.10}$$

$$P(|e\rangle) = \sin^2\left(\frac{n\pi}{2}\right) \tag{C.11}$$

$$P(|e\rangle) = \begin{cases} 0 & \text{if } n = \text{even} \\ 1 & \text{if } n = \text{odd} \end{cases} \tag{C.12}$$

The parity measurement procedure maps even photon number cavity states on to the qubit state $|g\rangle$ and odd photon number cavity states on to the qubit state $|e\rangle$. This mapping of cavity states outside the 0,1 manifold provides additional sensitivity to potential dark matter signals. In Chapter 7, I use this fact to exclude dark matter candidates that would produce

large amplitude signals that have significant odd photon number components.

Appendix D

Python code for forward-backward algorithm

Cavity state reconstruction is done by using a Bayesian inference technique. Given a sequence of measurement, the goal is to efficiently compute the probability of the initial cavity state. This is accomplished by using the forward-backward algorithm. This recursive algorithm can compute the state probabilities during any measurement by taking into account information from previous and future measurements[89]. Below is the forward-backward algorithm implemented in Python, used for the analysis in this work.

```python
# inputs to the algorithm are
# meas_seq: list of readout measurements in a given counting experiment.
# values of meas_seq represent G,E readout as 0,1
# T: transition matrix for hidden Markov model
# E: emission matrix


# output of algorithm is the full state reconstruction in gamma_matrix
# joint qubit-caviy states [0g, 0e, 1g, 1e] represented as [0,1,2,3]
# gamma_matrix[ii,:] = state probabilities at ii_th measurement
# gamma_matrix[:,jj] = jj_th state probability for all measurements


def forward(meas_seq, T, E):
# computes the probability of the possible state at the ii_th measurement
# given all the measurements up to ii
        num_meas = len(meas_seq)
        N = T.shape[0]
        alpha = zeros((num_meas, N))
        # assign flat prior to the 4 possible states (0g, 0e, 1g, 1e)
```

```python
        pi = [0.25,0.25,0.25,0.25]

        alpha[0] = pi*E[:,meas_seq[0]]

        for t in range(1, num_meas):

            alpha[t] = alpha[t-1].dot(T) * E[:, meas_seq[t]]

        return alpha


def backward(meas_seq, T, E):
# computes the probability of the observed sequence after the ii_th measurement
# given the measured signal at ii
        N = T.shape[0]

        num_meas = len(meas_seq)

        beta = zeros((N,num_meas))

        beta[:,-1:] = 1

        for t in reversed(range(num_meas-1)):

            for n in range(N):

                beta[n,t] = sum(beta[:,t+1] * T[n,:] * E[:, meas_seq[t+1]])

        return beta


def likelihood(meas_seq, T, E):
# computes the probability of a measured sequence using the forward algorithm
# can also be computed using the backward algorithm
        return  forward(meas_seq, T, E)[-1].sum()


def gamma(meas_seq,T,E):
# computes the state probability at the ii_th measurement
# given all measurements in the sequence
    alpha = forward(meas_seq, T, E)
```

```python
    beta  = backward(meas_seq, T, E)

    obs_prob = likelihood(meas_seq, T, E)

    # combine forward and backward algorithms

    return (multiply(alpha,beta.T) / obs_prob)


# calculate the cavity state probabilities given a measured sequence
gamma_matrix = gamma(meas_seq, T, E)
# obtain initial state probabilities, ii=0
# marginalize over qubit state, P(n) = P(n,g) + P(n,e)
P0 = gamma_matrix[0,0] + gamma_matrix[0,1]
P1 = gamma_matrix[0,2] + gamma_matrix[0,3]
```

References

[1] Yeh, J.-H., LeFebvre, J., Premaratne, S., Wellstood, F. C. & Palmer, B. S. Microwave attenuators for use with quantum devices below 100 mk. *Journal of Applied Physics* **121**, 224501 (2017).

[2] Caves, C. M. Quantum limits on noise in linear amplifiers. *Phys. Rev. D* **26**, 1817–1839 (1982).

[3] Pezzè, L., Smerzi, A., Oberthaler, M. K., Schmied, R. & Treutlein, P. Quantum metrology with nonclassical states of atomic ensembles. *Reviews of Modern Physics* **90** (2018).

[4] Arias, P. *et al.* Wispy cold dark matter. *Journal of Cosmology and Astroparticle Physics* **2012**, 013–013 (2012).

[5] McDermott, S. D. & Witte, S. J. Cosmological evolution of light dark photon dark matter. *Phys. Rev. D* **101** (2020).

[6] Graham, P. W., Mardon, J. & Rajendran, S. Vector dark matter from inflationary fluctuations. *Phys. Rev. D* **93** (2016).

[7] Dixit, A. V. *et al.* Searching for dark matter with a superconducting qubit. *Phys. Rev. Lett.* **126**, 141302 (2021).

[8] Gambetta, J. *et al.* Qubit-photon interactions in a cavity: Measurement-induced dephasing and number splitting. *Phys. Rev. A* **74**, 042318 (2006).

[9] Nigg, S. E. *et al.* Black-box superconducting circuit quantization. *Phys. Rev. Lett.* **108** (2012).

[10] Tanabashi, M. *et al.* Review of particle physics. *Phys. Rev. D* **98**, 030001 (2018).

[11] Rubin, V. C., Ford, J., W. K. & Thonnard, N. Rotational properties of 21 SC galaxies with a large range of luminosities and radii, from NGC 4605 (R=4kpc) to UGC 2885 (R=122kpc). *Astrophysical Journal* **238**, 471–487 (1980).

[12] Oort, J. H. Observational evidence confirming Lindblad's hypothesis of a rotation of the galactic system. *Bulletin of the Astronomical Institutes of the Netherlands* **3**, 275 (1927).

[13] Zwicky, F. On the Masses of Nebulae and of Clusters of Nebulae. *Astrophysical Journal* **86**, 217 (1937).

[14] Einstein, A. The Foundation of the General Theory of Relativity. *Annalen Phys.* **49**, 769–822 (1916).

[15] Fixsen, D. J. The Temperature of the Cosmic Microwave Background. *The Astrophysical Journal* **707**, 916–920 (2009).

[16] Ade, P. A. R. *et al.* Planck 2015 results. XIII. Cosmological parameters. *Astronomy & Astrophysics* **594**, A13 (2016).

[17] Komatsu, E. *et al.* Seven-Year Wilkinson Microwave Anisotropy Probe (WMAP) Observations: Cosmological Interpretation. *The Astrophysical Journal Supplement Series* **192**, 18 (2011).

[18] Wallraff, A. *et al.* Strong coupling of a single photon to a superconducting qubit using circuit quantum electrodynamics. *Nature* **431**, 162–167 (2004).

[19] Schuster, D. I. *et al.* Resolving photon number states in a superconducting circuit. *Nature* **445**, 515–518 (2007).

[20] Josephson, B. D. Possible new effects in superconductive tunnelling. *Physics Letters* **1**, 251–253 (1962).

[21] Anderson, P. W. & Rowell, J. M. Probable observation of the josephson superconducting tunneling effect. *Phys. Rev. Lett.* **10**, 230–232 (1963).

[22] Josephson, B. D. The discovery of tunnelling supercurrents. *Rev. Mod. Phys.* **46**, 251–254 (1974).

[23] Peccei, R. D. & Quinn, H. R. CP conservation in the presence of pseudoparticles. *Phys. Rev. Lett.* (1977).

[24] Peccei, R. D. & Quinn, H. R. Constraints imposed by CP conservation in the presence of pseudoparticles. *Phys. Rev. D* (1977).

[25] Wilczek, F. Problem of Strong P and T Invariance in the Presence of Instantons. *Phys. Rev. Lett.* **40**, 279–282 (1978).

[26] Weinberg, S. A New Light Boson? *Phys. Rev. Lett.* **40**, 223–226 (1978).

[27] Preskill, J., Wise, M. B. & Wilczek, F. Cosmology of the Invisible Axion. *Phys. Lett. B* **120**, 127–132 (1983).

[28] Abbott, L. & Sikivie, P. A Cosmological Bound on the Invisible Axion. *Phys. Lett. B* **120**, 133–136 (1983).

[29] Dine, M. & Fischler, W. The Not So Harmless Axion. *Phys. Lett. B* **120**, 137–141 (1983).

[30] Co, R. T. & Harigaya, K. Axiogenesis. *Phys. Rev. Lett.* **124** (2020).

[31] Chelouche, D., Rabadán, R., Pavlov, S. S. & Castejón, F. Spectral signatures of photon-particle oscillations from celestial objects. *The Astrophysical Journal Supplement Series* **180**, 1–29 (2008).

[32] Ahmed, Z. *et al.* Search for Axions with the CDMS Experiment. *Physical Review Letters* **103** (2009).

[33] Aprile, E. *et al.* First axion results from the XENON100 experiment. *Physical Review D* **90** (2014).

[34] Robilliard, C. *et al.* No "light shining through a wall": Results from a photoregeneration experiment. *Physical Review Letters* **99** (2007).

[35] Ehret, K. *et al.* New ALPS results on hidden-sector lightweights. *Physics Letters B* **689**, 149–155 (2010).

[36] Du, N. *et al.* Search for Invisible Axion Dark Matter with the Axion Dark Matter Experiment. *Phys. Rev. Lett.* **120**, 151301 (2018).

[37] Braine, T. *et al.* Extended search for the invisible axion with the axion dark matter experiment. *Phys. Rev. Lett.* **124** (2020).

[38] Brubaker, B. M. *et al.* First Results from a Microwave Cavity Axion Search at 24 μeV. *Phys. Rev. Lett.* **118**, 1–5 (2017).

[39] Zhong, L. *et al.* Results from phase 1 of the haystac microwave cavity axion experiment. *Phys. Rev. D* **97** (2018).

[40] Backes, K. M. *et al.* A quantum enhanced search for dark matter axions. *Nature* **590**, 238–242 (2021).

[41] Dine, M., Fischler, W. & Srednicki, M. A simple solution to the strong CP problem with a harmless axion. *Physics Letters B* **104**, 199–202 (1981).

[42] Zhitnitsky, A. On Possible Suppression of the Axion Hadron Interactions. (In Russian). *Sov. J. Nucl. Phys.* **31**, 260 (1980).

[43] Kim, J. E. Weak-interaction singlet and strong CP invariance. *Phys. Rev. Lett.* **43**, 103–107 (1979).

[44] Shifman, M., Vainshtein, A. & Zakharov, V. Can confinement ensure natural cp invariance of strong interactions? *Nuclear Physics B* **166**, 493–506 (1980).

[45] Horns, D. *et al.* Searching for wispy cold dark matter with a dish antenna. *Journal of Cosmology and Astroparticle Physics* **2013**, 016–016 (2013).

[46] Lamoreaux, S. K., van Bibber, K. A., Lehnert, K. W. & Carosi, G. Analysis of single-photon and linear amplifier detectors for microwave cavity dark matter axion searches. *Phys. Rev. D* **88**, 35020 (2013).

[47] Brune, M., Haroche, S., Lefevre, V., Raimond, J. M. & Zagury, N. Quantum nondemolition measurement of small photon numbers by rydberg-atom phase-sensitive detection. *Phys. Rev. Lett.* **65**, 976–979 (1990).

[48] Gleyzes, S. *et al.* Observing the quantum jumps of light : birth and death of a photon in a cavity. *Nature* **446**, 297 (2007).

[49] Jaynes, E. T. & Cummings, F. W. Comparison of quantum and semiclassical radiation theories with application to the beam maser. *Proceedings of the IEEE* **51**, 89–109 (1963).

[50] Leek, P. J. *et al.* Cavity quantum electrodynamics with separate photon storage and qubit readout modes. *Phys. Rev. Lett.* **104** (2010).

[51] Purcell, E. M., Torrey, H. C. & Pound, R. V. Resonance absorption by nuclear magnetic moments in a solid. *Phys. Rev.* **69**, 37–38 (1946).

[52] Chakram, S. *et al.* Seamless high-q microwave cavities for multimode circuit qed (2020). Preprint at arxiv.org/abs/2010.16382.

[53] Koch, J. *et al.* Charge-insensitive qubit design derived from the cooper pair box. *Phys. Rev. A* **76** (2007).

[54] Ambegaokar, V. & Baratoff, A. Tunneling between superconductors. *Phys. Rev. Lett.* **10**, 486–489 (1963).

[55] Kono, S., Koshino, K., Tabuchi, Y., Noguchi, A. & Nakamura, Y. Quantum non-demolition detection of an itinerant microwave photon. *Nature Physics* **14**, 546–549 (2018).

[56] Braginsky, V. B. & Khalili, F. Y. Quantum nondemolition measurements: the route from toys to tools. *Rev. Mod. Phys.* **68**, 1–11 (1996).

[57] Nogues, G. *et al.* Seeing a single photon without destroying it. *Nature* **400**, 239–242 (1999).

[58] Johnson, B. R. *et al.* Quantum non-demolition detection of single microwave photons in a circuit. *Nature Physics* **6**, 663–667 (2010).

[59] Zheng, H., Silveri, M., Brierley, R. T., Girvin, S. M. & Lehnert, K. W. Accelerating dark-matter axion searches with quantum measurement technology (2016). Preprint at arxiv.org/abs/1607.02529.

[60] Hann, C. T. *et al.* Robust readout of bosonic qubits in the dispersive coupling regime. *Phys. Rev. A* **98** (2018).

[61] Elder, S. S. *et al.* High-fidelity measurement of qubits encoded in multilevel superconducting circuits. *Phys. Rev. X* **10** (2020).

[62] Pechal, M. *et al.* Microwave-controlled generation of shaped single photons in circuit quantum electrodynamics. *Phys. Rev. X* **4** (2014).

[63] Kurpiers, P. *et al.* Deterministic quantum state transfer and remote entanglement using microwave photons. *Nature* **558**, 264–267 (2018).

[64] Rosenblum, S. *et al.* A cnot gate between multiphoton qubits encoded in two cavities. *Nature Communications* **9** (2018).

[65] Magnard, P. *et al.* Fast and unconditional all-microwave reset of a superconducting qubit. *Phys. Rev. Lett.* **121** (2018).

[66] Tanner, J. E. & Stejskal, E. O. Restricted self-diffusion of protons in colloidal systems by the pulsed-gradient, spin-echo method. *The Journal of Chemical Physics* **49**, 1768–1777 (1968).

[67] Jin, X. *et al.* Thermal and residual excited-state population in a 3d transmon qubit. *Phys. Rev. Lett.* **114** (2015).

[68] Wang, Z. *et al.* Cavity attenuators for superconducting qubits. *Phys. Rev. Appl.* **11** (2019).

[69] Serniak, K. *et al.* Hot nonequilibrium quasiparticles in transmon qubits. *Phys. Rev. Lett.* **121** (2018).

[70] Christensen, B. G. *et al.* Anomalous charge noise in superconducting qubits. *Phys. Rev. B* **100** (2019).

[71] Vepsäläinen, A. P. *et al.* Impact of ionizing radiation on superconducting qubit coherence. *Nature* **584**, 551–556 (2020).

[72] Riwar, R.-P. *et al.* Normal-metal quasiparticle traps for superconducting qubits. *Phys. Rev. B* **94** (2016).

[73] Wilen, C. D. *et al.* Correlated charge noise and relaxation errors in superconducting qubits (2020). Preprint at arxiv.org/abs/2012.06029.

[74] Clerk, A. A. & Utami, D. W. Using a qubit to measure photon-number statistics of a driven thermal oscillator. *Phys. Rev. A* **75**, 042302 (2007).

[75] Walter, T. *et al.* Rapid high-fidelity single-shot dispersive readout of superconducting qubits. *Phys. Rev. Appl.* **7** (2017).

[76] McClure, D. *et al.* Rapid driven reset of a qubit readout resonator. *Phys. Rev. Appl.* **5** (2016).

[77] Motzoi, F., Buchmann, L. & DIckel, C. Simple, smooth and fast pulses for dispersive measurements in cavities and quantum networks (2018). Preprint at arxiv.org/abs/1809.04116.

[78] Misra, B. & Sudarshan, E. C. G. The zeno's paradox in quantum theory. *Journal of Mathematical Physics* **18**, 756–763 (1977).

[79] Rolke, W. A., López, A. M. & Conrad, J. Limits and confidence intervals in the presence of nuisance parameters. *Nuclear Instruments and Methods in Physics Research Section A: Accelerators, Spectrometers, Detectors and Associated Equipment* **551**, 493–503 (2005).

[80] Conrad, J., Botner, O., Hallgren, A. & Pérez de los Heros, C. Including systematic uncertainties in confidence interval construction for poisson statistics. *Physical Review D* **67** (2003).

[81] Foster, J. W., Rodd, N. L. & Safdi, B. R. Revealing the dark matter halo with axion direct detection. *Phys. Rev. D* **97** (2018).

[82] Alesini, D. *et al.* High quality factor photonic cavity for dark matter axion searches. *Review of Scientific Instruments* **91**, 094701 (2020).

[83] Leung, N. *et al.* Deterministic bidirectional communication and remote entanglement generation between superconducting quantum processors. *npj Quantum Information* **5** (2018).

[84] Axline, C. J. *et al.* On-demand quantum state transfer and entanglement between remote microwave cavity memories. *Nature Physics* **14**, 705–710 (2018).

[85] Gao, Y. Y. *et al.* Programmable interference between two microwave quantum memories. *Phys. Rev. X* **8**, 021073 (2018).

[86] Wolf, F. *et al.* Motional fock states for quantum-enhanced amplitude and phase measurements with trapped ions. *Nature Communications* **10** (2019).

[87] Chakram, S. *et al.* Multimode photon blockade (2020). Preprint at arxiv.org/abs/2010.15292.

[88] Naik, R. K. *et al.* Random access quantum information processors using multimode circuit quantum electrodynamics. *Nature Communications* **8** (2017).

[89] Jurafsky, D. & Martin, J. H. *Speech and Language Processing* (Third Edition draft, 2020). Appendix A: Hidden Markov Model.